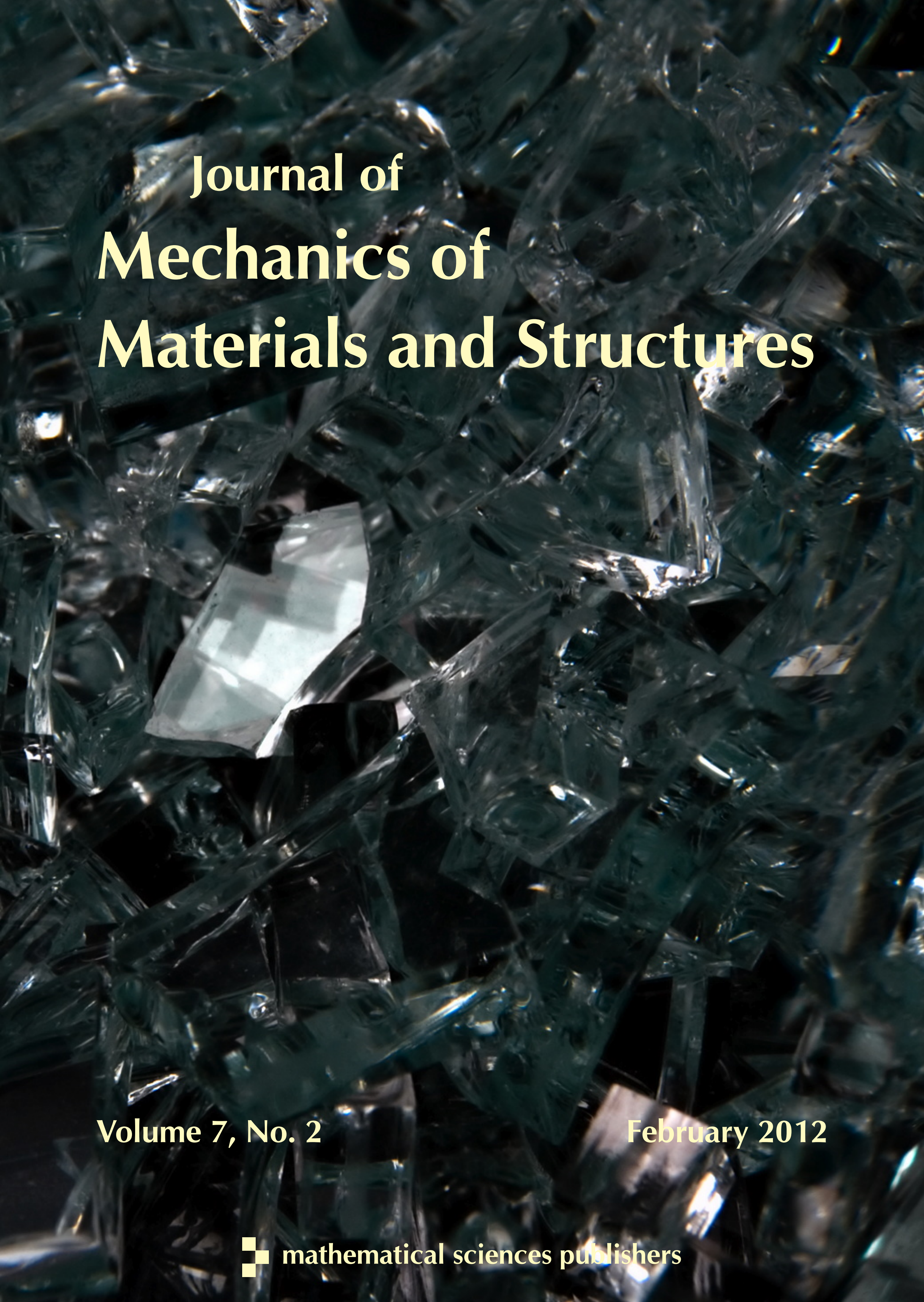

Journal of
Mechanics of Materials and Structures

Volume 7, No. 2
February 2012

mathematical sciences publishers

JOURNAL OF MECHANICS OF MATERIALS AND STRUCTURES

jomms.net

Founded by Charles R. Steele and Marie-Louise Steele

Cover design: Alex Scorpan Cover photo: Mando Gomez, www.mandolux.com

See http://jomms.net for submission guidelines.

JoMMS (ISSN 1559-3959) is published in 10 issues a year. The subscription price for 2012 is US $555/year for the electronic version, and $735/year (+$60 shipping outside the US) for print and electronic. Subscriptions, requests for back issues, and changes of address should be sent to Mathematical Sciences Publishers, Department of Mathematics, University of California, Berkeley, CA 94720–3840.

JoMMS peer-review and production is managed by EditFlow® from Mathematical Sciences Publishers.

PUBLISHED BY
mathematical sciences publishers
http://msp.org/
A NON-PROFIT CORPORATION
Typeset in LaTeX

JOURNAL OF MECHANICS OF MATERIALS AND STRUCTURES
Vol. 7, No. 2, 2012

MICROMECHANICAL ANALYSIS OF UNIDIRECTIONAL COMPOSITES USING A LEAST-SQUARES-BASED DIFFERENTIAL QUADRATURE ELEMENT METHOD

MOHAMMAD BAYAT AND MOHAMMAD MOHAMMADI AGHDAM

A generalized plane strain micromechanical model is developed to predict the stress and strain fields and overall elastic properties of a unidirectional fiber-reinforced composite subjected to various axial and transverse normal loading conditions using a least-squares-based differential quadrature element method (DQEM). The representative volume element (RVE) of the composite consists of a quarter of the fiber surrounded by matrix to represent the real composite with a repeating square array of fibers. The cubic serendipity shape functions are used to convert the solution domain to a proper rectangular domain and the new versions of the governing equations and boundary conditions are also derived. The fully bonded fiber-matrix interface condition is considered and the displacement continuity and traction reciprocity are imposed on the fiber-matrix interface. Application of DQEM to the problem leads to an overdetermined system of linear equations mainly due to the particular periodic boundary conditions of the RVE. A least-squares differential quadrature element method is used to obtain solutions for the governing partial differential equations of the problem. The numerical results are in excellent agreement with the available analytical and finite element studies. Moreover, the results of this study reveal that the presented model can provide highly accurate results with a very small number of elements and grid points within each element. In addition, the model shows advantages over conventional analytical models for fewer simplifying assumptions related to the geometry of the RVE.

1. Introduction

Effective and proper use of composites relies on how these materials behave under various types of loading. Both numerical [Adams and Doner 1967; Adams 1970; Eischen and Torquato 1993; Nedele and Wisnom 1994; Sun and Vaidya 1996; Aghdam et al. 2000; 2001; Ahmadi and Aghdam 2010] and analytical [Eshelby 1957; Hashin and Rosen 1964; Hill 1965; Uemura et al. 1979; Mikata and Taya 1985; Nairn 1985; Aboudi 1987; 1989; Nimmer 1990; Robertson and Mall 1993; Aghdam and Dezhestan 2005] micromechanical models have been used to predict the elastic, plastic, and thermal properties of composite materials and their responses to different thermal and mechanical loading conditions.

Numerical models include finite difference [Adams and Doner 1967], finite element [Adams 1970; Nedele and Wisnom 1994; Sun and Vaidya 1996; Aghdam et al. 2000; 2001], boundary element [Eischen and Torquato 1993], and, more recently, meshless [Ahmadi and Aghdam 2010] methods. Among the earliest finite element models, one can refer to [Adams 1970], covering the inelastic behavior of composites subjected to transverse normal loading using a plane strain finite element approach. Other studies on the finite element micromechanical modeling of composites for obtaining overall properties include

---

Keywords: least-squares DQEM, micromechanics, generalized plane strain, UD fiber-reinforced composite, microstress/strain fields, overall properties.

various simple uniaxial loading conditions such as longitudinal and transverse normal or shear loading [Sun and Vaidya 1996], combined axial shear and thermal loading [Nedele and Wisnom 1994] and off-axis loading of composites [Aghdam et al. 2001], and yielding and collapse behavior of unidirectional (UD) composites [Aghdam et al. 2000]. The boundary element method [Eischen and Torquato 1993] is also used to study the elastic behavior of composite materials.

Various analytical micromechanical models have also been proposed to evaluate the behavior of heterogeneous materials based on constituent properties, volume fractions, and their interactions. Among the first analytical approaches to model composite behavior were the model presented in [Eshelby 1957] and the self-consistent model of [Hill 1965]. Analytical models based on the variational principles of the theory of elasticity [Hashin and Rosen 1964] have also been employed to obtain upper and lower bounds of the overall elastic properties of composite materials. In these models, while the minimum complementary energy method yields the lower bounds, the minimum potential energy principle results in the upper bounds.

There is another class of analytical models in which a small area of the composite is considered as a representative volume element (RVE) of the composite. These types of models can be categorized into various groups based on the simplifying assumptions made about the geometry of the composite. The two major groups are composite cylinder models (CCM) and unit cell models (UCM). The geometry of the RVE in CCM consists of a circular fiber surrounded by a circular matrix [Uemura et al. 1979]. In some cases, more than two concentric cylinders were considered to study the effects of the interface [Nairn 1985] and fiber coating [Mikata and Taya 1985]. In UCM however, the cross section of the RVE includes a rectangular fiber surrounded by several rectangular blocks of matrix. One of the well-known micromechanical models in the category of UCM is the method of cells (MC), which was developed in [Aboudi 1987; 1989]. This model has several advantages compared with other similar models while also being mathematically rigorous. More UCM types of models can be found elsewhere [Nimmer 1990; Robertson and Mall 1993; Aghdam and Dezhestan 2005].

Analytical models normally require more rigorous mathematical procedures [Aboudi 1987; 1989] while normally involving more simplifying assumptions [Aboudi 1987; 1989; Nimmer 1990; Robertson and Mall 1993; Aghdam and Dezhestan 2005]. Furthermore, most analytical models are not able to provide a nonuniform distribution of stress and strain fields within the RVE, though their predictions for overall properties are reasonably accurate. In numerical techniques, however, there are fewer simplifying assumptions, and accuracy depends on the number of elements or grid points. For instance, in order to obtain more accurate results in finite element analysis, the geometry of the RVE should be divided into a few hundred small elements.

In the past decade, the differential quadrature element method (DQEM) has been used to study the behavior of different structural elements [Wang et al. 1996; Wang and Gu 1997; Karami and Malekzadeh 2002; Chen 2003]. However, apart from applications of the differential quadrature (DQ) method in fluid mechanics, all the studies in the literature have been restricted to various 2D elasticity problems of isotropic and laminated plates and shells; the method has not been used in micromechanics of heterogeneous materials. These studies revealed that the method offers a good convergence rate and accuracy with a relatively small number of grid points. However, implementation of boundary conditions is a challenging and time-consuming procedure in DQEM. This is mainly due to the resultant overdetermined system of algebraic equations in most DQEM problems. In order to prevent formation of overdetermined system of equations after implementation of multiboundary conditions, several approaches have been presented in the literature. For example, some DQ equations at inner nodes can be replaced by the additional boundary conditions. However, it has been found that the accuracy of the results may vary depending on which DQ equations at the inner grids are replaced by the boundary conditions [Zong and Zhang 2009]. Jang et al. [1989] proposed the so-called δ-technique wherein, adjacent to the boundary points of the differential quadrature grid, points are chosen at a small distance $\delta \cong 10^{-5}$ (as a dimensionless value). Then the DQ analog of the two conditions at a boundary are written for the boundary points and their adjacent δ-points. Wang and Bert [1993] introduced an approach where the boundary conditions are formed during formulation of the weighting coefficients for higher-order derivatives. Malik and Bert [1996] tried to employ this approach for all boundary conditions. Wang et al. [1996; Wang and Gu 1997] introduced another method in which multiboundary conditions are imposed by assigning two degrees of freedom to each end point for a fourth-order differential equation. Wu and Liu [2000] proposed a generalized differential quadrature rule, introducing multiple degrees of freedom at boundary points. Recently, Karami and Malekzadeh [2002] proposed a method of applying the multiboundary conditions. In formulations of the weighting coefficients of third and fourth-order derivatives, the second derivatives at the boundary points are viewed as additional independent variables.

Briefly, in order to adjust the number of equations and unknowns, researchers normally eliminate some of the equations [Wang 2001] or add extra unknowns to the problem [Karami and Malekzadeh 2002; Wu and Liu 2000]. However, in this study all of the governing equations and boundary conditions are considered and, therefore, the resultant overdetermined system of equations is solved using a least-squares technique.

In this study, a two-dimensional generalized plane strain micromechanical model is presented to predict the behavior of a UD composite system using DQEM. The geometry of the RVE is divided into three elements, as shown in Figure 1, which are then mapped to a rectangular domain using the cubic serendipity shape functions (see Figure 2). The fully bonded fiber-matrix interface condition is considered and the displacement continuity and traction reciprocity are imposed on the fiber-matrix interface. The new version of the governing partial differential equations of the problem and their boundary and interface conditions are obtained. Application of DQEM to the problem leads to an overdetermined system of linear equations mainly due to the particular periodic boundary conditions of the RVE. A least-squares differential quadrature element method (LSDQEM) is used to obtain solutions for the governing partial differential equations of the problem. The results of this study show excellent agreement with the finite element analysis for various stress and displacement components of a SiC/Ti composite system. The predicted overall properties of the same SiC/Ti system also show excellent agreement with other analytical and finite element analyses.

2. Analysis

2.1. ***Geometry of the model.*** In a real UD fiber-reinforced composite, the fibers are likely to be arranged in a random array. It is difficult, if not impossible, to model the composite behavior with the real constituent geometry. Apart from some approximate bounds found for a random array of fibers and arbitrary phase geometry using a variational method [Hill 1965], the actual cross section of the composite has to be idealized as a regular array of fibers. In most analytical, finite element, and numerical models,

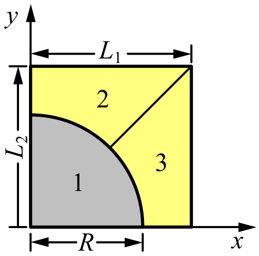

Figure 1. Geometry of the RVE and selected elements.

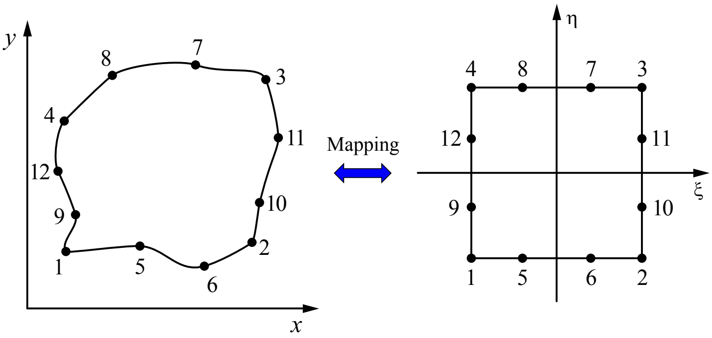

Figure 2. Mapping of the cubic serendipity element from the physical domain (left) to the computational domain (right).

the cross section of the composite is simplified as periodic arrays of fibers, either in a square or hexagonal array packing, as shown in Figure 3. In this study, the fibers are assumed to be arranged in square arrays. The second step is to choose the smallest informative and repeating area of the geometry for the whole cross section as the RVE. It is assumed that all the effective characteristics and global behavior of the composite are similar to those of the RVE. Hence, special care should be taken to select the correct RVE and to apply the correct boundary conditions to model the real loading conditions on the composite. Commonly, a quarter of the fiber and the corresponding matrix, as shown in Figure 1, are sufficient to model various loading conditions.

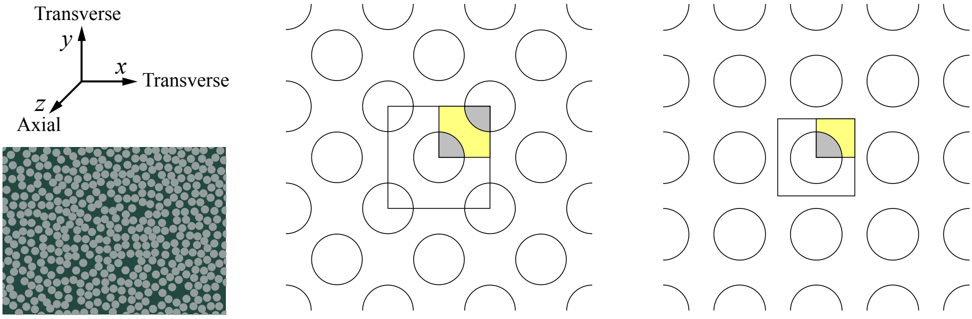

Figure 3. Left: schematic diagram of a real UD composite. Middle: unit cell and RVE of hexagonal array. Right: unit cell and RVE of square array.

2.2. *Governing equations.* Assuming a generalized plane strain condition which can provide more realistic predictions, the displacement fields within the RVE can be considered as

$$u = u(x, y), \quad v = v(x, y), \quad w = \varepsilon_{z0} \cdot z, \tag{1}$$

where u, v, and w are displacements in the x, y, and z directions, respectively, and ε_{z0} is an unknown constant strain in the fiber direction to be determined. Based on the theory of elasticity, the strain-displacement relations within the RVE are

$$\varepsilon_x = u_{,x}, \quad \varepsilon_y = v_{,y}, \quad \varepsilon_z = w_{,z}, \quad \gamma_{xy} = v_{,x} + u_{,y}, \quad \gamma_{xz} = w_{,x} + u_{,z}, \quad \gamma_{yz} = w_{,y} + v_{,z}, \tag{2}$$

in which $(\,)_{,x} \equiv \partial(\,)/\partial x$. The generalized plane strain condition for displacements requires vanishing shear strains $\gamma_{xz} = \gamma_{yz} = 0$ and consequently zero shear stresses $\tau_{xz} = \tau_{yz} = 0$. Furthermore, assuming linear elastic behavior for both constituents, stress-strain relations for each phase of the RVE can be written as

$$\begin{aligned} \sigma_x &= B(u_{,x} + Cv_{,y} + C\varepsilon_{0z}), & \sigma_y &= B(Cu_{,x} + v_{,y} + C\varepsilon_{0z}), \\ \sigma_z &= B(Cu_{,x} + Cv_{,y} + \varepsilon_{0z}), & \tau_{xy} &= G(v_{,x} + u_{,y}), \end{aligned} \tag{3}$$

where constants B and C are

$$B = \frac{E(1-\nu)}{(1+\nu)(1-2\nu)}, \quad C = \frac{\nu}{1-\nu}, \tag{4}$$

in which E and ν are the elasticity modulus and the Poisson's ratio of the constituents, respectively. Finally, the governing equilibrium equations of the problem in the absence of body forces can be written in terms of displacement components as

$$\alpha u_{,xx} + \beta v_{,xy} + u_{,yy} = 0, \quad \alpha v_{,yy} + \beta u_{,xy} + v_{,xx} = 0, \tag{5}$$

where $\alpha = 2(1-\nu)/(1-2\nu)$ and $\beta = 1/(1-2\nu)$.

2.3. *Mapping the geometry of the RVE.* In this study, a RVE corresponding to a square array of fibers is considered. In order to apply DQEM to solve the governing equations, the RVE is divided into three irregular regions/elements, as shown in Figure 1. Using geometric natural-to-Cartesian mappings, an irregular quadrilateral physical domain (x, y), as shown in Figure 2, can be mapped into a normalized computational domain (ξ, η) based on the following cubic serendipity shape function:

$$x = \sum_{i=1}^{12} N_i(\xi, \eta) \cdot x_i, \quad y = \sum_{i=1}^{12} N_i(\xi, \eta) \cdot y_i \quad (-1 \le \xi, \eta \le 1), \tag{6}$$

where $N_i(\xi, \eta)$ is the cubic serendipity shape function defined by

$$\begin{aligned} N_i(\xi, \eta) &= \tfrac{1}{32}(1+\xi\xi_i)(1+\eta\eta_i)[9(\xi^2+\eta^2)-10], & i &= 1, 2, 3, 4, \\ N_i(\xi, \eta) &= \tfrac{9}{32}(1-\xi^2)(1+\eta\eta_i)(1+9\xi\xi_i), & i &= 5, 6, 7, 8, \\ N_i(\xi, \eta) &= \tfrac{9}{32}(1+\xi\xi_i)(1-\eta^2)(1+9\eta\eta_i), & i &= 9, 10, 11, 12, \end{aligned} \tag{7}$$

in which ξ_i and η_i are the coordinates of the node i in the ξ-η domain. In order to obtain the new version of the governing equations in the computational square element, the Jacobian of transformation matrix,

$$[J]=\begin{bmatrix} x_{,\xi} & y_{,\xi} \\ x_{,\eta} & y_{,\eta} \end{bmatrix},$$

is inverted:

$$[J]^{-1}=\begin{bmatrix} \xi_{,x} & \eta_{,x} \\ \xi_{,y} & \eta_{,y} \end{bmatrix}=\frac{1}{|J|}\begin{bmatrix} y_{,\eta} & -y_{,\xi} \\ -x_{,\eta} & x_{,\xi} \end{bmatrix}, \qquad |J|=x_{,\xi}y_{,\eta}-x_{,\eta}y_{,\xi}, \tag{8}$$

where $|J|$ is the determinant of the Jacobian matrix. Thus, the transformation of the first-order derivatives is

$$\begin{Bmatrix} u_{,x} \\ u_{,y} \end{Bmatrix}=[J]^{-1}\begin{Bmatrix} u_{,\xi} \\ u_{,\eta} \end{Bmatrix}. \tag{9}$$

To include second-order derivatives, the transformation may be written in matrix form as

$$\begin{Bmatrix} u_{,\xi} \\ u_{,\eta} \\ u_{,\xi\eta} \\ u_{,\xi\xi} \\ u_{,\eta\eta} \end{Bmatrix}=\begin{bmatrix} x_{,\xi} & y_{,\xi} & 0 & 0 & 0 \\ x_{,\eta} & y_{,\eta} & 0 & 0 & 0 \\ x_{,\xi\eta} & y_{,\xi\eta} & x_{,\xi}y_{,\eta}+x_{,\eta}y_{,\xi} & x_{,\xi}x_{,\eta} & y_{,\eta}y_{,\xi} \\ x_{,\xi\xi} & y_{,\xi\xi} & 2x_{,\xi}y_{,\xi} & x_{,\xi}^2 & y_{,\xi}^2 \\ x_{,\eta}^2 & y_{,\eta}^2 & 2x_{,\eta}y_{,\eta} & x_{,\eta}^2 & y_{,\eta}^2 \end{bmatrix}\begin{Bmatrix} u_{,x} \\ u_{,y} \\ u_{,xy} \\ u_{,xx} \\ u_{,yy} \end{Bmatrix}. \tag{10}$$

The inverse transformation can be expressed as explicit functions of (ξ, η), similar to (9). Implementation of the DQ method on the computational square domain is straightforward.

2.4. ***DQ method.*** The quadrature rules for a function $\Psi=\Psi(x, y)$ on a rectangular domain $(0\le x\le a, 0\le y\le b)$, can be written as follows [Bert and Malik 1996]:

$$\left.\frac{\partial^r\Psi}{\partial x^r}\right|_{x=x_i}=\sum_{k=1}^{N_x}A_{ik}^{(r)}\Psi_{kj}, \quad i=1,2,\dots,N_x, \qquad \left.\frac{\partial^s\Psi}{\partial y^s}\right|_{y=y_j}=\sum_{l=1}^{N_y}B_{jl}^{(s)}\Psi_{il}, \quad j=1,2,\dots,N_y, \tag{11}$$

$$\int_{x=0}^{a}\Psi(x, y_j)\,dx=\sum_{k=1}^{N_x}C_k\Psi_{kj}, \qquad \int_{y=0}^{b}\Psi(x_i, y)\,dy=\sum_{l=1}^{N_y}C_l\Psi_{il},$$

$$\int_{x=0}^{a}\int_{y=0}^{b}\Psi(x,y)\,dx\,dy=\sum_{k=1}^{N_x}C_k\sum_{l=1}^{N_y}D_l\Psi_{kl}, \qquad \left.\frac{\partial^{(r+s)}\Psi}{\partial x^r\partial y^s}\right|_{x_i,y_j}=\frac{\partial^r}{\partial x^r}\left.\left(\frac{\partial^s\Psi}{\partial y^s}\right)\right|_{x_i,y_j}=\sum_{k=1}^{N_x}A_{ik}^{(r)}\sum_{l=1}^{N_y}B_{jl}^{(s)}\Psi_{kl},$$

where N_x and N_y are the numbers of grid points in the x and y directions, respectively, $\psi_{ij}=\psi(x_i, y_j)$, and $A_{ij}^{(r)}$, $B_{ij}^{(s)}$, C_i, and D_i are weighting coefficients. For example, in order to determine the weighting coefficients $A_{ik}^{(r)}$, the Lagrange interpolation basic functions [Shu and Richards 1992b; Bert et al. 1993] are used as test functions and, therefore, explicit formulas for computing the weighting coefficients of the first-order derivative can be obtained as follows [Shu and Richards 1992a]:

$$A_{ik}^{(1)}=\frac{\prod(x_i)}{(x_i-x_k)\prod(x_k)} \quad \text{for} \quad i,k=1,2,\dots,N_x \quad \text{and} \quad k\ne i, \qquad \prod(x_i)=\prod_{\nu=1,\nu\ne k}^{N_x}(x_i-x_\nu). \tag{12}$$

For higher-order derivatives, one can use the following relations iteratively:

$$\begin{aligned} A_{ik}^{(r)} &= r\left[A_{ii}^{(r-1)}A_{ik}^{(1)} - \frac{A_{ik}^{(r-1)}}{x_i - x_k}\right] && \text{for } i,k = 1,2,\ldots,N_x \text{ and } \quad k \neq i, \quad 2 \leq r \leq (N_x - 1), \\ A_{ii}^{(r)} &= -\sum_{v=1,v\neq i}^{N_x} A_{iv}^{(r)} && \text{for } i = 1,2,\ldots,N_x, \quad 1 \leq r \leq (N_x - 1). \end{aligned} \tag{13}$$

The next step is the discretization of the domain to $N_\xi \times N_\eta$ grid points. It is shown [Shu et al. 2001] that one of the best options for obtaining grid points is zeros of the well-known Chebyshev polynomials:

$$\xi_i = -1 + \cos\left[\frac{(i-1)\pi}{N_\xi - 1}\right], \; i = 1,2,\ldots,N_\xi, \qquad \eta_j = -1 + \cos\left[\frac{(j-1)\pi}{N_\eta - 1}\right], \; j = 1,2,\ldots,N_\eta. \tag{14}$$

In DQEM, the procedure of the DQ method should be repeated for the governing equation within each element. Therefore, the governing equations (5) can be written in the computational domain as

$$\begin{aligned} &(\alpha\xi_{,x}^2 + \xi_{,y}^2)\sum_{k=1}^{N_\xi} A_{ik}^{(2)}u_{kj} + (\alpha\eta_{,x}^2 + \eta_{,y}^2)\sum_{l=1}^{N_\eta} B_{jl}^{(2)}u_{il} + (\alpha\xi_{,xx} + \xi_{,yy})\sum_{k=1}^{N_\xi} A_{ik}^{(1)}u_{kj} \\ &\qquad + (\alpha\eta_{,xx} + \eta_{,yy})\sum_{l=1}^{N_\eta} B_{jl}^{(1)}u_{il} + (2\alpha\xi_{,x}\eta_{,x} + 2\xi_{,y}\eta_{,y})\sum_{k=1}^{N_\xi} A_{ik}^{(1)}\sum_{l=1}^{N_\eta} B_{jl}^{(1)}u_{kl} \\ &\qquad + (\beta\xi_{,x}\xi_{,y})\sum_{k=1}^{N_\xi} A_{ik}^{(2)}v_{kj} + (\beta\eta_{,x}\eta_{,y})\sum_{l=1}^{N_\eta} B_{jl}^{(2)}v_{il} + (\beta\xi_{,xy})\sum_{k=1}^{N_\xi} A_{ik}^{(1)}v_{kj} \\ &\qquad\qquad + (\beta\eta_{,xy})\sum_{l=1}^{N_\eta} B_{jl}^{(1)}v_{il} + \beta(\xi_{,x}\eta_{,y} + \xi_{,y}\eta_{,x})\sum_{k=1}^{N_\xi} A_{ik}^{(1)}\sum_{l=1}^{N_\eta} B_{jl}^{(1)}v_{kl} = 0, \\ &(\xi_{,x}^2 + \alpha\xi_{,y}^2)\sum_{k=1}^{N_\xi} A_{ik}^{(2)}v_{kj} + (\eta_{,x}^2 + \alpha\eta_{,y}^2)\sum_{l=1}^{N_\eta} B_{jl}^{(2)}v_{il} + (\xi_{,xx} + \alpha\xi_{,yy})\sum_{k=1}^{N_\xi} A_{ik}^{(1)}v_{kj} \\ &\qquad + (\eta_{,xx} + \alpha\eta_{,yy})\sum_{l=1}^{N_\eta} B_{jl}^{(1)}v_{il} + (2\xi_{,x}\eta_{,x} + 2\alpha\xi_{,y}\eta_{,y})\sum_{k=1}^{N_\xi} A_{ik}^{(1)}\sum_{l=1}^{N_\eta} B_{jl}^{(1)}v_{kl} \\ &\qquad + (\beta\xi_{,x}\xi_{,y})\sum_{k=1}^{N_\xi} A_{ik}^{(2)}u_{kj} + (\beta\eta_{,x}\eta_{,y})\sum_{l=1}^{N_\eta} B_{jl}^{(2)}u_{il} + (\beta\xi_{,xy})\sum_{k=1}^{N_\xi} A_{ik}^{(1)}u_{kj} \\ &\qquad\qquad + (\beta\eta_{,xy})\sum_{l=1}^{N_\eta} B_{jl}^{(1)}u_{il} + \beta(\xi_{,x}\eta_{,y} + \xi_{,y}\eta_{,x})\sum_{k=1}^{N_\xi} A_{ik}^{(1)}\sum_{l=1}^{N_\eta} B_{jl}^{(1)}u_{kl} = 0. \end{aligned}$$

2.5. ***Compatibility, loading, and boundary conditions.*** Assuming a perfectly bonded interface between the fiber and matrix, the following displacement continuity and traction reciprocity conditions should be satisfied at the common nodes of the two adjacent elements:

$$u^a = u^b, \quad v^a = v^b, \quad \sigma_x^a \cdot n_1 + \tau_{xy}^a \cdot n_2 = \sigma_x^b \cdot n_1 + \tau_{xy}^b \cdot n_2, \quad \tau_{xy}^a \cdot n_1 + \sigma_y^a \cdot n_2 = \tau_{xy}^b \cdot n_1 + \sigma_y^b \cdot n_2, \tag{15}$$

where a and b refer to two adjacent elements and $n = (n_1, n_2)$ is unit normal to the interface. Furthermore, appropriate loading and boundary conditions for the normal loading of the RVE in the transverse and axial directions are (Figure 1):

$$\begin{aligned}
&u = \tau_{xy} = 0 && && \text{on} \quad x = 0,\\
&v = \tau_{xy} = 0 && && \text{on} \quad y = 0,\\
&u = \text{const.}, && \tau_{xy} = 0, \quad \int_0^{L_2} \sigma_x \, dy = \sigma_{x0} L_2 && \text{on} \quad x = L_1,\\
&v = \text{const.}, && \tau_{xy} = 0, \quad \int_0^{L_1} \sigma_y \, dx = \sigma_{y0} L_1 && \text{on} \quad y = L_2,\\
&\varepsilon_{z0} = \text{const.}, && \int_0^{L_1}\!\!\int_0^{L_2} \sigma_z \, dx dy = \sigma_{z0} L_1 L_2 && \text{on the RVE,}
\end{aligned} \tag{16}$$

in which σ_{x0}, σ_{y0}, and σ_{z0} are the applied macrostress components on the RVE in the x, y, and z directions, respectively. The compatibility conditions at the element interface and the boundary conditions have a dominant influence on the accuracy of the results and, therefore, (15) and (16) should be mapped to the computational domain and discretized carefully.

Application of DQEM to the problem together with the boundary and compatibility conditions leads to an overdetermined system of algebraic linear equations $Ax = b$, that is, A is a rectangular matrix of size $m \times n$, $n < m$. In order to solve the nonsymmetric linear system $Ax = b$, one may use an equivalent system,

$$A^T A x = A^T b, \tag{17}$$

which is symmetric positive definite. This system is known as the system of the normal equations associated with the following least-squares problem:

$$\text{minimize } \|b - Ax\|_2, \tag{18}$$

in which $\|b - Ax\|_2 \equiv \left(\sum_{i=1}^{m} [b_i - \sum_{j=1}^{n} A_{ij} x_j]^2\right)^{1/2}$. It can be shown that minimizing (18), which is a least-squares solution for the nonsymmetric linear system $Ax = b$, leads to the symmetric system (17); see, for instance, [Saad 2003] for more details.

Finally, it is interesting to note that application of DQEM leads to a compatible overdetermined system of equations, and therefore, the above-mentioned least-squares technique results in accurate predictions.

3. Numerical results and discussion

The procedure explained in the previous sections is used to obtain stress and displacement components within the fiber and matrix of a SiC/Ti metal matrix composite with a 40% fiber volume fraction (FVF). The composite is subjected to normal loading in the axial and transverse directions. Various overall properties of the composite system can also be determined by applying uniaxial loads. The mechanical properties of the constituents of the SiC/Ti system are as follows (see [Aghdam et al. 2000]):

SiC (fiber): $E = 409\,\text{GPa}$ $\nu = 0.2$
Ti (matrix): $E = 107\,\text{GPa}$ $\nu = 0.3$

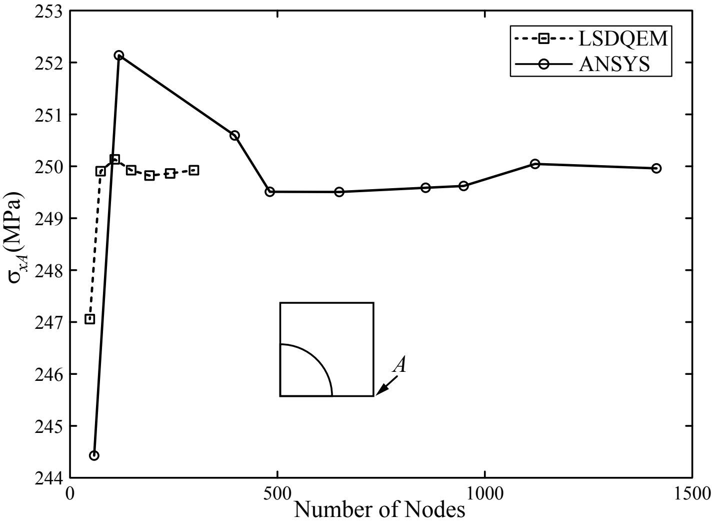

Figure 4. Convergence of transverse normal stress σ_x at point A, with $\varepsilon_{x0} = 0.001$.

3.1. ***Convergence study and CPU time.*** In this section, the convergence rate and CPU time of the presented method are compared with those of ANSYS and a mesh-free method for two examples. In the first example, a UD SiC/Ti metal matrix composite with a 40% FVF is considered. The RVE is subjected to a uniform strain of $\varepsilon_{x0} = 0.001$ in the x direction on the right-hand side, while all other stress and strain components are zero. Figure 4 represents the convergence of the transverse normal stress σ_x at point A of the RVE. The figure also includes convergence of the same results obtained by the commercial finite element code ANSYS [ANSYS 2008]. The geometry of the RVE in the ANSYS simulation is modeled by two-dimensional generalized plane strain PLANE183 elements with eight nodes. The results suggest that very good convergence can be achieved by using about 100 nodes in LSDQEM while FEM analysis requires more than 1000 nodes for the same level of convergence.

The efficiency of the presented method is examined in another example in which a boron/aluminum metal matrix composite with a 47% FVF is considered. The material properties of the constituents are as follows:

Boron (fiber)	$E = 379.3\,\text{GPa}$	$\nu = 0.2$
Aluminum (matrix)	$E = 68.3\,\text{GPa}$	$\nu = 0.3$

The overall transverse Young's modulus of the boron/aluminum composite (E_T^c) is calculated using three different methods including the presented LSDQEM, FEM (ANSYS), and meshless method [Ahmadi and Aghdam 2010]. The CPU times for these methods are tabulated in Table 1. Again, it can be

Method	Number of nodes	CPU time (s)	E_T^c (GPa)
LSDQEM	108	6	143.92
FEM (ANSYS)	1200	~15	143.96
Meshless method [Ahmadi and Aghdam 2010]	350	14.9	144.31

Table 1. Comparison of the CPU time for LSDQEM and other methods (FVF = 0.47).

seen that the number of nodes and the CPU time for LSDQEM are significantly less than for the other two methods which implies efficiency for the presented method. The predictions of the presented model for the transverse Young's modulus (E_T^c) are also in excellent agreement with the predictions of ANSYS.

3.2. *Stress analysis.*

Transverse normal loading. In this section, the SiC/Ti composite system with a 40% FVF subjected to a transverse strain of $\varepsilon_{x0} = 0.001$ in the x direction is considered. The RVE is assumed to be square, that is, $L_1 = L_2$. In order to examine the validity of the results, another analysis was also carried out using the finite element code ANSYS [ANSYS 2008]. All the predicted stress and displacement components show excellent agreement with the finite element results for the entire domain of the problem. For example, the comparison of the normal stress σ_x is presented in Figure 5. The stresses and displacements within the

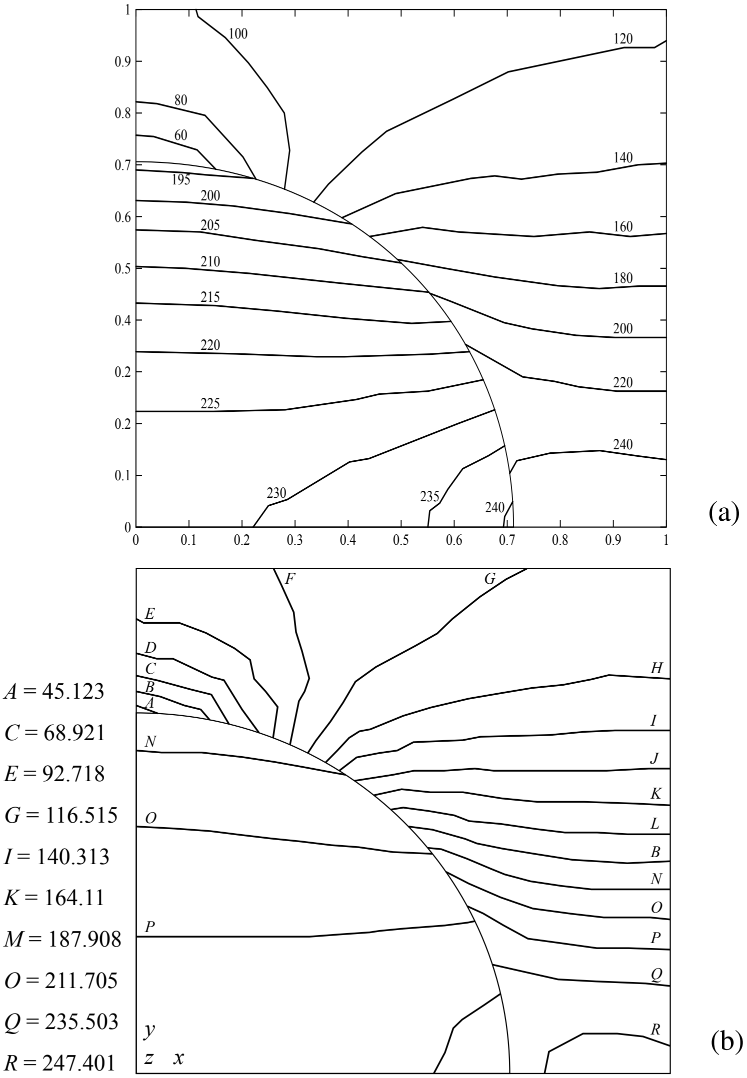

Figure 5. Contours of normal stress σ_x (in MPa) in the RVE of (a) DQEM and (b) ANSYS.

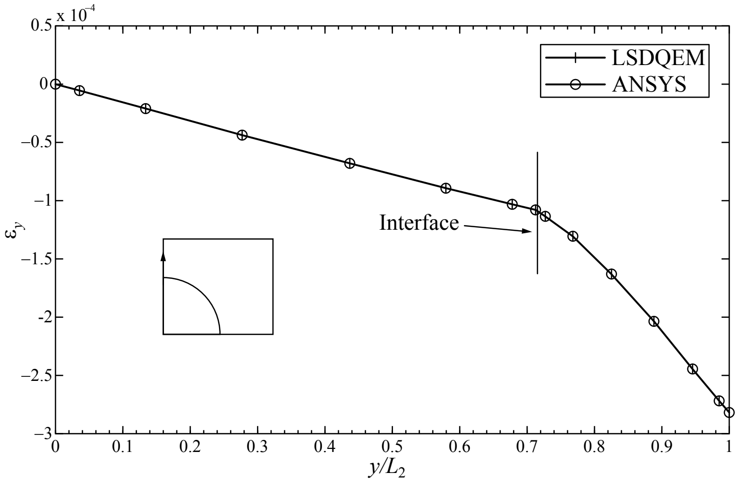

Figure 6. Comparison of ε_y along the y-axis, with $\varepsilon_{x0} = 0.001$.

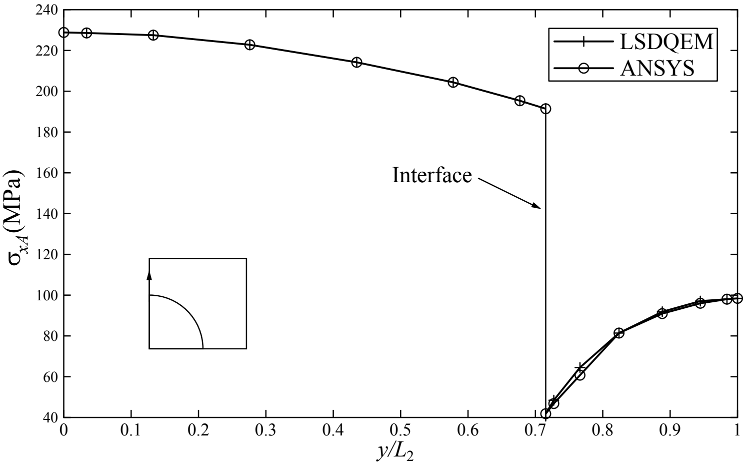

Figure 7. Comparison of normal stress σ_x along the y-axis, with $\varepsilon_{x0} = 0.001$.

RVE are compared with the finite element results in Figures 6–8. As expected, it can be seen in Figures 6–8 that ε_y and σ_y are continuous along the y-axis while σ_x and σ_z are discontinuous at the fiber-matrix interface. Furthermore the SiC/Ti composite is subjected to a uniaxial transverse normal load in the x direction, $\sigma_x = 100\,\text{MPa}$. The dimensionless stress σ^* is defined as the ratio of the microstress σ to the applied macrostress $\overline{\sigma} = 100\,\text{MPa}$, that is, $\sigma^* = \sigma/100$. The distribution of the dimensionless normal and effective von Mises σ_e^* stresses on the x and y axes of the RVE are shown in Figures 9 and 10. It is seen that on the x-axis the microstress σ_x^* is greater than the applied macrostress. The coefficient of stress concentration for transverse loading is $\sigma_{x\,\max}/\sigma_x = 1.4$. As expected, it can also be seen that σ_x along the x-axis (Figure 9) and σ_y along the y-axis (Figure 11) are continuous, while the other stresses are discontinuous at the fiber-matrix interface.

Axial normal stress loading. The uniaxial axial normal load in the z direction, $\sigma_z = 100\,\text{MPa}$, is applied to a SiC/Ti composite system. The resultant dimensionless normal and effective von Mises σ_e^* stresses

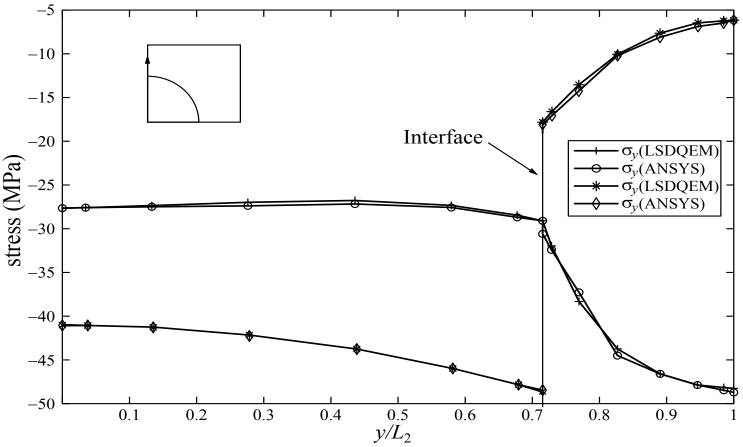

Figure 8. Comparison of normal stresses (σ_y, σ_z) along the y-axis, with $\varepsilon_{x0} = 0.001$.

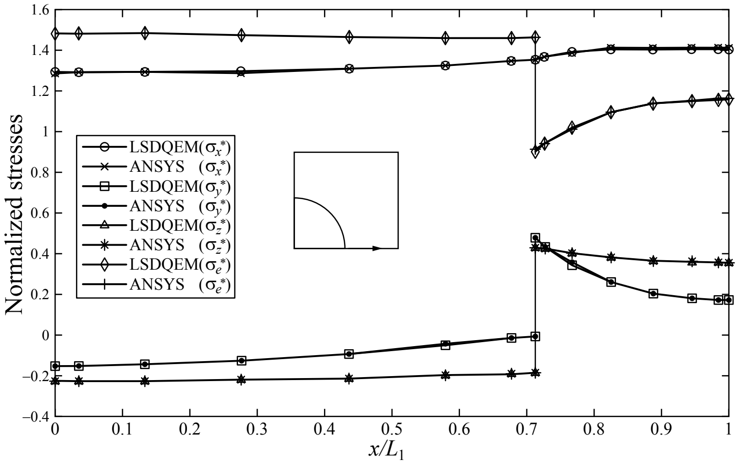

Figure 9. Comparison of normalized stresses along the x-axis, with $\sigma_x = 100\,\text{MPa}$.

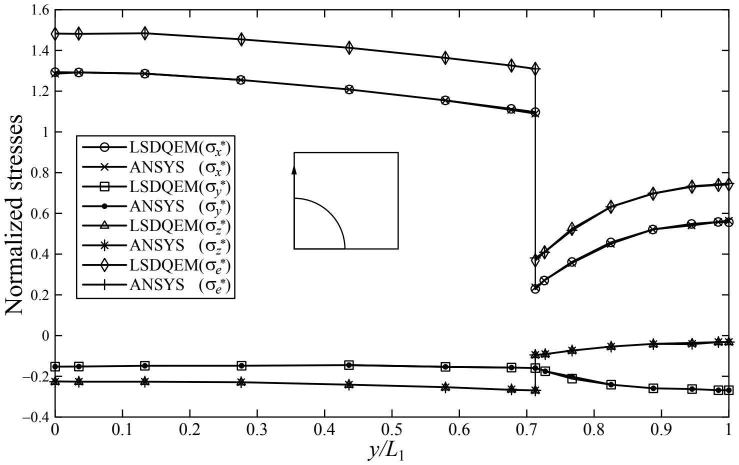

Figure 10. Comparison of normalized stresses along the y-axis, with $\sigma_x = 100\,\text{MPa}$.

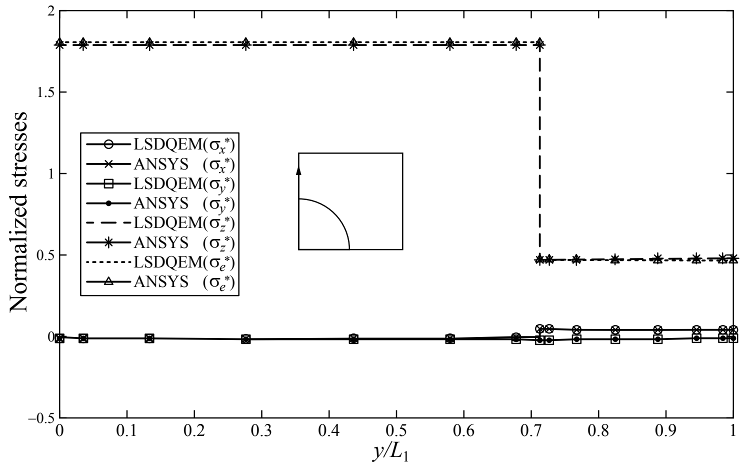

Figure 11. Comparison of normalized stresses along the y-axis, with $\sigma_z = 100\,\text{MPa}$.

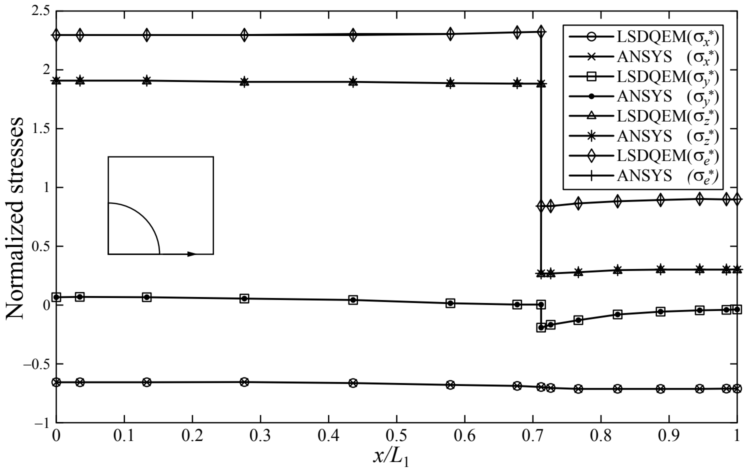

Figure 12. Comparison of normalized stresses along the x-axis, with $\sigma_x = -50\,\text{MPa}$, $\sigma_z = 100\,\text{MPa}$.

on the y-axis of the RVE are shown in Figure 11. It is seen that the microstress σ_z^* within the fiber is greater than the applied macrostress. The coefficient of stress concentration for the axial loading is $\sigma_{z\,\max}/\sigma_z = 1.79$. As expected, σ_z is nearly constant within the fiber and matrix with larger a value in the fiber which results from the generalized plane strain assumption and all other stress components are nearly zero.

Biaxial normal stress loading. In the next example, the SiC/Ti composite system subjected to a biaxial normal stress of $\sigma_x = -50\,\text{MPa}$, $\sigma_z = 100\,\text{MPa}$ is studied. The dimensionless normal and effective von Mises σ_e^* stresses on the x axis of the RVE are shown in Figure 12. It can be seen that σ_x along the x-axis, Figure 12, is continuous while the other stresses are discontinuous at the fiber-matrix interface. Furthermore σ_z is nearly constant within the fiber and matrix.

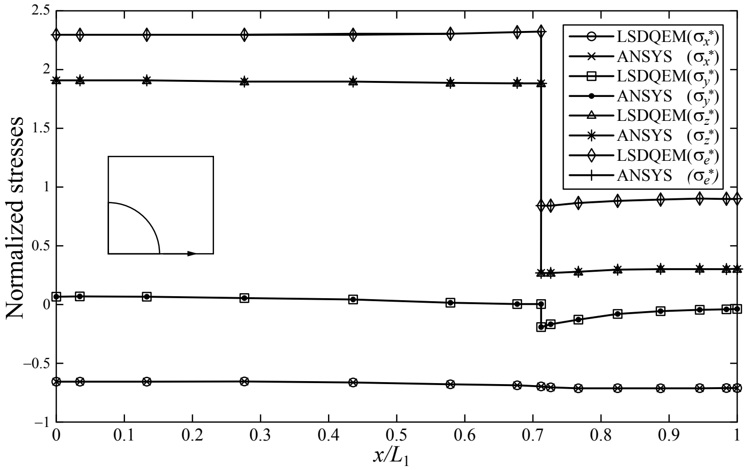

Figure 13. Comparison of normalized stresses along the x-axis, with $\sigma_x = -50\,\text{MPa}$, $\sigma_y = 80\,\text{MPa}$, $\sigma_z = 100\,\text{MPa}$.

Triaxial normal stress loading. Finally, the SiC/Ti composite system subjected to a triaxial normal stress of $\sigma_x = -50\,\text{MPa}$, $\sigma_y = 80\,\text{MPa}$, $\sigma_z = 100\,\text{MPa}$ is considered. The distribution of the dimensionless stresses on the x-axis of the RVE is shown in Figure 13. All the predicted stress components show excellent agreement with the finite element results.

3.3. ***Elastic properties.*** In order to obtain the overall mechanical properties of the composite system, the square RVE is analyzed using uniaxial loadings in the transverse and longitudinal directions. For instance, the RVE is subjected to a uniform stress in the x direction (σ_{x0}) while the other stress components (σ_{y0}, σ_{z0}) are zero. Then, the overall strain of the RVE in the x and y directions ($\varepsilon_{x0}, \varepsilon_{y0}$) can be determined. The transverse Young's modulus and Poisson's ratio can be calculated using

$$E_T^c = \sigma_{x0}/\varepsilon_{x0}, \qquad \nu_T^c = |\varepsilon_{y0}/\varepsilon_{x0}|, \tag{19}$$

in which the superscript c refers to the overall composite property. A similar procedure can be used to obtain the axial properties of the composite system. Predictions for the overall transverse Young's modulus, E_T^c, of the SiC/Ti are shown in Table 1. It should be noted that three elements with 8×8 grid points are considered in the presented DQEM while more elements are used in the finite element analysis.

Included in Table 2 are also results from finite element analysis [Aghdam et al. 2000] and the method of cells (MC) [Aboudi 1987]. As can be seen in Table 2, all the predictions are in close agreement with each other. It should be noted that due to geometrical restrictions for the square array fiber assumption, the maximum fiber volume fraction (FVF) for both the finite element method and DQEM is 0.785. The predictions for the overall transverse Poisson's ratio, ν_T^c, for the same material are shown in Table 2. Again, excellent agreement can be seen between the DQEM and finite element results while the results of MC shows an overestimate for the entire range of the FVF. The predictions for the overall longitudinal Young's modulus, E_L^c, and Poisson's ratio, ν_L^c, of the SiC/Ti composite system are depicted in Table 2.

FVF	Solution method	E_L^c (GPa)	ν_L^c	E_T^c (GPa)	ν_T^c
20%	LSDQEM	167.63	0.2766	136.66	0.3103
	ANSYS	167.62	0.2766	136.74	0.3099
	FEM	168.80	0.2612	136.91	0.3102
	MC	167.93	0.2637	135.18	0.323
40%	LSDQEM	228.13	0.2550	177.86	0.2820
	ANSYS	228.12	0.2550	177.93	0.2818
	FEM	228.61	0.2252	177.75	0.2822
	MC	227.75	0.2274	169.5	0.3130
60%	LSDQEM	288.56	0.2348	234.46	0.2450
	ANSYS	288.54	0.2348	234.35	0.2455
	FEM	289.30	0.1913	243.23	0.2458
	MC	288.86	0.1929	217.29	0.2885

Table 2. Comparison of the longitudinal (axial) and transverse Young's moduli and Poisson's ratios for various fiber volume fractions (FVF). The FEM values are from [Aghdam et al. 2000] and the method of cells (MC) values from [Aboudi 1987].

The predictions of the MC and finite element analysis are also included in the table. The MC predictions can be obtained by the closed form solutions given in [Aboudi 1987].

4. Concluding remarks

A micromechanical model is developed to predict the behavior of a unidirectional (UD) fiber-reinforced composite subjected to various axial and transverse normal loading conditions using the differential quadrature element method (DQEM). The theory of elasticity is used to derive the governing partial differential equations of the problem. The geometry of the representative volume element (RVE) is then divided into three elements and mapping is used to convert the solution domain to a computational square domain. The new versions of the governing equations and boundary conditions are derived.

The application of DQEM for this problem leads to an overdetermined system of linear equations since the RVE has particular boundary conditions. The least-squares approximation is used to solve the resultant system of equations. It is demonstrated that the least-squares differential quadrature element method (LSDQEM) is a simple and fast approach to imposing the various boundary conditions of the problem. It can be seen that the number of nodes and the CPU time for LSDQEM are significantly less than for the mesh-free method and FEM. Comparison of the predicted results for various stress and displacement components shows excellent agreement with the finite element method. Moreover, results for overall the mechanical properties of the UD composites also show excellent agreement with other published analytical and finite element models. In addition, the model has the advantage over conventional analytical models of making fewer simplifying assumptions on the geometry of the RVE.

References

[Aboudi 1987] J. Aboudi, "Closed form constitutive equations for metal matrix composites", *Int. J. Eng. Sci.* **25**:9 (1987), 1229–1240.

[Aboudi 1989] J. Aboudi, "Micromechanical analysis of composites by the method of cells", *Appl. Mech. Rev.* (*ASME*) **42**:7 (1989), 193–221.

[Adams 1970] D. F. Adams, "Inelastic analysis of a unidirectional composite subjected to transverse normal loading", *J. Compos. Mater.* **4**:3 (1970), 310–328.

[Adams and Doner 1967] D. F. Adams and D. R. Doner, "Transverse normal loading of a unidirectional composite", *J. Compos. Mater.* **1**:2 (1967), 152–164.

[Aghdam and Dezhestan 2005] M. M. Aghdam and A. Dezhestan, "Micromechanics based analysis of randomly distributed fiber reinforced composites using simplified unit cell model", *Compos. Struct.* **71**:3–4 (2005), 327–332.

[Aghdam et al. 2000] M. M. Aghdam, M. J. Pavier, and D. J. Smith, "Finite element micromechanical modelling of yield and collapse behaviour of metal matrix composites", *J. Mech. Phys. Solids* **48**:3 (2000), 499–528.

[Aghdam et al. 2001] M. M. Aghdam, M. J. Pavier, and D. J. Smith, "Micro-mechanics of off-axis loading of metal matrix composites using finite element analysis", *Int. J. Solids Struct.* **38**:22–23 (2001), 3905–3925.

[Ahmadi and Aghdam 2010] I. Ahmadi and M. M. Aghdam, "Micromechanics of fibrous composites subjected to combined shear and thermal loading using a truly meshless method", *Comput. Mech.* **46**:3 (2010), 387–398.

[ANSYS 2008] *ANSYS user's manual*, Version 11.0, Swanson Analysis Systems, Houston, TX, 2008.

[Bert and Malik 1996] C. W. Bert and M. Malik, "Differential quadrature method in computational mechanics: a review", *Appl. Mech. Rev.* (*ASME*) **49**:1 (1996), 1–28.

[Bert et al. 1993] C. W. Bert, X. Wang, and A. G. Striz, "Differential quadrature for static and free vibrational analyses of anisotropic plates", *Int. J. Solids Struct.* **30**:13 (1993), 1737–1744.

[Chen 2003] C.-N. Chen, "DQEM and DQFDM for the analysis of composite two-dimensional elasticity problems", *Compos. Struct.* **59**:1 (2003), 3–13.

[Eischen and Torquato 1993] J. W. Eischen and S. Torquato, "Determining elastic behavior of composites by the boundary element method", *J. Appl. Phys.* **74**:1 (1993), 159–170.

[Eshelby 1957] J. D. Eshelby, "The determination of the elastic field of an ellipsoidal inclusion, and related problems", *Proc. R. Soc. Lond. A* **241**:1226 (1957), 376–396.

[Hashin and Rosen 1964] Z. Hashin and B. W. Rosen, "The elastic moduli of fiber-reinforced materials", *J. Appl. Mech.* (*ASME*) **31**:2 (1964), 223–232.

[Hill 1965] R. Hill, "A self-consistent mechanics of composite materials", *J. Mech. Phys. Solids* **13**:4 (1965), 213–222.

[Jang et al. 1989] S. K. Jang, C. W. Bert, and A. G. Striz, "Application of differential quadrature to static analysis of structural components", *Int. J. Numer. Methods Eng.* **28**:3 (1989), 561–577.

[Karami and Malekzadeh 2002] G. Karami and P. Malekzadeh, "A new differential quadrature methodology for beam analysis and the associated differential quadrature element method", *Comput. Methods Appl. Mech. Eng.* **191**:32 (2002), 3509–3526.

[Malik and Bert 1996] M. Malik and C. W. Bert, "Implementing multiple boundary conditions in the DQ solution of higher-order PDEs: application to free vibration of plates", *Int. J. Numer. Methods Eng.* **39**:7 (1996), 1237–1258.

[Mikata and Taya 1985] Y. Mikata and M. Taya, "Stress field in a coated continuous fiber composite subjected to thermo-mechanical loadings", *J. Compos. Mater.* **19**:6 (1985), 554–578.

[Nairn 1985] J. A. Nairn, "Thermoelastic analysis of residual stresses in unidirectional, high-performance composites", *Polym. Compos.* **6**:2 (1985), 123–130.

[Nedele and Wisnom 1994] M. R. Nedele and M. R. Wisnom, "Finite element micromechanical modelling of a unidirectional composite subjected to axial shear loading", *Composites* **25**:4 (1994), 263–272.

[Nimmer 1990] R. P. Nimmer, "Fiber-matrix interface effects in the presence of thermally induced residual stress", *J. Compos. Technol. Res.* **12**:2 (1990), 65–75.

[Robertson and Mall 1993] D. D. Robertson and S. Mall, "Micromechanical relations for fiber-reinforced composites using the free transverse shear approach", *J. Compos. Technol. Res.* **15**:3 (1993), 181–192.

[Saad 2003] Y. Saad, *Iterative methods for sparse linear systems*, 2nd ed., Chapter 8, pp. 245–259, SIAM, Philadelphia, 2003.

[Shu and Richards 1992a] C. Shu and B. E. Richards, "Application of generalized differential quadrature to solve two dimensional incompressible Navier–Stokes equations", *Int. J. Numer. Methods Fluids* **15**:7 (1992), 791–798.

[Shu and Richards 1992b] C. Shu and B. E. Richards, "Parallel simulation of incompressible viscous flows by generalized differential quadrature", *Comput. Sys. Eng.* **3**:1–4 (1992), 271–281.

[Shu et al. 2001] C. Shu, W. Chen, H. Xue, and H. Du, "Numerical study of grid distribution effect on accuracy of DQ analysis of beams and plates by error estimation of derivative approximation", *Int. J. Numer. Methods Eng.* **51**:2 (2001), 159–179.

[Sun and Vaidya 1996] C. T. Sun and R. S. Vaidya, "Prediction of composite properties from a representative volume element", *Compos. Sci. Technol.* **56**:2 (1996), 171–179.

[Uemura et al. 1979] M. Uemura, H. Iyama, and Y. Yamaguchi, "Thermal residual stresses in filament-wound carbon-fiber-reinforced composites", *J. Therm. Stresses* **2**:3–4 (1979), 393–412.

[Wang 2001] Y. Wang, *Differential quadrature method and differential quadrature element method-theory and practice*, Ph.D. thesis, Nanjing University of Aeronautics and Astronautics, Nanjing, 2001. In Chinese.

[Wang and Bert 1993] X. Wang and C. W. Bert, "A new approach in applying differential quadrature to static and free vibrational analyses of beam and plates", *J. Sound Vib.* **162**:3 (1993), 566–572.

[Wang and Gu 1997] X. Wang and H. Gu, "Static analysis of frame structures by the differential quadrature element method", *Int. J. Numer. Methods Eng.* **40**:4 (1997), 759–772.

[Wang et al. 1996] X. Wang, H. Gu, and B. Liu, "On buckling analysis of beams and frame structures by the differential quadrature element method", pp. 382–385 in *Engineering mechanics: proceedings of the 11th conference* (Fort Lauderdale, FL, 1996), vol. 1, edited by Y. K. Lin and T. C. Su, ASCE, New York, 1996.

[Wu and Liu 2000] T. Y. Wu and G. R. Liu, "Application of generalized differential quadrature rule to sixth-order differential equations", *Commun. Numer. Methods Eng.* **16**:11 (2000), 777–784.

[Zong and Zhang 2009] Z. Zong and Y. Zhang, *Advanced differential quadrature methods*, CRC Press, Boca Raton, FL, 2009.

Received 22 Dec 2010. Revised 14 Jun 2011. Accepted 19 Aug 2011.

MOHAMMAD BAYAT: `mbayat@aut.ac.ir`
Department of Mechanical Engineering, Amirkabir University of Technology, 424 Hafez Avenue, Tehran 15875-4413, Iran

MOHAMMAD MOHAMMADI AGHDAM: `aghdam@aut.ac.ir`
Department of Mechanical Engineering, Amirkabir University of Technology, 424 Hafez Avenue, Tehran 15875-4413, Iran
http://me.aut.ac.ir/M.Aghdam.htm

JOURNAL OF MECHANICS OF MATERIALS AND STRUCTURES
Vol. 7, No. 2, 2012

SIZE-DEPENDENT FREE VIBRATION ANALYSIS OF INFINITE NANOTUBES USING ELASTICITY THEORY

JAFAR ESKANDARI JAM, YASER MIRZAEI, BEHNAM GHESHLAGHI AND REZA AVAZMOHAMMADI

Exact elasticity theory is employed to study the (two-dimensional) free vibration of nanoscale cylindrical tubes in the presence of free surface energy. Use is made of the Gurtin–Murdoch surface elasticity model to incorporate the surface stress terms into the pertinent boundary conditions. Some numerical examples are provided to depict the influence of the surface energy, and particularly the inner radius size of the nanocylinder, on the natural frequencies of the system. The results indicate a stronger influence of surface effects for both smaller values of the outer to inner radius ratio and higher modes of vibration.

1. Introduction

Due to accelerated miniaturization of components and devices in micro and nanoelectromechanical systems, there is an increasing demand for understanding of the behaviors of small-sized materials and structures. Nanostructured devices and materials have become progressively more important both in fundamental and applied research because of their unique physical properties [Tan and Lim 2006]. When the characteristic size of materials and devices shrinks to microns or nanometers, surface and interface effects start to play a considerable or even dominant role in their deformability, performance, and reliability, owing to the increasing ratio of surface/interface area to volume [Wong et al. 1997; Cuenot et al. 2004]. Also, atomic simulations have revealed that a solid surface/interface may be either elastically softer or stiffer than its bulk counterparts [Benveniste and Miloh 2001; Zhou and Huang 2004].

A continuum model of surface elasticity was first established in [Gurtin and Murdoch 1975] to account for the effects of surfaces, and further extended in [Gurtin et al. 1998] to incorporate the effects of interfaces as well. Surface elastic constants can be obtained through atomic calculations [Shenoy 2005]; their direct measurement has been very difficult until now. Investigations of the deformation of some elementary nanosized devices (for example, beams, tubes, and plates) have demonstrated that the predictions of Gurtin's surface/interface elasticity theory agree reasonably well with direct atomic simulations [Miller and Shenoy 2000; Shenoy 2002].

Although surface elasticity theory has been extensively used to elucidate the effects of various size-dependent phenomena on elastic fields in nanowires caused by static loadings [Chen et al. 2006; Jing et al. 2006], to date, however, investigation of surface effects on the dynamic behaviors of long nanotubes/nanowires has been comparatively lacking. As a few examples in the context of dynamic loadings in conjunction with surface elasticity theory, we mention studies regarding the diffraction of plane compressional/shear waves by nanosized inhomogeneities/voids (embedded in an elastic medium) [Wang 2007; Hasheminejad and Avazmohammadi 2009] which demonstrate the considerable importance of the

---

Yaser Mirzaei is the corresponding author.

Keywords: free surface energy, free vibration, nanotube, elasticity solution.

surface effects on dynamic stress concentration around the nanoinhomogeneities. He and Lilley [2008] studied the influence of the surface stress on the resonance frequencies of bending nanowires using Euler–Bernoulli beam theory and, similarly, the natural frequencies of a microbeam in the presence of surface effects were estimated in [Abbasion et al. 2009] based on Timoshenko beam theory. Furthermore, in [Hasheminejad and Gheshlaghi 2010] a dissipative surface stress model was adopted to study the effect of size-dependent surface dissipation on natural frequencies of vibrating elastic nanowires. Nevertheless, as far as the authors know, investigation of surface effects on the natural frequencies of nanosized cylindrical tubes is still lacking. Here, we make use of classical elasticity theory in conjunction with Gurtin–Murdoch theory to carry out a (exact) two-dimensional natural frequency analysis of long, nanosized cylindrical tubes (nanotubes) in presence of free surface-energy effects.

2. Formulation

The elastic material of the nanotube (NT) under consideration is assumed to be linear, macroscopically homogeneous, and isotropic. Its constitutive equation may be written as

$$\sigma_{ij} = \lambda \delta_{ij} \varepsilon_{jj} + 2\mu \varepsilon_{ij}, \tag{1}$$

where δ_{ij} is the Kronecker delta, (λ, μ) are the Lamé constants, and σ_{ij} and ε_{ij} are the stress and the strain tensors, respectively. The problem can be analyzed by means of the standard methods of elastodynamics. In the absence of body forces, the displacement field is governed by the classical Navier's equation [Pao and Mow 1973]

$$\rho \frac{\partial^2 \boldsymbol{u}}{\partial \boldsymbol{t}^2} = \boldsymbol{\mu} \nabla^2 \boldsymbol{u} + (\lambda + \mu) \nabla (\nabla \cdot \boldsymbol{u}), \tag{2}$$

subjected to appropriate boundary conditions. Here, ρ is the elastic material density and $\boldsymbol{u}$ is the displacement vector that can advantageously be expressed as sum of the gradient of a scalar potential and the curl of a vector potential:

$$\boldsymbol{u} = \nabla \varphi + \nabla \times \boldsymbol{\psi}, \tag{3}$$

with the condition $\nabla \cdot \boldsymbol{\psi} = 0$. The above decomposition enables us to separate the dynamic equation of motion (2) into the Helmholtz wave equations

$$c_p^2 \nabla^2 \varphi = \ddot{\varphi}, \quad c_s^2 \nabla^2 \boldsymbol{\psi} = \ddot{\boldsymbol{\psi}}, \tag{4}$$

where $c_p^2 = (\lambda + 2\mu)/\rho$ and $c_s^2 = \mu/\rho$ are the propagation velocities of compressional and shear waves in the elastic medium, respectively, and superposed dots stand for the time derivative. Taking the divergence-free condition of $\boldsymbol{\psi}$ into account, only two of the three components of $\boldsymbol{\psi}$ remain independent. Also, considering the plane-strain assumption, (4) can be reduced to the following fully uncoupled scalar wave equations (see [Hasheminejad and Mirzaei 2009, Equations (b-2)]):

$$c_p^2 \nabla^2 \phi = \ddot{\phi}, \quad c_s^2 \nabla^2 \psi = \ddot{\psi}. \tag{5}$$

Furthermore, the relevant displacement components in polar coordinates, (r, θ), in terms of compressional and shear wave potentials may be simply written as [Pao and Mow 1973]

$$u_r = \frac{\partial \phi}{\partial r} + \frac{1}{r}\frac{\partial \psi}{\partial \theta}, \quad u_\theta = \frac{1}{r}\frac{\partial \phi}{\partial \theta} - \frac{\partial \psi}{\partial r}. \tag{6}$$

Correspondingly, the relevant stress components are

$$\sigma_{rr} = \lambda\nabla^2\varphi + 2\mu\left[\frac{\partial^2\varphi}{\partial r^2} + \frac{\partial}{\partial r}\left(\frac{1}{r}\frac{\partial\psi}{\partial\theta}\right)\right], \quad \sigma_{r\theta} = \mu\left\{2\frac{\partial}{\partial r}\left(\frac{1}{r}\frac{\partial\varphi}{\partial\theta}\right) + \frac{1}{r^2}\frac{\partial^2\psi}{\partial\theta^2} - r\frac{\partial}{\partial r}\left(\frac{1}{r}\frac{\partial\psi}{\partial r}\right)\right\}. \tag{7}$$

Consider a long cylindrical NT with inner and outer radii a and b, respectively. The in-plane cross section of the NT is shown in Figure 1. The field expansions for the standing compressional and shear waves within the tube (that is, the solutions to the wave equations (5)) with respect to the polar coordinate system may be written as [Pao and Mow 1973]

$$\varphi(r,\theta,\omega) = \sum_{n=0}^{\infty}[a_n J_n(\alpha r) + b_n Y_n(\alpha r)]e^{in\theta}, \quad \psi(r,\theta,\omega) = \sum_{n=0}^{\infty}[c_n J_n(\beta r) + d_n Y_n(\beta r)]e^{in\theta}, \tag{8}$$

where $i = \sqrt{-1}$, a_n through d_n are unknown modal coefficients, $\alpha = \omega/c_p$ and $\beta = \omega/c_s$ are the compressional and shear wave numbers, respectively, J_n and Y_n are the cylindrical Bessel functions of the first and second kind, respectively, and $\boldsymbol{\omega}$ is the circular frequency. Substituting (8) into (7), the relevant stress components can be respectively written as

$$\begin{aligned}
\sigma_{rr}(r,\theta,\omega) &= \sum_{n=0}^{\infty}\big(a_n T_{1n}^{(1)} + b_n T_{1n}^{(2)} + c_n T_{2n}^{(1)} + d_n T_{2n}^{(2)}\big)e^{in\theta},\\
\sigma_{r\theta}(r,\theta,\omega) &= \sum_{n=0}^{\infty}\big(a_n T_{3n}^{(1)} + b_n T_{3n}^{(2)} + c_n T_{4n}^{(1)} + d_n T_{4n}^{(2)}\big)e^{in\theta},
\end{aligned} \tag{9}$$

in which

$$\begin{aligned}
T_{1n}^{(i)}(r,\omega) &= -2\mu\frac{\alpha}{r}\ell_{n-1}^{(i)}(\alpha r) + \left[2\mu\frac{n(1+n)}{r^2} - (\lambda+2\mu)\alpha^2\right]\ell_n^{(i)}(\alpha r),\\
T_{2n}^{(i)}(r,\omega) &= 2i\mu n\left[\frac{\beta}{r}\ell_{n-1}^{(i)}(\beta r) - \frac{(1+n)}{r^2}\ell_n^{(i)}(\beta r)\right],\\
T_{3n}^{(i)}(r,\omega) &= 2i\mu n\left[\frac{\alpha}{r}\ell_{n-1}^{(i)}(\alpha r) - \frac{(1+n)}{r^2}\ell_n^{(i)}(\alpha r)\right],\\
T_{4n}^{(i)}(r,\omega) &= 2\mu\frac{\beta}{r}\ell_{n-1}^{(i)}(\beta r) + \mu\left[-2\frac{n(1+n)}{r^2} + \beta^2\right]\ell_n^{(i)}(\beta r),
\end{aligned} \tag{10}$$

where $i = 1, 2$ and

$$\ell_n^{(i)} = \begin{cases} J_n & (i=1),\\ Y_n & (i=2).\end{cases}$$

According to surface elasticity theory, a surface is considered as a negligibly thin layer adhered to an abutting bulk material without slipping [Gurtin and Murdoch 1975; Gurtin et al. 1998]. The equilibrium and constitutive equations in the abutting (bulk) solids are the same as those in classical elasticity theory. However, the surface has different elastic constants than the solids. Hence, in general, a nonzero surface stress associated with the (nonzero) surface constants should be taken into account in order to derive the (localized) equilibrium equations on the surface. Here, for the sake of brevity, we only provide the final set of pertinent nonclassical boundary conditions (caused by presence of the surface stress) in the polar

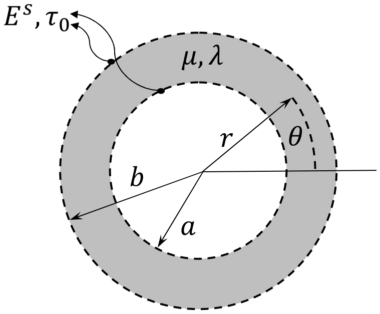

Figure 1. Problem geometry: two-dimensional view of the NT.

coordinate system [Wang et al. 2006]:

$$\sigma_{rr}(r=a,\theta,\omega)=\frac{1}{a}\sigma_{\theta\theta}^{(s)}(a,\theta,\omega),\qquad \sigma_{r\theta}(r=a,\theta,\omega)=-\frac{1}{a}\frac{\partial\sigma_{\theta\theta}^{(s)}(a,\theta,\omega)}{\partial\theta},\tag{11a}$$

$$\sigma_{rr}(r=b,\theta,\omega)=-\frac{1}{b}\sigma_{\theta\theta}^{(s)}(b,\theta,\omega),\qquad \sigma_{r\theta}(r=b,\theta,\omega)=\frac{1}{b}\frac{\partial\sigma_{\theta\theta}^{(s)}(b,\theta,\omega)}{\partial\theta},\tag{11b}$$

where $\sigma_{\theta\theta}^{(s)}(r,\theta,\omega)$ is the resultant surface stress at the surface with radius r and is written as

$$\sigma_{\theta\theta}^{(s)}(a,\theta,\omega)=\tau_0+E^s\varepsilon_{\theta\theta}(r=a,\theta,\omega),\quad \sigma_{\theta\theta}^{(s)}(b,\theta,\omega)=\tau_0+E^s\varepsilon_{\theta\theta}(r=b,\theta,\omega),\tag{12}$$

in which E^s is the (Young's modulus-type) elastic constant of the surface, $\varepsilon_{\theta\theta}=(\partial u_\theta/\partial\theta)/r$ and τ_0 is the surface residual stress whose effect is not taken into account here (that is, we assume $\tau_0=0$). Making use of (6) and (8), the strain component $\varepsilon_{\theta\theta}$ may be written as

$$\varepsilon_{\theta\theta}(r,\theta,\omega)=\sum_{n=0}^{\infty}\bigl(a_nT_{5n}^{(1)}+b_nT_{5n}^{(2)}+c_nT_{6n}^{(1)}+d_nT_{6n}^{(2)}\bigr)e^{in\theta},\tag{13}$$

where

$$T_{5n}^{(i)}(r,\omega)=r\alpha\ell_{n-1}^{(i)}(\alpha r)-n(1+n)\ell_n^{(i)}(\alpha r),\quad T_{6n}^{(i)}(r,\omega)=in\bigl(-r\beta\ell_{n-1}^{(i)}(\beta r)+(1+n)\ell_n^{(i)}(\beta r)\bigr).\tag{14}$$

Substitution of (9) and (12), along with (13), into the boundary conditions (11a) and (11b) leads to the following system of linear algebraic equations:

$$\begin{aligned}a_n\bigl(T_{1n}^{(1)}(a,\omega)-E^sT_{5n}^{(1)}(a,\omega)/a\bigr)+b_n\bigl(T_{1n}^{(2)}(a,\omega)-E^sT_{5n}^{(2)}(a,\omega)/a\bigr)\\+c_n\bigl(T_{2n}^{(1)}(a,\omega)-E^sT_{6n}^{(1)}(a,\omega)/a\bigr)+d_n\bigl(T_{2n}^{(2)}(a,\omega)-E^sT_{6n}^{(2)}(a,\omega)/a\bigr)=0,\end{aligned}\tag{15a}$$

$$\begin{aligned}a_n\bigl(T_{3n}^{(1)}(a,\omega)+inE^sT_{5n}^{(1)}(a,\omega)/a\bigr)+b_n\bigl(T_{3n}^{(2)}(a,\omega)+inE^sT_{5n}^{(2)}(a,\omega)/a\bigr)\\+c_n\bigl(T_{4n}^{(1)}(a,\omega)+inE^sT_{6n}^{(1)}(a,\omega)/a\bigr)+d_n\bigl(T_{4n}^{(2)}(a,\omega)+inE^sT_{6n}^{(2)}(a,\omega)/a\bigr)=0,\end{aligned}\tag{15b}$$

$$\begin{aligned}a_n\bigl(T_{1n}^{(1)}(b,\omega)+E^sT_{5n}^{(1)}(b,\omega)/b\bigr)+b_n\bigl(T_{1n}^{(2)}(b,\omega)+E^sT_{5n}^{(2)}(b,\omega)/b\bigr)\\+c_n\bigl(T_{2n}^{(1)}(b,\omega)+E^sT_{6n}^{(1)}(b,\omega)/b\bigr)+d_n\bigl(T_{2n}^{(2)}(b,\omega)+E^sT_{6n}^{(2)}(b,\omega)/b\bigr)=0,\end{aligned}\tag{15c}$$

$$a_n\big(T_{3n}^{(1)}(b,\omega)-inE^sT_{5n}^{(1)}(b,\omega)/b\big)+b_n\big(T_{3n}^{(2)}(b,\omega)-inE^sT_{5n}^{(2)}(b,\omega)/b\big)$$
$$+c_n\big(T_{4n}^{(1)}(b,\omega)-inE^sT_{6n}^{(1)}(b,\omega)/b\big)+d_n\big(T_{4n}^{(2)}(b,\omega)-inE^sT_{6n}^{(2)}(b,\omega)/b\big)=0. \quad (15d)$$

This system can be cast in the form

$$\boldsymbol{T}_n\boldsymbol{d}_n=\boldsymbol{0}, \quad (16)$$

in which $\boldsymbol{d}_n=[a_n,b_n,c_n,d_n]^T$ $(n=0,1,2,\dots)$ is the modal vector multiplied by (4×4) square matrix $\boldsymbol{T}_n$, containing frequency-dependent coefficients. Setting the determinant of $\boldsymbol{T}_n$ equal to zero, the characteristic equation of the system is obtained which leads to determination of the natural frequencies. It should be noted that for each frequency number, n, there are infinite numbers of longitudinal modes, denoted by m. A Mathematica program was written for numerical calculation of the natural frequencies as a function of the NT inner and outer radii through a simple root finding technique based on the bisection approach.

3. Numerical examples

To illustrate the influence of the surface stress on the dynamic behavior of the nanotube, some numerical examples are provided in this section. To this end, a NT with an infinite length and of selected outer to inner radius ratio is considered to be made of isotropic aluminum with the following physical properties: $\rho=2700\,\mathrm{kg/m^3}$, $\lambda=52.0\times10^9\,\mathrm{N/m^2}$, and $\mu=34.7\times10^9\,\mathrm{N/m^2}$. Two different sets of surface properties corresponding to the crystallographic directions [100] (denoted as surface A (SA)) and [111] (denoted as surface B (SB)) in aluminum are used in the calculation. The corresponding elastic constants are [Hasheminejad and Avazmohammadi 2009] $E^s=-8.95\,\mathrm{N/m}$ for SA and $E^s=6.08\,\mathrm{N/m}$ for SB. Surface C (SC) (with $E^s=0\,\mathrm{N/m}$) refers to a surface with the classical perfect bonding condition. Furthermore, as mentioned before, we assume $\tau_0=0$. In the following examples, the natural frequencies have been normalized by c_p/b.

Figure 2 displays the variation of the normalized natural frequency versus the inner radius of the NT, for the first longitudinal mode $(m=1)$ and for two selected outer to inner radius ratios $(b/a=1.1,1.5)$. These figures include the results associated with the first two frequencies numbers $(n=0,1)$ for three different surface types, SA, SB, and SC. Some observations are in order. It can be seen that the surface effect is more evident for lower values of the outer to inner radius ratio, corresponding to thinner NTs. Also, the frequency values for SA and SB are, respectively, lower and higher than that of the classical SC. This drop (rise) for SA (SB) is connected to the negative (positive) sign of the associated constant E^s. Moreover, since the absolute value of E^s for SA is greater than that of SB, its discrepancy with the classic solution (SC) is larger. Furthermore, as expected, by increasing the inner radius of NT (specifically, for $a>15\,\mathrm{nm}$), the surface effect gradually diminishes and the normalized frequencies (associated with SA and SB) approach the classical (size-independent) limit (we used [Gazis 1958, Equation (17)] to obtain the classical solution).

Figure 3 displays the variation of the normalized natural frequency, for three types of surfaces, SA, SB, and SC, versus the frequency number $(1\le n\le8)$ for a NT with $b/a=3$. The results are calculated for the first three longitudinal modes (that is, $1\le m\le3$) at each frequency number, n. It is found that the surface effects become more evident as the frequency number, n, increases. Similarly, a larger surface effect is observed at higher longitudinal mode numbers. This may be linked to the fact that the deformed

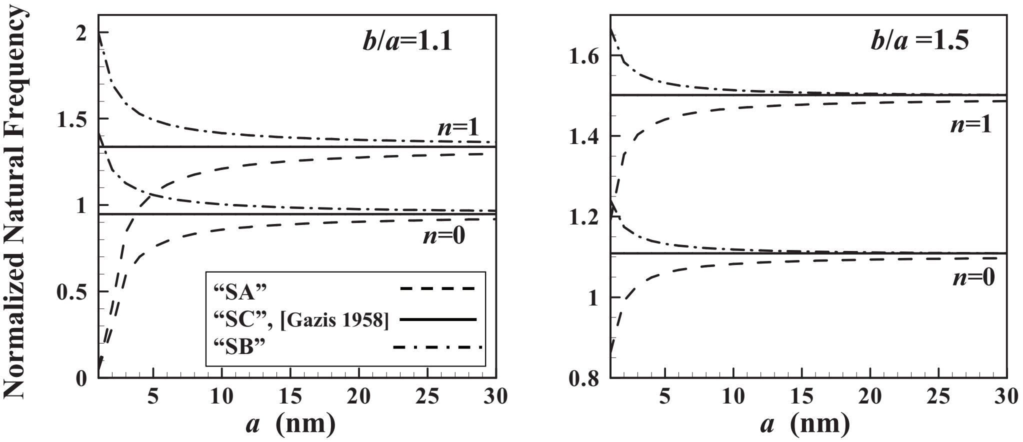

Figure 2. Variation of the normalized natural frequency with NT size, for selected radius ratio, surface type, longitudinal mode ($m = 1$), and frequency number ($n = 0, 1$).

shape of the inner/outer surfaces of the NT at higher modes of vibration has more curvature associated with a larger hoop strain at the surfaces. Hence, based on (12), a stronger surface effect at these modes is anticipated. Also, the fundamental frequency number ($n = 2$) that has the minimum value among all frequencies remains unchanged despite the presence of the surface effect.

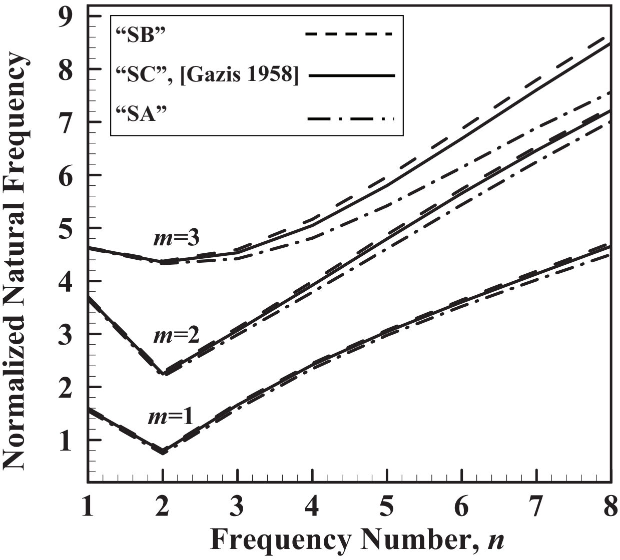

Figure 3. Variation of the normalized natural frequency with frequency number (n), for selected surface types and longitudinal modes ($m = 1, 2, 3$).

4. Conclusions

Making use of the Helmholtz wave equations together with the theory of surface elasticity, the influence of surface stress was investigated on the natural frequencies of a long, nanoscaled, cylindrical tube with a circular cross-section. As a numerical example, the free vibration of a nanotube (NT) made of aluminum with two different types of surface constants was studied. In this example, the size-dependence of the natural frequencies of the NT was analyzed for various natural frequency numbers and longitudinal modes. It was found that the size dependence is more noticeable at higher modes of vibration. This observation could be considerable technological interest in the area of designing nanoscaled devices.

References

[Abbasion et al. 2009] S. Abbasion, A. Rafsanjani, R. Avazmohammadi, and A. Farshidianfar, "Free vibration of microscaled Timoshenko beams", *Appl. Phys. Lett.* **95**:14 (2009), 143122.

[Benveniste and Miloh 2001] Y. Benveniste and T. Miloh, "Imperfect soft and stiff interfaces in two-dimensional elasticity", *Mech. Mater.* **33**:6 (2001), 309–323.

[Chen et al. 2006] C. Q. Chen, Y. Shi, Y. S. Zhang, J. Zhu, and Y. J. Yan, "Size dependence of Young's modulus in ZnO nanowires", *Phys. Rev. Lett.* **96**:7 (2006), 75505.

[Cuenot et al. 2004] S. Cuenot, C. Frétigny, S. Demoustier-Champagne, and B. Nysten, "Surface tension effect on the mechanical properties of nanomaterials measured by atomic force microscopy", *Phys. Rev. B* **69**:16 (2004), 165410.

[Gazis 1958] D. C. Gazis, "Exact analysis of the plane-strain vibrations of thick-walled hollow cylinders", *J. Acoust. Soc. Am.* **30**:8 (1958), 786–794.

[Gurtin and Murdoch 1975] M. E. Gurtin and A. I. Murdoch, "A continuum theory of elastic material surfaces", *Arch. Ration. Mech. Anal.* **57**:4 (1975), 291–323.

[Gurtin et al. 1998] M. E. Gurtin, J. Weissmüller, and F. Larché, "A general theory of curved deformable interfaces in solids at equilibrium", *Philos. Mag. A* **78**:5 (1998), 1093–1109.

[Hasheminejad and Avazmohammadi 2009] S. M. Hasheminejad and R. Avazmohammadi, "Size-dependent effective dynamic properties of unidirectional nanocomposites with interface energy effects", *Compos. Sci. Technol.* **69**:15–16 (2009), 2538–2546.

[Hasheminejad and Gheshlaghi 2010] S. M. Hasheminejad and B. Gheshlaghi, "Dissipative surface stress effects on free vibrations of nanowires", *Appl. Phys. Lett.* **97**:25 (2010), 253103.

[Hasheminejad and Mirzaei 2009] S. M. Hasheminejad and Y. Mirzaei, "Free vibration analysis of an eccentric hollow cylinder using exact 3D elasticity theory", *J. Sound Vib.* **326**:3–5 (2009), 687–702.

[He and Lilley 2008] J. He and C. M. Lilley, "Surface stress effect on bending resonance of nanowires with different boundary conditions", *Appl. Phys. Lett.* **93**:26 (2008), 263108.

[Jing et al. 2006] G. Y. Jing, H. L. Duan, X. M. Sun, Z. S. Zhang, J. Xu, Y. D. Li, J. X. Wang, and D. P. Yu, "Surface effects on elastic properties of silver nanowires: contact atomic-force microscopy", *Phys. Rev. B* **73**:23 (2006), 235409.

[Miller and Shenoy 2000] R. E. Miller and V. B. Shenoy, "Size-dependent elastic properties of nanosized structural elements", *Nanotechnology* **11**:3 (2000), 139–147.

[Pao and Mow 1973] Y. H. Pao and C. C. Mow, *Diffraction of elastic waves and dynamics stress concentration*, Crane Russak, New York, 1973.

[Shenoy 2002] V. B. Shenoy, "Size-dependent rigidities of nanosized torsional elements", *Int. J. Solids Struct.* **39**:15 (2002), 4039–4052.

[Shenoy 2005] V. B. Shenoy, "Atomistic calculations of elastic properties of metallic fcc crystal surfaces", *Phys. Rev. B* **71**:9 (2005), 094104.

[Tan and Lim 2006] E. P. S. Tan and C. T. Lim, "Mechanical characterization of nanofibers: a review", *Compos. Sci. Technol.* **66**:9 (2006), 1102–1111.

[Wang 2007] G. F. Wang, "Diffraction of plane compressional wave by a nanosized spherical cavity with surface effects", *Appl. Phys. Lett.* **90**:21 (2007), 211907.

[Wang et al. 2006] G. F. Wang, T. J. Wang, and X. Q. Feng, "Surface effects on the diffraction of plane compressional waves by a nanosized circular hole", *Appl. Phys. Lett.* **89**:23 (2006), 231923.

[Wong et al. 1997] E. W. Wong, P. E. Sheehan, and C. M. Lieber, "Nanobeam mechanics: elasticity, strength, and toughness of nanorods and nanotubes", *Science* **277**:5334 (1997), 1971–1975.

[Zhou and Huang 2004] L. G. Zhou and H. Huang, "Are surfaces elastically softer or stiffer?", *Appl. Phys. Lett.* **84**:11 (2004), 1940–1942.

Received 28 Mar 2011. Revised 8 Aug 2011. Accepted 19 Aug 2011.

JAFAR ESKANDARI JAM: `jejam@mail.com`
Composite Material and Technology Center, Tehran, Iran

YASER MIRZAEI: `mirzaei@damavandiau.ac.ir`
Department of Mechanical Engineering, Damavand Branch, Islamic Azad University, Damavand, Iran

BEHNAM GHESHLAGHI: `behnamqeshlaqi@gmail.com`
Young Researchers Club, Science and Research Branch, Islamic Azad University, Tehran, Iran

REZA AVAZMOHAMMADI: `reza.avazmohammadi@gmail.com`
Department of Mechanical Engineering and Applied Mechanics, University of Pennsylvania, 220 S 33rd St., Philadelphia, PA 19104-6315, United States

JOURNAL OF MECHANICS OF MATERIALS AND STRUCTURES
Vol. 7, No. 2, 2012

SPECTRAL ELEMENT MODEL FOR THE VIBRATION OF A SPINNING TIMOSHENKO SHAFT

USIK LEE AND INJOON JANG

A spectral element model for a spinning uniform shaft is developed. The spinning shaft supported by bearings is represented by the uniform Timoshenko beam model and the bearing-supports are represented by equivalent springs. The variational approach is used to formulate the spectral element model by using the frequency-dependent shape functions derived from exact wave solutions on the frequency-domain governing differential equations. The conventional finite element model is also formulated for evaluating the accuracy of the present spectral element model through some example problems.

1. Introduction

Spinning shafts have been extensively used in diverse engineering applications such as motors, engines, turbines, and machine tools. In general, the rotating machines consist of multiple spinning shafts and disks (or blades) which are connected to each other to form rotor systems supported by multiple bearings. As it is very important to predict the dynamic characteristics of the rotor systems accurately in the early design phase, there have been extensive studies on the modeling and analysis of such rotor systems in past decades [Nelson 2003].

In previous studies, the dynamics of spinning shafts were represented by various models. When the diameter of a shaft is large relative to its length and when vibration occurs at high frequencies, deflections due to transverse shear and rotary inertia become important. Thus, many researchers have used the Timoshenko beam models for spinning shafts [Eshleman and Eubanks 1969; Nelson 1980; Ehrich 1992; Zu and Han 1992; Ghoneim and Lawrie 2007; Chen 2010]. In this study, we adopt the Timoshenko beam model used by [Ehrich 1992; Zu and Han 1992].

The early methods used to determine the critical speed of a rotor are Rayleigh's method, Dunkerley's formula, Holzer's method, and the transfer matrix method [Lund 1974]. As the size of the transfer matrix generated to represent a rotor system is not large, the transfer matrix method is very efficient for the analysis of one-dimensional (1D) systems such as rotor systems. However, as the transfer matrix method provides dynamic responses only at the endpoints of a 1D system, postprocessing is necessary to compute the dynamic responses at the interim positions of the system. [Ruhl and Booker 1972] and [Nelson 1980] used FEM to investigate the stability and dynamics of rotor systems. In general, a large number of degrees of freedom (DOFs) are required for an FEM model of a large flexible rotor system, which may result in an increase in the computational cost as well as a widely spread frequency spectrum

---

This research was supported in part by the Basic Science Research Program through the National Research Foundation of Korea funded by the Ministry of Education, Science and Technology (2010-0007741) and in part by an Inha University research grant.
Keywords: spinning Timoshenko shaft, spectral element model, finite element model, natural frequency, critical speed, dispersion curve.

which may include many insignificant vibration modes. To cope with these problems, reduced-order modeling techniques have been introduced [Kane and Torby 1991]. Though reduced-order modeling techniques are useful for reducing the size of FEM models, they are known to degrade the accuracy of FEM solutions.

Thus, as an alternative analysis method, this paper adopts the spectral element method (SEM) for the dynamic analysis of the flexible spinning shafts of a rotor system. SEM may meet two requirements: high accuracy up to the frequency range of interest and the use of a minimum number of DOFs [Doyle 1997; Lee et al. 2000; Vinod et al. 2007; Lee 2009]. Thus, SEM has apparent advantages over the other solution methods such as the transfer matrix method and FEM, especially when it is applied to 1D structural dynamic problems such as rotor systems as well as to structural health monitoring problems. However, though SEM can be also used for nonlinear analysis by using an iterative approach [Lee 2009], conventional FEM can be more efficiently used for nonlinear analysis.

Thus, the purposes of this paper are:

- to develop a spectral element model for the spinning Timoshenko shaft (T-shaft) and
- to apply the spectral element model to investigate the natural frequencies and critical speeds of example spinning shafts.

The results obtained by using the spectral element model are then compared with the results obtained by using the conventional finite element model and the analytical theories available in the literature to verify the accuracy of the spectral element model.

2. Governing equations

Consider a spinning flexible uniform shaft subjected to transverse vibrations and represent it as a spinning uniform T-shaft. The equations of motion and relevant boundary conditions for the spinning uniform T-shaft can be derived by using Hamilton's principle [Meirovitch 1980]:

$$\int_{t_1}^{t_2} (\delta T - \delta U + \delta W)\, dt = 0, \tag{1}$$

where T is the kinetic energy, U is the potential energy, and δW is the virtual work done by external forces and moments. As shown in Figure 1, the uniform T-shaft of circular cross-section is spinning about the central axis x at a constant speed of Ω radians/s and it has length L, bending rigidity EI, transverse shear rigidity κGA, mass per length ρA, mass moment of inertia about the y or z-axes ρI, and polar mass moment of inertia about the x-axis ρJ. In Figure 1a, $v(x,t)$ is the transverse displacement in the y-direction, $w(x,t)$ is the transverse displacement in the z-direction, $\phi(x,t)$ is the rotation angle about the y-axis, and $\psi(x,t)$ is the rotation angle about the z-axis.

Assuming that the uniform T-shaft takes small amplitude transverse vibrations in the y and z-directions, the kinetic and potential energies can be obtained as [Nelson 1980; Ehrich 1992]

$$T = \frac{1}{2}\int_0^L \rho A(\dot{v}^2 + \dot{w}^2)\, dx + \frac{1}{2}\int_0^L \rho I(\dot{\phi}^2 + \dot{\psi}^2)\, dx + \frac{1}{2}\int_0^L \rho J(\Omega - \phi\dot{\psi})^2\, dx, \tag{2}$$

$$U = \frac{1}{2}\int_0^L EI(\phi'^2 + \psi'^2)\, dx + \frac{1}{2}\int_0^L \kappa GA[(v' - \psi)^2 + (w' + \phi)^2]\, dx + \sum_{i=1}^{2} \frac{1}{2}\boldsymbol{v}_i^T \boldsymbol{K}_{\text{support}(i)} \boldsymbol{v}_i, \tag{3}$$

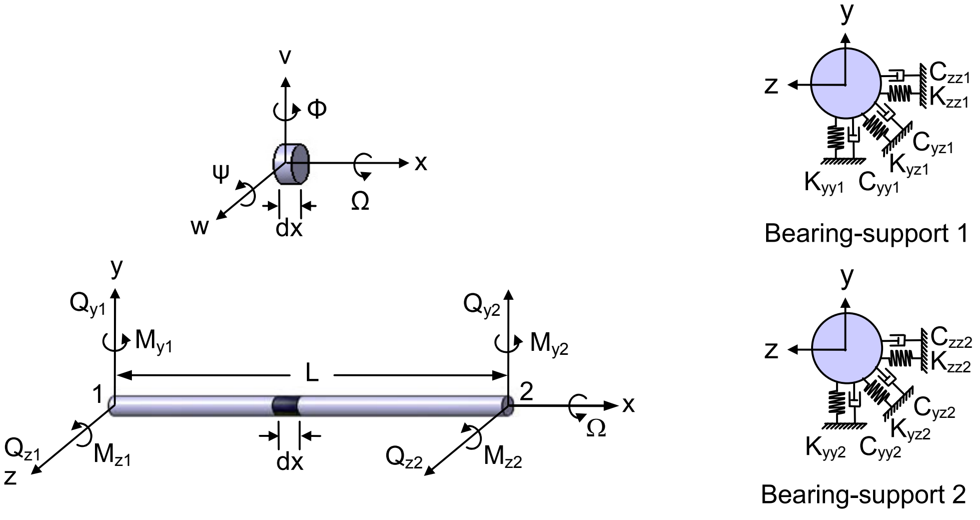

(a) (b)

Figure 1. A spinning uniform shaft: (a) displacement fields and the boundary forces and moments and (b) bearing-supports.

where

$$\boldsymbol{v}_i = \begin{Bmatrix} v_i \\ w_i \end{Bmatrix}, \qquad \boldsymbol{K}_{\text{support}(i)} = \begin{bmatrix} K_{yyi} & K_{yzi} \\ K_{zyi} & K_{zzi} \end{bmatrix} \quad (i = 1, 2). \tag{4}$$

The matrices $\boldsymbol{K}_{\text{support}(1)}$ and $\boldsymbol{K}_{\text{support}(2)}$ represent the stiffnesses of bearing-supports 1 and 2, as shown in Figure 1b, and the vectors $\boldsymbol{v}_1$ and $\boldsymbol{v}_2$ represent the transverse displacements at bearing-supports 1 and 2. The dot ($\dot{}$) and prime ($'$) denote the derivatives with respect to the time t and axial coordinate x, respectively. In (2), the first integral represents the translational kinetic energy and the other two integrals the rotational kinetic energies. In (3), the first integral represents the strain energy for the transverse bending deformations, the second integral for the transverse shear deformations, and the last term for the bearing-support deformations. The virtual work δW is given by

$$\begin{aligned} \delta W = \int_0^L (p_y \delta v + p_z \delta w + \tau_y \delta \phi + \tau_z \delta \psi)\, dx + Q_{y1} \delta v_1 + Q_{y2} \delta v_2 + Q_{z1} \delta w_1 + Q_{z2} \delta w_2 \\ + M_{y1} \delta \phi_1 + M_{y2} \delta \phi_2 + M_{z1} \delta \psi_1 + M_{z2} \delta \psi_2 - f_{\dot{v}_1} \delta v_1 - f_{\dot{w}_1} \delta w_1 - f_{\dot{v}_2} \delta v_2 - f_{\dot{w}_2} \delta w_2, \end{aligned} \tag{5}$$

where Q_{yi}, Q_{zi}, M_{yi}, and M_{zi} $(i = 1, 2)$ are the transverse shear forces and bending moments applied at the two ends of the T-shaft as shown in Figure 1a. The forces and bending moments distributed along the x-axis are p_y, p_z, τ_y, and τ_z. The viscous damping forces generated by bearing-supports 1 and 2 are $f_{\dot{v}_i}$ and $f_{\dot{w}_i}$ $(i = 1, 2)$, and they can be computed from

$$f_{\dot{v}_i} = \frac{\partial R}{\partial \dot{v}_i}, \qquad f_{\dot{w}_i} = \frac{\partial R}{\partial \dot{w}_i} \quad (i = 1, 2). \tag{6}$$

The Rayleigh's dissipation function R is given by

$$R=\sum_{i=1}^{2}\frac{1}{2}\dot{\boldsymbol{v}}_i^T\boldsymbol{C}_{\text{support}(i)}\dot{\boldsymbol{v}}_i,\tag{7}$$

where

$$\boldsymbol{C}_{\text{support}(i)}=\begin{bmatrix}C_{yyi} & C_{yzi}\\ C_{zyi} & C_{zzi}\end{bmatrix}\quad(i=1,2),\tag{8}$$

where $C_{abi}(a,b=y,z)$ are viscous damping coefficients of the bearing-supports as shown in Figure 1b.

Substituting (2), (3), and (6) into (1) and then applying the integral by parts, we can obtain the differential equations of motion as

$$\begin{aligned}&\rho A\ddot{v}-\kappa GA(v''-\psi')=p_y, &&\rho I\ddot{\psi}-\rho J\Omega\dot{\phi}-EI\psi''-\kappa GA(v'-\psi)+\rho J(2\phi\dot{\phi}\dot{\psi}+\phi^2\ddot{\psi})=\tau_z,\\ &\rho A\ddot{w}-\kappa GA(w''+\phi')=p_z, &&\rho I\ddot{\phi}+\rho J\Omega\dot{\psi}-EI\phi''+\kappa GA(w'+\phi)-\rho J\phi\dot{\psi}^2=\tau_y,\end{aligned}\tag{9}$$

and the natural boundary conditions as

$$\begin{aligned}Q_y(0,t)&=K_{yy1}v_1+\tfrac{1}{2}(K_{yz1}+K_{zy1})w_1+C_{yy1}\dot{v}_1+\tfrac{1}{2}(C_{yz1}+C_{zy1})\dot{w}_1-Q_{y1},\\ Q_y(L,t)&=-K_{yy2}v_2-\tfrac{1}{2}(K_{yz2}+K_{zy2})w_2-C_{yy2}\dot{v}_2-\tfrac{1}{2}(C_{yz2}+C_{zy2})\dot{w}_2+Q_{y2},\\ Q_z(0,t)&=K_{zz1}w_1+\tfrac{1}{2}(K_{yz1}+K_{zy1})v_1+C_{zz1}\dot{w}_1+\tfrac{1}{2}(C_{yz1}+C_{zy1})\dot{v}_1-Q_{z1},\\ Q_z(L,t)&=-K_{zz2}w_2-\tfrac{1}{2}(K_{yz2}+K_{zy2})v_2-C_{zz2}\dot{w}_2-\tfrac{1}{2}(C_{yz2}+C_{zy2})\dot{v}_2+Q_{z2},\\ M_y(0,t)&=-M_{y1},\qquad M_y(L,t)=M_{y2},\\ M_z(0,t)&=-M_{z1},\qquad M_z(L,t)=M_{z2}.\end{aligned}\tag{10}$$

The force-displacement relations are defined by

$$\begin{aligned}Q_y(x,t)&=\kappa GA(v'-\psi), &\quad M_y(x,t)&=EI\phi',\\ Q_z(x,t)&=\kappa GA(w'+\phi), &\quad M_z(x,t)&=EI\psi'.\end{aligned}\tag{11}$$

By neglecting small nonlinear terms from (9), we can obtain

$$\begin{aligned}&\rho A\ddot{v}-\kappa GA(v''-\psi')=p_y, &&\rho I\ddot{\psi}-\rho J\Omega\dot{\phi}-EI\psi''-\kappa GA(v'-\psi)=\tau_z,\\ &\rho A\ddot{w}-\kappa GA(w''+\phi')=p_z, &&\rho I\ddot{\phi}+\rho J\Omega\dot{\psi}-EI\phi''+\kappa GA(w'+\phi)=\tau_y.\end{aligned}\tag{12}$$

Equations (12) are identical to the governing equations introduced in [Ehrich 1992; Zu and Han 1992]. Equations (12) will be used herein for developing a spectral element model for spinning T-shafts.

3. Spectral element modeling

The spectral element model for the spinning uniform T-shaft is derived from the differential equations of motion given by (12). To formulate the spectral element, we represent the solutions of (12), the external forces, and the resultant forces and moments in spectral forms as [Lee 2009]

$$\{v(x,t)\ \ w(x,t)\ \ \psi(x,t)\ \ \phi(x,t)\}=\frac{1}{N}\sum_{n=0}^{N-1}\{V_n(x;\omega_n)\ \ W_n(x;\omega_n)\ \ \psi_n(x;\omega_n)\ \ \phi_n(x;\omega_n)\}\,e^{i\omega_n t},\tag{13}$$

$$\left\{p_y(x,t)\;\; p_z(x,t)\;\; \tau_y(x,t)\;\; \tau_z(x,t)\right\} = \frac{1}{N}\sum_{n=0}^{N-1}\left\{P_{yn}(x;\omega_n)\;\; P_{zn}(x;\omega_n)\;\; T_{yn}(x;\omega_n)\;\; T_{zn}(x;\omega_n)\right\} e^{i\omega_n t}, \tag{14}$$

$$\begin{aligned}&\left\{Q_y(x,t)\;\; Q_z(x,t)\;\; M_y(x,t)\;\; M_z(x,t)\right\}\\ &\qquad = \frac{1}{N}\sum_{n=0}^{N-1}\left\{Q_{yn}(x;\omega_n)\;\; Q_{zn}(x;\omega_n)\;\; M_{yn}(x;\omega_n)\;\; M_{zn}(x;\omega_n)\right\} e^{i\omega_n t}.\end{aligned} \tag{15}$$

Substituting (13) and (14) into (12) gives

$$\begin{aligned}&\kappa GA(V''-\psi')+\rho A\omega^2 V+P_y=0, && EI\psi''+i\omega\Omega\rho J\Phi+\kappa GA(V'-\psi)+\rho I\omega^2\psi+T_z=0,\\ &\kappa GA(W''+\Phi')+\rho A\omega^2 W+P_z=0, && EI\Phi''-i\omega\Omega\rho J\psi-\kappa GA(W'+\Phi)+\rho I\omega^2\Phi+T_y=0,\end{aligned} \tag{16}$$

where the subscripts n are omitted for brevity. Similarly, substituting (13) and (15) into (11) gives

$$\begin{aligned}&Q_y(x)=\kappa GA(V'-\psi), && M_y(x)=EI\Phi',\\ &Q_z(x)=\kappa GA(W'+\Phi), && M_z(x)=EI\psi'.\end{aligned} \tag{17}$$

Consider the homogeneous equations reduced from (16) as

$$\begin{aligned}&\kappa GA(V''-\psi')+\rho A\omega^2 V=0, && EI\psi''+i\omega\Omega\rho J\Phi+\kappa GA(V'-\psi)+\rho I\omega^2\psi=0,\\ &\kappa GA(W''+\Phi')+\rho A\omega^2 W=0, && EI\phi''-i\omega\Omega\rho J\psi-\kappa GA(W'+\Phi)+\rho I\omega^2\Phi=0.\end{aligned} \tag{18}$$

Assume the homogeneous solutions of (18) as

$$V(x)=ae^{-ikx},\qquad W(x)=tae^{-ikx},\qquad \psi(x)=rae^{-ikx},\qquad \Phi(x)=t\hat{r}ae^{-ikx}. \tag{19}$$

Substitution of (19) into (18) yields an eigenvalue problem as

$$\begin{bmatrix}\sigma_1 & -\sigma_3 & 0 & 0\\ \sigma_3 & \sigma_2 & 0 & -\sigma_4\\ 0 & 0 & \sigma_1 & \sigma_3\\ 0 & \sigma_4 & -\sigma_3 & \sigma_2\end{bmatrix}\begin{Bmatrix}1\\ r\\ t\\ t\hat{r}\end{Bmatrix}=\begin{Bmatrix}0\\0\\0\\0\end{Bmatrix}, \tag{20}$$

where

$$\sigma_1=k^2\kappa GA-\omega^2\rho A,\qquad \sigma_2=k^2EI+\kappa GA-\omega^2\rho I,\qquad \sigma_3=ik\kappa GA,\qquad \sigma_4=i\omega\Omega\rho J. \tag{21}$$

From (20), we can get a dispersion equation as

$$\begin{aligned}&k^8-2(\eta_1k_F^4+k_G^4)k^6+(\eta_1^2k_F^8+4\eta_1k_G^4k_F^4+k_G^8-2k_F^4-\eta_2^{-2}\eta_3^2\Omega^2\omega^2)k^4\\ &\qquad+(-2\eta_1^2k_G^4k_F^8-2\eta_1k_G^8k_F^4+2\eta_1k_F^8+2k_F^4k_G^4+2k_F^4\eta_2^{-1}\eta_3^2\Omega^2\omega^2)k^2\\ &\qquad\qquad+\eta_1^2k_G^8k_F^8-2\eta_1k_G^4k_F^8+(1-\eta_3^2\Omega^2\omega^2)k_F^8=0,\end{aligned} \tag{22}$$

where

$$k_F=\sqrt{\omega}\left(\frac{\rho A}{EI}\right)^{1/4},\qquad k_G=\sqrt{\omega}\left(\frac{\rho A}{\kappa GA}\right)^{1/4},\qquad \eta_1=\frac{\rho I}{\rho A},\qquad \eta_2=\frac{EI}{\kappa GA},\qquad \eta_3=\frac{\rho J}{\kappa GA}. \tag{23}$$

Eight wavenumbers k_i $(i = 1, 2, \ldots, 8)$ can be computed from (22). By substituting each wavenumber into (20), we can obtain

$$\begin{aligned} r_j &= i k_j^{-1}(k_G^4 - k_j^2), \quad \hat{r}_j = -r_j, \\ t_j &= -(i\eta_3\Omega\omega)^{-1} r_j^{-1}[ik_j + (\eta_2 k_j^2 - \eta_1 k_G^4) r_j] \end{aligned} \qquad (j = 1, 2, \ldots, 8). \tag{24}$$

By using the eight wavenumbers computed from (22), the homogeneous solutions of (18) can be obtained as

$$V(x) = \boldsymbol{N}_v(x;\omega)\boldsymbol{d}, \quad W(x) = \boldsymbol{N}_w(x;\omega)\boldsymbol{d}, \quad \psi(x) = \boldsymbol{N}_\psi(x;\omega)\boldsymbol{d}, \quad \Phi(x) = \boldsymbol{N}_\phi(x;\omega)\boldsymbol{d}. \tag{25}$$

where

$$\boldsymbol{d} = \begin{Bmatrix} V_1 & \psi_1 & W_1 & \Phi_1 & V_2 & \psi_2 & W_2 & \Phi_2 \end{Bmatrix}^T \equiv \begin{Bmatrix} V(0) & \psi(0) & W(0) & \Phi(0) & V(L) & \psi(L) & W(L) & \Phi(L) \end{Bmatrix}^T \tag{26}$$

and

$$\begin{aligned} \boldsymbol{N}_v(x;\omega) &= \boldsymbol{e}_v(x)\boldsymbol{H}_B^{-1}, \quad \boldsymbol{N}_w(x;\omega) = \boldsymbol{e}_w(x)\boldsymbol{H}_B^{-1}, \\ \boldsymbol{N}_\psi(x;\omega) &= \boldsymbol{e}_\psi(x)\boldsymbol{H}_B^{-1}, \quad \boldsymbol{N}_\phi(x;\omega) = \boldsymbol{e}_\phi(x)\boldsymbol{H}_B^{-1}, \end{aligned} \tag{27}$$

with the use of the following definitions:

$$\begin{aligned} \boldsymbol{e}_v(x) &= \begin{bmatrix} e^{-ik_1x} & e^{ik_1x} & e^{-ik_3x} & e^{ik_3x} & e^{-ik_5x} & e^{ik_5x} & e^{-ik_7x} & e^{ik_7x} \end{bmatrix}, \\ \boldsymbol{e}_\psi(x) &= \boldsymbol{e}_v(x)\boldsymbol{R}, \quad \boldsymbol{e}_w(x) = \boldsymbol{e}_v(x)\boldsymbol{T}, \quad \boldsymbol{e}_\phi(x) = -\boldsymbol{e}_v(x)\boldsymbol{T}\boldsymbol{R}, \\ \boldsymbol{H}_B &= \begin{bmatrix} \boldsymbol{e}_v^T(0) & \boldsymbol{e}_\psi^T(0) & \boldsymbol{e}_w^T(0) & \boldsymbol{e}_\phi^T(0) & \boldsymbol{e}_v^T(L) & \boldsymbol{e}_\psi^T(L) & \boldsymbol{e}_w^T(L) & \boldsymbol{e}_\phi^T(L) \end{bmatrix}^T, \end{aligned} \tag{28}$$

where

$$\boldsymbol{R} = \mathrm{diag}[r_j], \quad \boldsymbol{T} = \mathrm{diag}[t_j] \qquad (j = 1, 2, \ldots, 8). \tag{29}$$

$\boldsymbol{N}_v$, $\boldsymbol{N}_\psi$, $\boldsymbol{N}_w$, and $\boldsymbol{N}_\phi$ are the frequency-dependent dynamic shape function matrices and $\boldsymbol{d}$ is the spectral nodal DOFs vector for the transverse bending vibrations of the spinning shaft.

To formulate the spectral element equation, the weak form of (16) are obtained in the form

$$\begin{aligned} &\int_0^L [EI(\Phi'\delta\Phi' + \psi'\delta\psi') + \kappa GA(V'\delta V' + W'\delta W') - \kappa GA(\psi\delta V' + V'\delta\psi) \\ &\qquad\qquad + \kappa GA(\Phi\delta W' + W'\delta\Phi) + \kappa GA(\Phi\delta\Phi + \psi\delta\psi)]\,dx \\ &\quad + \int_0^L i\omega\Omega\rho J(\psi\delta\Phi - \Phi\delta\psi)\,dx - \int_0^L \omega^2[\rho A(V\delta V + W\delta W) + \rho I(\Phi\delta\Phi + \psi\delta\psi)]\,dx \\ &\quad = \int_0^L (P_y\delta V + T_z\delta\psi + P_z\delta W + T_y\delta\phi)\,dx + Q_y\delta V\big|_0^L + M_z\delta\psi\big|_0^L + Q_z\delta W\big|_0^L + M_y\delta\Phi\big|_0^L. \end{aligned} \tag{30}$$

Substituting (25) into (30) and applying the associated boundary conditions, we can get

$$\boldsymbol{S}(\omega)\boldsymbol{d} = \boldsymbol{f}_c + \boldsymbol{f}_d, \tag{31}$$

where $\boldsymbol{S}(\omega)$ is the spectral element matrix given by

$$\boldsymbol{S}(\omega) = \boldsymbol{H}^{-T}\boldsymbol{D}\boldsymbol{H}^{-1} + \boldsymbol{K}_{\text{support}} + i\omega\boldsymbol{C}_{\text{support}}, \tag{32}$$

where

$$\begin{aligned}\boldsymbol{D}(\omega) = {} & -EI(\boldsymbol{RTKEKTR} + \boldsymbol{RKEKR}) - \kappa GA(\boldsymbol{KEK} + \boldsymbol{TKEKT}) + i\kappa GA(\boldsymbol{KER} + \boldsymbol{REK}) \\ & + i\kappa GA(\boldsymbol{TKETR} + \boldsymbol{RTEKT}) + \kappa GA(\boldsymbol{RTETR} + \boldsymbol{RER}) - \omega^2 \rho A(\boldsymbol{E} + \boldsymbol{TET}) \\ & - \omega^2 \rho I(\boldsymbol{RTETR} + \boldsymbol{RER}) - i\omega\Omega\rho J(\boldsymbol{RTER} - \boldsymbol{RETR}), \end{aligned} \tag{33}$$

$$\boldsymbol{K}_{\text{support}} = \begin{bmatrix} \boldsymbol{K}_1 & \boldsymbol{0} \\ \boldsymbol{0} & \boldsymbol{K}_2 \end{bmatrix}, \quad \boldsymbol{C}_{\text{support}} = \begin{bmatrix} \boldsymbol{C}_1 & \boldsymbol{0} \\ \boldsymbol{0} & \boldsymbol{C}_2 \end{bmatrix}, \tag{34}$$

with the use of following definitions:

$$\boldsymbol{E}(\omega) = \int_0^L \boldsymbol{e}_v^T \boldsymbol{e}_v \, dx \equiv [E_{lm}] = \begin{cases} \dfrac{i}{k_l + k_m}[e^{-i(k_l+k_m)L} - 1] & \text{if } k_l + k_m \neq 0, \\ L & \text{if } k_l + k_m = 0, \end{cases} \tag{35}$$

$$\boldsymbol{K} = \operatorname{diag}[k_j] \qquad (j = 1, 2, \ldots, 8), \tag{36}$$

$$\boldsymbol{K}_i = \begin{bmatrix} K_{yyi} & 0 & \frac{1}{2}(K_{yzi} + K_{zyi}) & 0 \\ 0 & 0 & 0 & 0 \\ \frac{1}{2}(K_{yzi} + K_{zyi}) & 0 & K_{zzi} & 0 \\ 0 & 0 & 0 & 0 \end{bmatrix} \quad (i = 1, 2), \tag{37}$$

$$\boldsymbol{C}_i = \begin{bmatrix} C_{yyi} & 0 & \frac{1}{2}(C_{yzi} + C_{zyi}) & 0 \\ 0 & 0 & 0 & 0 \\ \frac{1}{2}(C_{yzi} + C_{zyi}) & 0 & C_{zzi} & 0 \\ 0 & 0 & 0 & 0 \end{bmatrix} \quad (i = 1, 2). \tag{38}$$

In (31), $\boldsymbol{f}_c$ represents the spectral nodal forces and moments due to the concentrated forces and moments, while $\boldsymbol{f}_d$ represents the ones due to the distributed forces and moments. They are defined by

$$\begin{aligned} \boldsymbol{f}_c &= \left\{ Q_{y1} \;\; M_{z1} \;\; Q_{z1} \;\; M_{y1} \;\; Q_{y2} \;\; M_{z2} \;\; Q_{z2} \;\; M_{y2} \right\}^T, \\ \boldsymbol{f}_d &= \int_0^L [P_y(x)\boldsymbol{N}_v^T(x) + T_z(x)\boldsymbol{N}_\psi^T(x) + P_z(x)\boldsymbol{N}_w^T(x) + T_y(x)\boldsymbol{N}_\phi^T(x)]\, dx \\ &= \left\{ F_{v1} \;\; F_{\psi 1} \;\; F_{w1} \;\; F_{\phi 1} \;\; F_{v2} \;\; F_{\psi 2} \;\; F_{w2} \;\; F_{\phi 2} \right\}^T. \end{aligned} \tag{39}$$

The last term of (33) is skew symmetric and represents the gyroscopic effect.

4. Spectral element analysis

The spectral element (31) can be assembled in an analogous way as in conventional FEM. After imposing the relevant boundary conditions, a global dynamic stiffness matrix equation can be obtained in the form

$$\boldsymbol{S}_g(\omega)\boldsymbol{d}_g = \boldsymbol{f}_{cg} + \boldsymbol{f}_{dg} = \boldsymbol{f}_g, \tag{40}$$

where the subscripts g denote the quantities for the assembled global spinning shaft system. As the spectral element matrix $\boldsymbol{S}(\omega)$ is formulated by using exact wave solutions to the frequency-domain governing differential equations, only one element will suffice for modeling a regular shaft of any length in the absence of any discontinuity or irregularity in the geometrical and material properties.

The natural frequencies ω_{NAT} of a global system can be computed from the condition that the determinant of the global dynamic stiffness matrix vanishes at ω_{NAT}. That is

$$\det \boldsymbol{S}_g(\omega_{\mathrm{NAT}}) = 0. \tag{41}$$

To compute the roots (that is, natural frequencies ω_{NAT}) of (41), we can use a proper root-searching algorithm in conjunction with the Wittrick–William algorithm [Wittrick and Williams 1971] not to miss any roots within a frequency range specified during the root search. The spectral nodal DOFs can be exactly computed from (40) as

$$\boldsymbol{d}_g = \boldsymbol{S}_g(\omega)^{-1}, \quad \boldsymbol{f}_g = \boldsymbol{T}_g(\omega)\boldsymbol{f}_g, \tag{42}$$

where $\boldsymbol{T}_g(\omega) = \boldsymbol{S}_g(\omega)^{-1}$ is the system transfer matrix (or frequency response function). Thus, (42) implies that the spectral nodal DOFs can be computed by convolving the system transfer matrix with the spectral nodal forces and moments. Once the spectral nodal DOFs are computed from (42), one can readily use the inverse FFT to compute the time history of the dynamic responses.

5. Numerical examples

5.1. ***Simply supported uniform shaft.*** Consider a simply supported uniform shaft as shown in Figure 2. The geometric and material properties of the uniform shaft are given as follows: length $2L = 2\,\mathrm{m}$, radius $r = 0.02\,\mathrm{m}$, mass density $\rho = 7700\,\mathrm{kg/m^3}$, Young's modulus $E = 207\,\mathrm{GPa}$, shear modulus 77.6 GPa, and shear correction factor for the circular cross-section $\kappa = 0.9$.

To verify the accuracy of the present spectral element model, the natural frequencies of the stationary (nonspinning) uniform shaft obtained by using the present spectral element model are compared in Table 1 with those obtained by using the finite element model (see the Appendix) as well as with those obtained by using the analytical formula given by [Blevins 1979] as

$$f_n = \bar{f}_n \alpha_n \sqrt{\beta_n - \sqrt{\beta_n^2 - \eta_1^{-1}\eta_2^{-1}}}\ \mathrm{Hz}, \tag{43}$$

where $\bar{f}_n$ are the natural frequencies of the simply supported, stationary uniform Bernoulli–Euler beam and

$$\alpha_n = \frac{L}{n\pi}, \quad \beta_n = \frac{1}{2}[\eta_1^{-1} + (1 + \alpha_n^2 \eta_1^{-1})\eta_2^{-1}]. \tag{44}$$

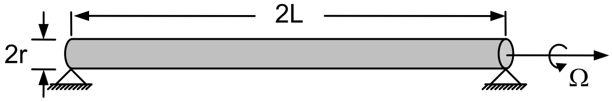

Figure 2. A simply supported uniform shaft, where Ω is the spinning speed.

	FEM (n)						
Mode	$n = 2$	$n = 10$	$n = 30$	$n = 50$	$n = 100$	SEM (1)	[Blevins 1979]
1st	20.43	20.35	20.35	20.35	20.35	20.35	20.35
2nd	90.35	81.23	81.29	81.29	81.29	81.29	81.29
3rd	226.9	182.6	182.5	182.5	182.5	182.5	182.5
4th	414.1	324.0	323.3	323.3	323.3	323.3	323.3
5th	-	505.8	503.1	503.0	502.9	502.9	502.9
10th	-	2232	1952	1947	1945	1945	1945
15th	-	5521	4228	4182	4166	4160	4160
20th	-	10261	7260	7058	6982	6956	6956

Table 1. Natural frequencies (in Hz) of the simply supported stationary uniform shaft ($\Omega = 0\,\text{rpm}$), with n the total number of finite elements used in the analysis.

For the spectral element analysis, the whole uniform shaft is represented by using a single element, that is, a one-element model. On the other hand, for the finite element analysis, the total number of finite elements used in the analysis is increased step by step until the FEM results converge to the exact analytical results. Table 1 shows that the SEM results are indeed identical to those obtained by the analytical formula (43), while the FEM results converge to the SEM results (or the exact results) as the total number of finite elements used in the finite element analysis is increased. For instance, Table 1 shows, for the present example problem, that more than 100 finite elements must be used for the finite element analysis to satisfy an accuracy of five significant figures for the fifth and higher natural frequencies while the one-element model suffices for the spectral element analysis. The maximum number of natural frequencies which can be obtained by finite element analysis is certainly limited by the total number of finite elements used in the analysis (for example, four natural frequencies when two finite elements are used, as shown in Table 1), while the present spectral element analysis provides an infinite number of natural frequencies.

The natural frequencies of the spinning uniform shaft are compared in Table 2. It is assumed that the uniform shaft is spinning at a constant speed of 3600 rpm. The SEM results are compared with those obtained by using the finite element model as well as with those obtained from the analytical formula given by [Zu and Han 1992] as

$$\sin\left(\frac{L}{\sqrt{2}}\sqrt{\chi_1\eta_5+\sqrt{\chi_1^2\eta_5^2-4\chi_2}}\right)=0, \tag{45}$$

where

$$\begin{aligned}\chi_1 &= -\eta_6\Omega\omega+(\eta_1+\eta_2)\omega^2,\\ \chi_2 &= -\omega-\eta_3\Omega\omega^3+\eta_4\omega^4,\end{aligned}\qquad \eta_4=\frac{\rho I}{\kappa GA},\qquad \eta_5=\frac{\rho A}{EI},\qquad \eta_6=\frac{\rho J}{\rho A}. \tag{46}$$

Table 2 also shows that the natural frequencies for both forward and backward whirling modes obtained by using the spectral element model (the one-element model) are very close to the results obtained by using the analytical formula (45), while those obtained by using the finite element model converge to the SEM results as the total number of finite elements used in the finite element analysis is increased. Figure 3 shows the spinning speed Ω-dependence of the first and second natural frequencies, all computed

Mode		FEM (n)						
		$n = 2$	$n = 10$	$n = 30$	$n = 50$	$n = 100$	SEM (1)	Z&H
1st	forward	20.45	20.37	20.37	20.37	20.37	20.37	20.37
	backward	20.42	20.34	20.34	20.34	20.34	20.34	
2nd	forward	90.41	81.36	81.34	81.34	81.34	81.34	81.34
	backward	90.29	81.24	81.23	81.23	81.23	81.23	
3rd	forward	227.1	182.7	182.6	182.6	182.6	182.6	182.6
	backward	226.8	182.5	182.3	182.3	182.3	182.3	
4th	forward	414.4	324.3	323.5	323.5	323.5	323.5	323.5
	backward	413.9	323.8	323.1	323.0	323.0	323.0	
5th	forward	-	506.1	503.4	503.3	503.3	503.3	503.3
	backward	-	505.4	502.7	502.6	502.6	502.6	
10th	forward	-	2234	1953	1948	1947	1946	1946
	backward	-	2231	1951	1946	1944	1943	
15th	forward	-	5524	4231	4185	4168	4163	4163
	backward	-	5518	4225	4180	4163	4158	
20th	forward	-	10267	7264	7061	6985	6961	6961
	backward	-	10255	7257	7054	6978	6954	

Table 2. Natural frequencies (in Hz) of the simply supported spinning uniform shaft ($\Omega = 3600\,\text{rpm}$), with n the total number of finite elements used in the analysis, and where Z&H indicates data from [Zu and Han 1992].

by using the present spectral element model. Figure 3 shows that both forward and backward whirling modes appear when the uniform shaft starts spinning.

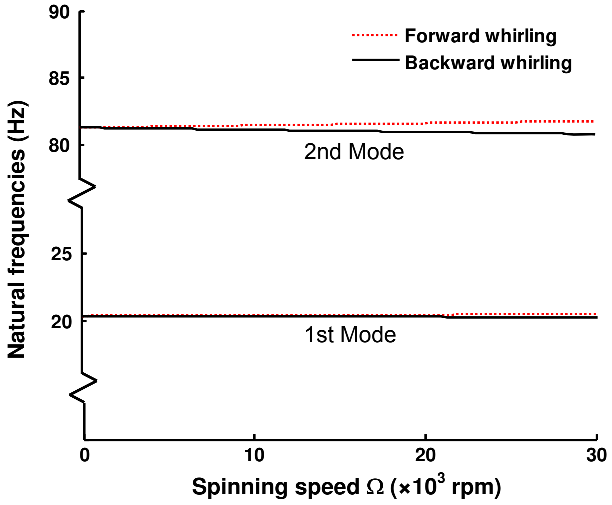

Figure 3. Natural frequencies versus spinning speed Ω of the simply supported uniform shaft.

		FEM (n)						
Mode		$n=2$	$n=10$	$n=30$	$n=50$	$n=100$	SEM (1)	E&E
1st	forward	20.44	20.36	20.36	20.36	20.36	20.36	20.36
	backward	20.43	20.35	20.35	20.35	20.35	20.35	20.35
2nd	forward	90.44	81.38	81.37	81.36	81.36	81.36	81.36
	backward	90.26	81.22	81.21	81.21	81.21	81.21	81.21
3rd	forward	227.5	183.0	182.9	182.8	182.8	182.8	182.8
	backward	226.4	182.2	182.1	182.0	182.0	182.0	182.0
4th	forward	415.9	325.3	324.6	324.5	324.5	324.5	324.5
	backward	412.4	322.8	322.1	322.0	322.0	322.0	322.0
5th	forward	-	508.8	506.1	506.0	506.0	506.0	506.0
	backward	-	502.8	500.1	500.0	500.0	500.0	499.9
10th	forward	-	2289	2001	1995	1994	1989	1989
	backward	-	2180	1912	1907	1906	1901	1901
15th	forward	-	5835	4413	4360	4341	4350	4350
	backward	-	5252	4063	4022	4007	3971	3971
20th	forward	-	11449	7770	7548	7465	7454	7454
	backward	-	10971	6752	6563	6489	6462	6462

Table 3. Critical speeds (in Hz) of the simply supported spinning uniform shaft, with n the total number of finite elements used in the analysis, and where E&E indicates data from [Eshleman and Eubanks 1969].

The critical speeds of the uniform shaft are compared in Table 3. The critical speeds of a spinning shaft are defined by the spinning speeds which are identical to the natural frequencies of the shaft. As the gyroscopic effect will change the effective compliance of the shaft to raise or lower the natural frequencies, one critical speed is raised (forward whirling mode) while one is lowered (backward whirling mode). The critical speeds obtained by using the present spectral element model are compared with the results obtained by using the finite element model and the analytical formula given by [Eshleman and Eubanks 1969] as

$$\Omega_n = \begin{cases} \bar{f}_n \sqrt{\dfrac{\alpha_n^2}{\alpha_n^2 + \eta_2 - \eta_1}} \ \text{(Hz)} & \text{(forward whirling),} \\ \bar{f}_n \sqrt{\dfrac{\alpha_n^2}{\alpha_n^2 + \eta_2 + 3\eta_1}} \ \text{(Hz)} & \text{(backward whirling).} \end{cases} \tag{47}$$

It is also obvious from Table 3 that the critical speeds of the present spectral element model (the one-element model) are very close to the results of the analytical formula (47), while the FEM results certainly converge to the SEM results as the total number of finite elements used in the finite element analysis is increased.

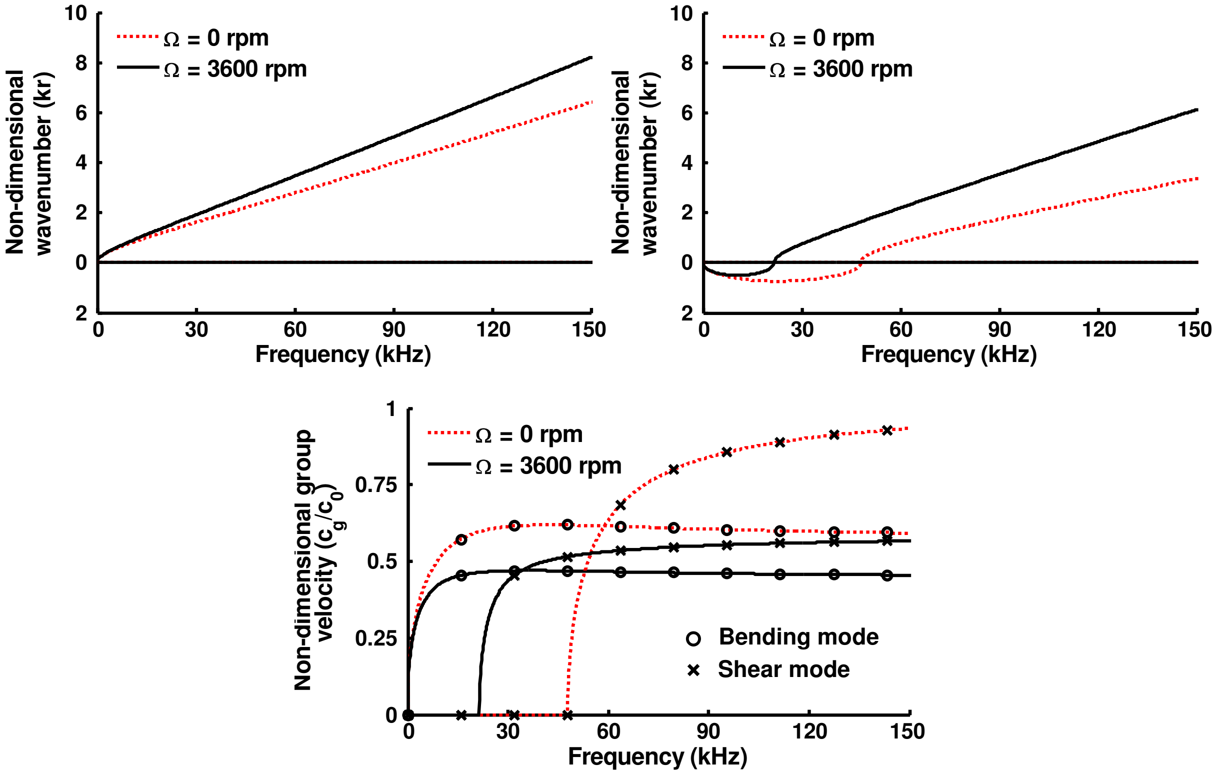

Figure 4. Dispersion curves of the simply supported uniform shaft.

In summary, the results displayed in Tables 1, 2, and 3 confirm the accuracy of the present spectral element model when compared with the conventional finite element model which is provided in the Appendix.

Lastly, Figure 4 compares the dispersion curves when the shaft is stationary and rotating at a constant speed of 3600 rpm. In the last graph, the group velocities are nondimensionalized with respect to $c_0 = \sqrt{EI/\rho A}$. Figure 4 shows that the group velocity of the bending (flexural) wave mode decreases as the shaft rotates. For the shear wave mode, the cutoff frequency shifts to a lower frequency as the shaft rotates and its group velocity also decreases at higher frequencies than the cutoff frequency.

5.2. ***Bearing-supported uniform shaft.*** To investigate the effect of the stiffness and damping of the bearing-supports on the natural and critical speeds of a spinning shaft, we consider a bearing-supported uniform shaft as shown in Figure 5 as the second example problem. The geometric and material properties for the bearing-supported uniform shaft are exactly same as those for the previous simply supported

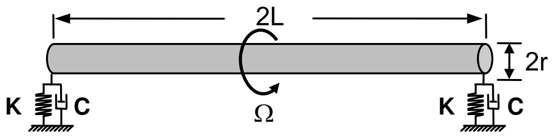

Figure 5. A bearing-supported uniform shaft, where Ω is the spinning speed.

uniform shaft. It is assumed that the stiffness and damping properties of the left bearing-support are identical to those of the right. For the stiffness and damping properties of the bearing-supports, we consider three cases:

- Case A: $K_{yy} = K_{zz} = 1.0 \times 10^6\,\text{N/m}$, $K_{yz} = K_{zy} = 0\,\text{N/m}$, $C_{yy} = C_{zz} = 400\,\text{Ns/m}$, and $C_{yz} = C_{zy} = 0\,\text{Ns/m}$;
- Case B: $K_{yy} = K_{zz} = 1.0 \times 10^8\,\text{N/m}$, $K_{yz} = K_{zy} = 0\,\text{N/m}$, $C_{yy} = C_{zz} = 400\,\text{Ns/m}$, and $C_{yz} = C_{zy} = 0\,\text{Ns/m}$;
- Case C: $K_{yy} = K_{zz} = 1.0 \times 10^6\,\text{N/m}$, $K_{yz} = K_{zy} = 0\,\text{N/m}$, $C_{yy} = C_{zz} = 800\,\text{Ns/m}$, and $C_{yz} = C_{zy} = 0\,\text{Ns/m}$.

Compared to Case A, Case B has higher stiffness, while Case C has lower damping.

For these three cases of bearing-supported uniform shaft problems, exact solutions are not available from the literature. Thus, as shown in Tables 4, 5, and 6, the FEM results are also provided as reference solutions to evaluate the present SEM results. The one-element model suffices for accurate SEM results. On the other hand, a sufficient number of finite elements (100 finite elements) are used to obtain sufficiently converged accurate FEM results.

Table 4 shows the lowest three natural frequencies for uniform shafts which are not spinning, while Table 5 shows the forward and backward natural frequencies of the lowest three modes for uniform shafts which are spinning at $\Omega = 3600\,\text{rpm}$. Lastly Table 6 shows the forward and backward critical speeds of

	Case A		Case B		Case C	
Mode	SEM (1)	FEM (100)	SEM (1)	FEM (100)	SEM (1)	FEM (100)
1st	19.13	19.13	20.34	20.34	19.14	19.14
2nd	63.61	63.61	81.08	81.08	64.19	64.19
3rd	110.6	110.6	181.4	181.4	111.5	111.5

Table 4. Natural frequencies (in Hz) of the simply supported stationary stepped shafts ($\Omega = 0\,\text{rpm}$), with the number in parentheses being the total number of finite elements used in the analysis.

		Case A		Case B		Case C	
Mode		SEM (1)	FEM (100)	SEM (1)	FEM (100)	SEM (1)	FEM (100)
1st	forward	19.14	19.14	20.35	20.35	19.15	19.15
	backward	19.12	19.12	20.32	20.32	19.13	19.13
2nd	forward	63.64	63.64	81.14	81.14	64.22	64.22
	backward	63.59	63.59	81.02	81.02	64.17	64.17
3rd	forward	110.7	110.7	181.5	181.5	111.6	111.6
	backward	110.6	110.6	181.3	181.3	111.5	111.5

Table 5. Natural frequencies (in Hz) of the simply supported spinning stepped shafts ($\Omega = 3600\,\text{rpm}$), with the number in parentheses being the total number of finite elements used in the analysis.

Mode		Case A SEM (1)	Case A FEM (100)	Case B SEM (1)	Case B FEM (100)	Case C SEM (1)	Case C FEM (100)
1st	forward	19.14	19.14	20.34	20.34	19.143	19.143
	backward	19.13	19.13	20.33	20.33	19.136	19.136
2nd	forward	63.64	63.64	81.16	81.16	64.22	64.22
	backward	63.59	63.59	81.00	81.00	64.17	64.17
3rd	forward	110.7	110.7	181.8	181.8	111.6	111.6
	backward	110.5	110.5	181.0	181.0	111.4	111.4

Table 6. Critical speeds (in Hz) of the simply supported spinning stepped shafts, with the number in parentheses being the total number of finite elements used in the analysis.

the lowest three modes. The effects of the stiffness and damping of the bearing-supports on the natural frequencies and critical speeds can be observed in Tables 4, 5, and 6. When compared with Case A, both Cases B, with bearing-supports of higher stiffness, and C, with bearing-supports of higher damping, have higher natural frequencies and critical speeds.

5.3. ***Bearing-supported stepped shaft.*** As the third example problem, consider a bearing-supported stepped shaft which consists of two uniform shafts of equal length $L = 1$ m as shown in Figure 6. The material properties for the two uniform shafts are identical to those used the previous two example problems. The spring constants and viscous damping coefficients for the left and right bearing-supports are identical, and they are assumed to be identical to those for Case A of the previous bearing-supported uniform shaft problem. For the radii of the two equal-length uniform shafts, we consider three cases:

- Case I: $r_1 = r_2 = 0.02\,\text{m}$;
- Case II: $r_1 = 0.02\,\text{m}$, $r_2 = 0.01\,\text{m}$;
- Case III: $r_1 = 0.02\,\text{m}$, $r_2 = 0.03\,\text{m}$.

Exact solutions are not available from the literature for these three cases of bearing-supported stepped shaft problems. Thus, as shown in Tables 7, 8, and 9, the FEM results are also provided as the reference solutions to evaluate the present SEM results. A sufficient number of finite elements (100 finite elements) is used to obtain sufficiently converged accurate FEM results. For the SEM results, a one-element model is used for Case I, while two-element models are used for Cases II and III due to the existence of a single geometric discontinuity at the middle of the stepped shafts.

Table 7 displays the lowest three natural frequencies when the stepped shafts are not spinning, while Table 8 displays the forward and backward natural frequencies of the lowest three modes when the stepped shafts are spinning at $\Omega = 3600\,\text{rpm}$. Lastly Table 9 displays the forward and backward critical

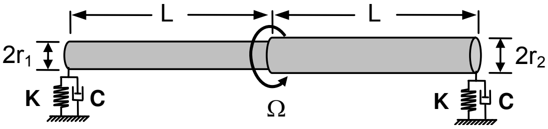

Figure 6. A bearing-supported stepped shaft, where Ω is the spinning speed.

speeds of the lowest three modes. The natural frequencies and critical speeds for Case III are shown to be higher than for Cases I and II for the first mode. However, for the second and third modes, the values for Case I are higher than for Cases II and III. In addition, the natural frequencies and critical speeds given in Tables 7, 8, and 9 for the bearing-supported uniform shaft (Case I) are shown to be lower than the values given in Tables 1, 2, and 3 for the simply supported uniform shaft.

Figure 7 shows the first three normalized modes of the transverse displacement $v(x,t)$ when the stepped shafts are spinning at $\Omega = 0\,\text{rpm}$ and $\Omega = 3600\,\text{rpm}$. The mode shapes for the stepped shafts

	Case I		Case II		Case III	
Mode	SEM (1)	FEM (100)	SEM (2)	FEM (100)	SEM (2)	FEM (100)
1st	19.13	19.13	9.563	9.563	19.28	19.28
2nd	63.61	63.61	56.32	56.32	58.46	58.46
3rd	110.6	110.6	93.15	93.15	103.2	103.2

Table 7. Natural frequencies (in Hz) of the bearing-supported stationary stepped shafts ($\Omega = 0\,\text{rpm}$), with the number in parentheses being the total number of finite elements used in the analysis.

		Case I		Case II		Case III	
Mode		SEM (1)	FEM (100)	SEM (2)	FEM (100)	SEM (2)	FEM (100)
1st	forward	19.14	19.14	9.578	9.578	19.29	19.29
	backward	19.12	19.12	9.551	9.551	19.26	19.26
2nd	forward	63.64	63.64	56.34	56.34	58.51	58.51
	backward	63.59	63.59	56.30	56.30	58.42	58.42
3rd	forward	110.7	110.7	93.20	93.20	103.3	103.3
	backward	110.6	110.6	93.10	93.10	103.1	103.1

Table 8. Natural frequencies (in Hz) of the bearing-supported spinning stepped shafts ($\Omega = 3600\,\text{rpm}$), with the number in parentheses being the total number of finite elements used in the analysis.

		Case I		Case II		Case III	
Mode		SEM (1)	FEM (100)	SEM (2)	FEM (100)	SEM (2)	FEM (100)
1st	forward	19.14	19.14	9.565	9.565	19.28	19.28
	backward	19.13	19.13	9.561	9.561	19.27	19.27
2nd	forward	63.64	63.64	56.34	56.34	58.51	58.51
	backward	63.59	63.59	56.30	56.30	58.42	58.42
3rd	forward	110.7	110.7	93.23	93.23	103.4	103.4
	backward	110.5	110.5	93.07	93.07	103.1	103.1

Table 9. Critical speeds (in Hz) of the bearing-supported spinning stepped shafts, with the number in parentheses being the total number of finite elements used in the analysis.

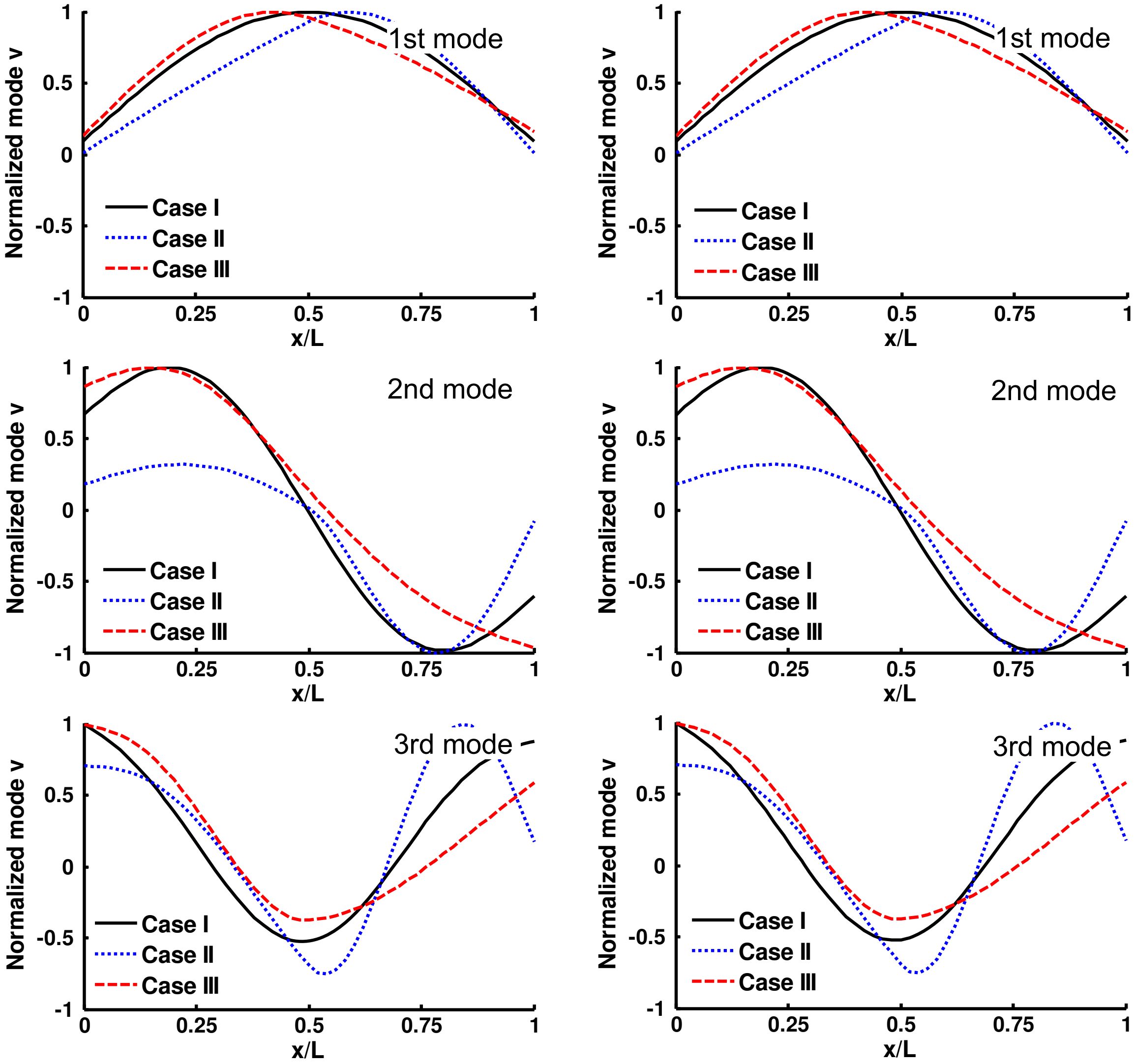

(a) $\Omega = 0\,\mathrm{rpm}$ (b) $\Omega = 3600\,\mathrm{rpm}$

Figure 7. The first three normalized modes of the bearing-supported stepped shafts.

(Cases II and III) are shown to deviate significantly from those for the uniform shaft (Case I) at both $\Omega = 0\,\mathrm{rpm}$ and $\Omega = 3600\,\mathrm{rpm}$. Though the mode shapes are dependent on the spinning speed, Figure 7 shows that the change of mode shapes at $\Omega = 3600\,\mathrm{rpm}$ is not so significant for the example shafts considered herein.

6. Conclusions

This paper develops a spectral element model for a spinning uniform shaft. The spinning uniform shaft is represented by a spinning uniform Timoshenko beam model and its bearing-supports are represented by two translational springs and two rotational springs. The spectral element model is then used to investigate the natural frequencies and critical speeds of the simply supported and bearing-supported spinning uniform shafts and the results are compared with the results obtained by using the conventional finite element model and the analytical theories available in existing references. It is numerically shown that the present spectral element model provides extremely accurate results by using only a small number of finite elements when compared with the conventional finite element model. In addition, some numerical investigation is also conducted for the bearing-supported stepped shafts.

Appendix: Finite element model

The equations of motion for the transverse bending vibration are given by (10) and the corresponding weak form can be derived in the form

$$\begin{aligned}&\int_0^L [EI(\phi'\delta\phi'+\psi'\delta\psi')+\kappa GA(v'\delta v'+w'\delta w')-\kappa GA(\psi\delta v'+v'\delta\psi)+\kappa GA(\phi\delta w'+w'\delta\phi)\\&+\kappa GA(\phi\delta\phi+\psi\delta\psi)]\,dx+\int_0^L \Omega\rho J(\dot{\psi}\delta\phi-\dot{\phi}\delta\psi)\,dx+\int_0^L[\rho A(\ddot{v}\delta v+\ddot{w}\delta w)+\rho I(\ddot{\phi}\delta\phi+\ddot{\psi}\delta\psi)]\,dx\\&=\int_0^L(p_y\delta v+\tau_z\delta\psi+p_z\delta w+\tau_y\delta\phi)\,dx+Q_y\delta v\big|_0^L+M_z\delta\psi\big|_0^L+Q_z\delta w\big|_0^L+M_y\delta\phi\big|_0^L.\end{aligned}\tag{A.1}$$

The displacement fields $v(x,t)$, $w(x,t)$, $\phi(x,t)$, and $\psi(x,t)$ are represented by

$$v=\boldsymbol{N}_v(x)\boldsymbol{d}(t),\quad w=\boldsymbol{N}_w(x)\boldsymbol{d}(t),\quad \phi=\boldsymbol{N}_\phi(x)\boldsymbol{d}(t),\quad \psi=\boldsymbol{N}_\psi(x)\boldsymbol{d}(t),\tag{A.2}$$

where

$$\boldsymbol{d}(t)=\{\boldsymbol{d}_1(t)\ \ \boldsymbol{d}_2(t)\}^T,\qquad \boldsymbol{d}_j(t)=\{v_j(t)\ \ \psi_j(t)\ \ w_j(t)\ \ \phi_j(t)\}^T\quad (j=1,2),\tag{A.3}$$

and

$$\begin{aligned}\boldsymbol{N}_v(x)&=[(1-\xi)(2-\xi-\xi^2+6r)(R/4)\ \ L(1-\xi^2)(1-\xi+3r)(R/8)\ \ 0\ \ 0\\&\qquad(1+\xi)(2+\xi-\xi^2+6r)(R/4)\ \ -L(1-\xi^2)(1+\xi+3r)(R/8)\ \ 0\ \ 0],\\ \boldsymbol{N}_w(x)&=[0\ \ 0\ \ (1-\xi)(2-\xi-\xi^2+6r)(R/4)\ \ -L(1-\xi^2)(1-\xi+3r)(R/8)\\&\qquad 0\ \ 0\ \ (1+\xi)(2+\xi-\xi^2+6r)(R/4)\ \ L(1-\xi^2)(1+\xi+3r)(R/8)],\\ \boldsymbol{N}_\phi(x)&=[0\ \ 0\ \ 3(1-\xi^2)(R/2L)\ \ -(1-\xi)(1+3\xi-6r)(R/4)\\&\qquad 0\ \ 0\ \ -3(1-\xi^2)(R/2L)\ \ -(1+\xi)(1-3\xi-6r)(R/4)],\\ \boldsymbol{N}_\psi(x)&=[-3(1-\xi^2)(R/2L)\ \ -(1-\xi)(1+3\xi-6r)(R/4)\ \ 0\ \ 0\\&\qquad 3(1-\xi^2)(R/2L)\ \ -(1+\xi)(1-3\xi-6r)(R/4)\ \ 0\ \ 0],\end{aligned}\tag{A.4}$$

with

$$\xi=2\Big(\frac{x}{L}\Big)-1\quad(0\le x\le L),\qquad r=\frac{4EI}{\kappa GAL^2},\qquad R=\frac{1}{1+3r}.\tag{A.5}$$

Substitution of (A.2) into (A.1) gives the finite element equation in the form

$$\boldsymbol{M}\ddot{\boldsymbol{d}}(t)+\boldsymbol{G}\dot{\boldsymbol{d}}(t)+\boldsymbol{K}\boldsymbol{d}(t)=\boldsymbol{f}(t), \tag{A.6}$$

where

$$\begin{aligned}
\boldsymbol{M}=[m_{ij}]&=\int_0^L[\rho A(\boldsymbol{N}_v^T\boldsymbol{N}_v+\boldsymbol{N}_w^T\boldsymbol{N}_w)+\rho I(\boldsymbol{N}_\phi^T\boldsymbol{N}_\phi+\boldsymbol{N}_\psi^T\boldsymbol{N}_\psi)]\,dx,\\
\boldsymbol{G}=[g_{ij}]&=\int_0^L\Omega\rho J(\boldsymbol{N}_\phi^T\boldsymbol{N}_\psi-\boldsymbol{N}_\psi^T\boldsymbol{N}_\phi)\,dx,\\
\boldsymbol{K}=[k_{ij}]&=\int_0^L[EI(\boldsymbol{N}_\phi'^T\boldsymbol{N}_\phi'+\boldsymbol{N}_\psi'^T\boldsymbol{N}_\psi')+\kappa GA(\boldsymbol{N}_v'^T\boldsymbol{N}_v'+\boldsymbol{N}_w'^T\boldsymbol{N}_w'+\boldsymbol{N}_\phi^T\boldsymbol{N}_\phi\\
&\qquad+\boldsymbol{N}_\psi^T\boldsymbol{N}_\psi+\boldsymbol{N}_w'^T\boldsymbol{N}_\phi+\boldsymbol{N}_\phi^T\boldsymbol{N}_w'-\boldsymbol{N}_v'^T\boldsymbol{N}_\psi-\boldsymbol{N}_\psi^T\boldsymbol{N}_v')]\,dx,
\end{aligned} \tag{A.7}$$

and

$$\begin{aligned}
\boldsymbol{f}(t)&=\boldsymbol{f}_c(t)+\boldsymbol{f}_d(t)\equiv\left\{\boldsymbol{f}_1(t)\ \ \boldsymbol{f}_2(t)\right\}^T,\\
\boldsymbol{f}_c(t)&=\left\{Q_{y1}(t)\ \ M_{z1}(t)\ \ Q_{z1}(t)\ \ M_{y1}(t)\ \ Q_{y2}(t)\ \ M_{z2}(t)\ \ Q_{z2}(t)\ \ M_{y2}(t)\right\}^T,\\
\boldsymbol{f}_d(t)&=\int_0^L(\boldsymbol{N}_v^Tp_y+\boldsymbol{N}_w^Tp_z+\boldsymbol{N}_\phi^T\tau_y+\boldsymbol{N}_\psi^T\tau_z)\,dx,\\
\boldsymbol{f}_i(t)&=\left\{f_{vi}(t)\ \ f_{\psi i}(t)\ \ f_{wi}(t)\ \ f_{\phi i}(t)\right\}^T\quad(i=1,2).
\end{aligned} \tag{A.8}$$

$\boldsymbol{M}$ and $\boldsymbol{K}$ are the 8×8 symmetric matrices and $\boldsymbol{G}$ is the 8×8 skew symmetric matrix. Their components are given by

$$\begin{aligned}
&m_{11}=m_{33}=m_{55}=m_{77}=12\alpha_1(26+147r+210r^2)+36\alpha_2,\\
&m_{12}=-m_{34}=-m_{56}=m_{78}=\alpha_1L(44+231r+315r^2)+3\alpha_2L(1-15r),\\
&m_{15}=m_{37}=36\alpha_1(3+21r+35r^2)-36\alpha_2,\\
&m_{16}=-m_{25}=-m_{38}=m_{47}=-\alpha_1L(26+189r+315r^2)+3\alpha_2L(1-15r),\\
&m_{22}=m_{44}=m_{66}=m_{88}=\alpha_1L^2(8+42r+63r^2)+\alpha_2L^2(4+15r+90r^2),\\
&m_{26}=m_{48}=-3\alpha_1L^2(2+14r+21r^2)-\alpha_2L^2(1+15r-45r^2),
\end{aligned} \tag{A.9}$$

and other $m_{ij}=0$,

$$\begin{aligned}
&g_{13}=-g_{17}=g_{35}=g_{57}=36\eta,\\
&g_{14}=g_{18}=-g_{23}=g_{27}=g_{36}=g_{45}=-g_{58}=g_{67}=-3\eta L(1-15r),\\
&g_{24}=g_{68}=-\eta L^2(4+15r+90r^2),\\
&g_{28}=-g_{46}=\eta L^2(1+15r-45r^2),
\end{aligned} \tag{A.10}$$

and other $g_{ij} = 0$, and

$$\begin{aligned}
k_{11} &= -k_{15} = k_{33} = -k_{37} = k_{55} = k_{77} = 12\beta_1 + 540\beta_2 r^2,\\
k_{12} &= -k_{25} = -k_{34} = k_{47} = 6\beta_1 L + 270\beta_2 L r^2,\\
k_{16} &= -k_{38} = -k_{56} = k_{78} = 6\beta_1 L + 90\beta_2 L r(1+3r),\\
k_{22} &= k_{44} = \beta_1 L^2(4+6r+9r^2) + 135\beta_2 L^2 r^2,\\
k_{26} &= k_{48} = \beta_1 L^2(2-6r-9r^2) + 45\beta_2 L^2 r(1+3r),\\
k_{66} &= k_{88} = \beta_1 L^2(4+6r+9r^2) + \beta_2 L^2(47+210r+315r^2),
\end{aligned} \tag{A.11}$$

and other $k_{ij} = 0$, where

$$\alpha_1 = \frac{R^2}{840}\rho A L, \qquad \beta_1 = \frac{R^2}{L^3} E I, \qquad \eta = \frac{R^2}{30L}\rho J \Omega. \qquad \alpha_2 = \frac{R^2}{30L}\rho I, \qquad \beta_2 = \frac{R^2}{60L}\kappa G A, \tag{A.12}$$

References

[Blevins 1979] R. D. Blevins, *Formulas for natural frequency and mode shape*, Van Nostrand Reinhold, New York, 1979.

[Chen 2010] W.-R. Chen, "On the vibration and stability of spinning axially loaded pre-twisted Timoshenko beams", *Finite Elem. Anal. Des.* **46**:11 (2010), 1037–1047.

[Doyle 1997] J. F. Doyle, *Wave propagation in structures: spectral analysis using fast discrete Fourier transforms*, Springer, New York, 1997.

[Ehrich 1992] F. F. Ehrich, *Handbook of rotordynamics*, McGraw-Hill, New York, 1992.

[Eshleman and Eubanks 1969] R. L. Eshleman and R. A. Eubanks, "On the critical speeds of a continuous rotor", *J. Eng. Ind.* (*ASME*) **91** (1969), 1180–1188.

[Ghoneim and Lawrie 2007] H. Ghoneim and D. J. Lawrie, "Dynamic analysis of a hyperbolic composite coupling", *J. Sound Vib.* **301**:1-2 (2007), 43–58.

[Kane and Torby 1991] K. Kane and B. J. Torby, "The extended modal reduction method applied to rotor dynamic problems", *J. Vib. Acoust.* (*ASME*) **113**:1 (1991), 79–84.

[Lee 2009] U. Lee, *Spectral element method in structural dynamics*, Wiley, Singapore, 2009.

[Lee et al. 2000] U. Lee, J. Kim, and A. Y. T. Leung, "The spectral element method in structural dynamics", *Shock Vib. Digest* **32**:6 (2000), 451–465.

[Lund 1974] J. W. Lund, "Stability and damped critical speeds of a flexible rotor in fluid-film bearings", *J. Eng. Ind.* (*ASME*) **96**:2 (1974), 509–517.

[Meirovitch 1980] L. Meirovitch, *Computational methods in structural dynamics*, Monographs and Textbooks on Mechanics of Solids and Fluids: Mechanics of Dynamical Systems **5**, Sijthoff & Noordhoff, Alphen aan den Rijn, 1980.

[Nelson 1980] H. D. Nelson, "A finite rotating shaft element using Timoshenko beam theory", *J. Mech. Des.* (*ASME*) **102**:4 (1980), 793–803.

[Nelson 2003] F. C. Nelson, "A brief history of early rotor dynamics", *Sound Vib.* **37**:6 (2003), 8–11.

[Ruhl and Booker 1972] R. L. Ruhl and J. F. Booker, "A finite element model for distributed parameter turborotor systems", *J. Eng. Ind.* (*ASME*) **94**:1 (1972), 126–132.

[Vinod et al. 2007] K. G. Vinod, S. Gopalakrishnan, and R. Ganguli, "Free vibration and wave propagation analysis of uniform and tapered rotating beams using spectrally formulated finite elements", *Int. J. Solids Struct.* **44**:18-19 (2007), 5875–5893.

[Wittrick and Williams 1971] W. H. Wittrick and F. W. Williams, "A general algorithm for computing natural frequencies of elastic structures", *Q. J. Mech. Appl. Math.* **24**:3 (1971), 263–284.

[Zu and Han 1992] J. W.-Z. Zu and R. P. S. Han, "Natural frequencies and normal modes of a spinning Timoshenko beam with general boundary conditions", *J. Appl. Mech.* (*ASME*) **59**:2S (1992), S197–S204.

Received 18 Apr 2011. Revised 23 Jun 2011. Accepted 23 Jun 2011.

USIK LEE: `ulee@inha.ac.kr`
Department of Mechanical Engineering, Inha University, 253 Yonghyun-Dong, Nam-Gu, Incheon 402-751, South Korea

INJOON JANG: `injoonjang@inha.edu`
Department of Mechanical Engineering, Inha University, 253 Yonghyun-Dong, Nam-Gu, Incheon 402-751, South Korea

JOURNAL OF MECHANICS OF MATERIALS AND STRUCTURES
Vol. 7, No. 2, 2012

ON INDENTER BOUNDARY EFFECTS AT ELASTIC CONTACT

DENIS JELAGIN AND PER-LENNART LARSSON

Axisymmetric contact problems at finite Coulomb friction and rounded profiles are examined for linear elastic solids. In previous analytical/numerical approaches to this problem often incremental procedures have been developed resulting in a reduced incremental problem corresponding to a rigid flat indentation of an elastic half-space. The reduced problem, being independent of loading and contact region, can be solved by a finite element method based on a stationary contact contour and characterized by high accuracy. Subsequently, with cumulative superposition procedures it is then possible to resolve the original problem in order to determine global and local field values. Such a procedure, when applied to for example to flat and conical profiles with rounded edges and apices, is exact save for the influence from boundaries close to the contact region. This influence could be exemplified by the indenter boundaries of a flat deformable profile with rounded edges indenting a linear elastic half-space. In the present analysis such effects are investigated qualitatively and quantitatively. In doing so, the results derived using previously discussed analytical/numerical approaches are compared with corresponding ones from full-field finite element calculations. Both local as well as global quantities are included in the comparison in order to arrive at a complete understanding of the boundary effects at elastic contact.

1. Introduction

Following the classical results by Hertz [1882] for normal frictionless contact between two linear elastic nonconforming bodies of elliptical profiles the corresponding problem was attacked for adhesive contact by Mossakovskii [1963] and Spence [1968] and for finite friction by Spence [1975a; 1975b]. Even though the Hertz formulation was based on linear elasticity and linear kinematics, the problem is indeed nonlinear due to the presence of a moving contact boundary. At finite friction further nonlinearities will evolve as stick-slip boundaries then have to be determined when partial slip occurs. In this context substantial progress was made by Spence [1975a; 1975b], who showed that under monotonic loading a single stick-slip contour will evolve being independent of the contact profile provided it has a polynomial shape. More recently (see [Ciavarella and Hills 1999; Ciavarella 1999; Argatov 2002; Jaffar 2002; Storåkers and Elaguine 2005]], contact of various nonstandard profiles such as blunted cones and flat indenters with rounded edges, has been investigated. Besides a more general contact law behavior, the main intention has been to predict initiation of plastic flow or the occurrence of brittle fracture (also the contact behavior at nanoindentation is an interesting feature in this context; see [Fu 2006; Fu and Cao 2009]). Related experimental work has been presented in [Pau et al. 2006], for example.

Mossakovskii [1963] seems to have been the first to propose that normal contact problems at adhesive behavior may be attacked in two steps, by first solving the problem at an incremental advance and subsequently apply superposition. By emphasizing self-similarity for power-law profiles, further advances

---

Keywords: Contact mechanics, Elastic material, Friction, Indenter boundary effects.

were made by Spence [1968; 1975a; 1975b]. Mossakovskii and Spence were mainly concerned with determination of surface tractions and displacements. Mossakovskii's analysis was later developed for indentation methods by Borodich and Keer [2004]. In case of axisymmetric and frictionless contact it was later shown in [Hill and Storåkers 1990] that complete field values may readily be determined by a solution for incremental fields followed by the cumulative superposition along radial paths. Numerically, such a procedure is at advantage as only a stationary mesh is required when finite elements are to be used. In view of self similarity principles applied by Hill et al. [1989] the strategy was utilized in full by Storåkers and Larsson [1994] for Norton creep by combining a finite element procedure with cumulative superposition. For the case of linear viscosity, the approach corresponds to linear elasticity though with incompressibility anticipated. In subsequent work, hereditary material behavior was treated in the same spirit for the case of plastic flow theory [Biwa and Storåkers 1995] and viscoplasticity [Storåkers et al. 1997], with finite friction also included [Carlsson et al. 2000] and oblique (nonnormal) loading [Larsson and Storåkers 2002].

Presently, with linear elastic contact at issue, history dependence evolves through the presence of finite friction. However, it was shown in [Storåkers and Elaguine 2005] for the case of monotonically increasing loading that history dependence is only fictitious and that the stick-slip contour relative to the external contact contour will be invariant for any contact profile provided that it is smooth and convex and the loading is axisymmetric and monotonically increasing. In the same paper a consistent and robust method was described to solve frictional normal contact problems at smooth and convex but otherwise arbitrary profiles with special emphasis put on the presence of finite friction causing partial slip between dissimilar solids. For profiles represented by monomials self-similarity will prevail as has been thoroughly discussed, for instance in [Borodich 1993] and [Borodich and Galanov 2002], in case of finite friction and also nonlinear elasticity. Analytically this is a convenient property but it will be lost for general profiles.

Usually, the normal contact problem sketched refers to one rigid member impressed into one elastically deforming. This requires only a half-space solution to be dealt with. If two of the contacting solids are deforming, formally a full-space solution with proper interface conditions needs to be mastered save for the degenerate case of two identical elastic materials. It has been pointed out by Mossakovskii [1963] and Spence [1968; 1975a; 1975b], however, that the contact tractions arising may be determined from a single half-space solution by using a tailored combination of material parameters for two dissimilar solids. When these interface conditions are captured, the respective fields of the two solids may be obtained individually.

The above described theoretical approaches and computational procedures, applied to the different indentation problems; rest, however, on the assumption that, at contact of rounded profiles, any effects from the boundary of the deformable indenter outside of the contact region are negligible. This may be so in many situations of practical interest but is from a theoretical point of view not immediately obvious and has been discussed for the 2D half-plane case by Banerjee et al. [2009]. Argatov [2010] considered the size effect associated with the finite dimensions of the indented sample, and the size effects associated with material length scales included in constitutive description where studied in some detail by Huang et al. [2006] and Harsono et al. [2011]. At axisymmetric conditions size effects related to the dimensions of the deformable indenter have not been studied in detail previously and, accordingly, they will be investigated in the present analysis for the case of linear elasticity and a flat cylindrical punch with rounded edges. The latter case was chosen as it is expected that these boundary effects may be most significant for such a situation. It should be emphasized that this effect should not be confused with effects due to elastic deformation of the indenters in the contact region. This is sometimes called the indenter elasticity effect and is usually and also here as outlined below, considered in the analysis by using modified elastic parameters. The problem will be examined in detail using the finite element method and in particular the commercial finite element package ABAQUS is relied upon. It should be emphasized that the importance of the presently discussed problem is not limited to elastic indentation problems but is also relevant at for example analysis of fretting fatigue crack nucleation [Hills and Dini 2006; Nowell et al. 2006]. An accurate description of the local particle contact problem is of principal importance in discrete element modeling (DEM) of mechanical behavior of granular media (see Cundall and Hart [1992], for example) and in several other DEM applications. This include such problems as micromechanical analysis of powder compaction Heyliger and McMeeking [2001; Martin and Bouvard [2003; Martin et al. [2003; Skrinjar and Larsson [2004] and micromechanical modeling of rock materials [Matsuoka and Yamamoto 1993], as the size of the bodies in contact may be comparable to the characteristic contact dimensions (see [Thornton and Antony 1998] and [Thornton and Lanier 1997], for instance).

2. Formulation of the problem

The geometry of the problem to be analyzed is depicted in Figure 1 along with the notation; it involves contact between a flat indenter with rounded edges and a half-space under monotonically increasing load. It should be noted that this also includes the special cases of a flat and spherical indenters, as

$$b = a \quad \text{and} \quad b = 0 \tag{1}$$

respectively in Figure 1. The two solids are in a general case elastically dissimilar. The indenter geometry is defined by the indenter radius, w, indenter height, l, along with the radius of the flat part, b, and the

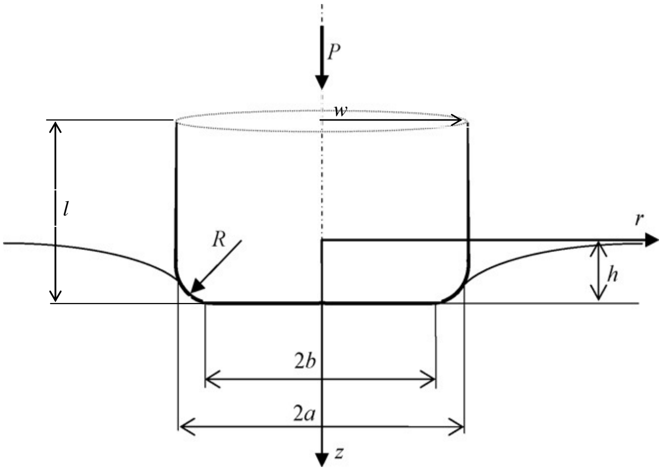

Figure 1. Geometry and notation of the problem of a flat indenter with a rounded corners indenting an elastic half-space.

curvature radius of the round-off, R. It should be noted that in case of a nonrigid indenter, the Hertz theory of contact is strictly valid only when w, l, $R \gg a$.

In the analysis, quasi-static conditions are assumed to prevail and in the absence of body forces, equilibrium equations may be expressed as

$$\sigma_{ij,j} = 0 \tag{2}$$

and strain-displacement relations as

$$\epsilon_{ij} = \left(\tfrac{1}{2}\right)(u_{i,j} + u_{j,i}) \tag{3}$$

in obvious notation and linear kinematics assumed. Furthermore, Hooke's law in the elastic solids is expressed in the form

$$\epsilon_{ij} = (1/2G)(\sigma_{ij} - (\nu/(1+\nu))\sigma_{kk}\delta_{ij}) \tag{4}$$

where G denotes the shear modulus and ν Poisson's ratio.

Coulomb friction is assumed to be valid at the interface between the elastic solids and the following boundary condition holds at points where frictional tractions are not sufficient to initiate tangential slip:

$$\mu|\sigma_{zz}(r)| - |\sigma_{rz}(r)| > 0, \quad \frac{\partial u_r(r,a)}{\partial a} = 0, \quad r \le c, \quad z = 0 \tag{5}$$

and at points where slip occurs

$$\mu|\sigma_{zz}(r)| - |\sigma_{rz}(r)| = 0, \quad \frac{\partial u_r(r,a)}{\partial a} \bigg/ \left|\frac{\partial u_r(r,a)}{\partial a}\right| = \sigma_{rz}(r)/|\sigma_{rz}(r)|, \quad c \le r \le a, \quad z = 0. \tag{6}$$

In Equations (5) and (6) c is the stick-slip radius.

Storåkers and Elaguine [2005] analyzed the present problem, depicted in Figure 1, and the corresponding one for a cone indenter with a rounded tip. In this investigation a reduced incremental problem was laid down based on a flat stationary boundary and modeled by finite elements. The reduced incremental problem concerned a rigid flat die indenting an elastic half-space. Subsequently, the original problem was readily solved by cumulative superposition as relative stick-slip contours proved to be invariant for any smooth and convex profile. As a consequence, in case of a rigid indenter, complete displacement and stress fields may be superposed for different contact profiles provided that monotonic loading prevails. Accordingly, when the interior fields are to be determined by for example a finite element method only a half-space solution is required.

When two dissimilar elastic solids are in contact solutions for interior fields are in general required in a full space. It has been shown, however, by Mossakovskii [1963] and Spence [1975b], that a half-space solution will still suffice to determine surface values. As explained in [Storåkers and Elaguine 2005], following [Spence 1975b], the stress state in the contact region between two elastic bodies is equivalent to that arising from contact between a rigid indenter and an elastic half-space with material parameters modified according to the relations:

$$\frac{1-\nu_m}{G_m} = \frac{1-\nu_1}{G_1} + \frac{1-\nu_2}{G_2}, \quad \frac{1-2\nu_m}{2G_m} = \frac{1-2\nu_1}{2G_1} + \frac{1-2\nu_2}{2G_2} \tag{7}$$

where G_m, ν_m are the modified elasticity parameters for the reduced rigid-elastic problem and g_i, ν_i $(i = 1, 2)$ are the elasticity parameters for the original two bodies in contact.

Thus, the resulting contact tractions may be directly determined by aid of a half-space solution procedure described in [Storåkers and Elaguine 2005]. As a result, two uncoupled problems pertinent to dissimilar half-spaces with prescribed normal and tangential stress distributions are obtained and the complete internal stress fields may be subsequently generated by two harmonic potentials as explained in detail in e.g. [Hills et al. 1993].

Accordingly, from the discussion above it is clear that the solutions to the contact problems described can be derived in a computationally favorable way from the solution of a reduced incremental problem with a stationary contact boundary corresponding to a flat rigid punch indenting an elastic half-space. However, due to the fact that the reduced incremental problem is rigid-elastic, unavoidable effects on global and local quantities from the boundaries of the indenter are not accounted for. The validity of this assumption in the case when the indenter has dimensions comparable with the contact size will be investigated here. In particular the attention will be focused on the influence of the relative indenter radius, w/a, on the contact conditions. In order to ensure that other indenter geometrical parameters do not contribute to the deviation from the Hertz theory (and to ensure the validity of the rigid-modified elastic solution), the indenter height, l, and the curvature radius, R, will be kept sufficiently large, as compared to the contact radius, in all of the simulations. This of course also indicates that the indentation depth is much smaller than the contact radius.

Provided that the dimensions of contacting bodies are large compared to the contact size (R/a, l/a, $w/a \gg 1$), the pressure and shear tractions distributions obtained at elastic-elastic and rigid-modified elastic formulations should be identical. Furthermore, the relative stick-slip radius, c/a is then invariant of indenter geometry as well as of depth of indentation and depends only on composite elastic coefficients and coefficient of friction, as shown for the case of smooth and convex, but otherwise arbitrary profiles by Storåkers and Elaguine [2005]. On the other hand, when the indenter dimensions are close to the contact radii, the invariance properties are lost and pressure and shear traction distribution are influenced by the global stress-strain state in the indenter, which is in turn controlled by the material parameters of the contact pair; the details of indenter geometry and of the load application. It seems to be impossible to establish a complete set of parameters describing any possible combination of the above. One would rather have to rely on numerical modeling to find out what exactly happens in each particular contact configuration. The main intention of the present study is to establish the limits of the validity of the rigid-modified elastic formulation with respect to the relative indenter radius, w/a. Situations with w/a close to 1 are considered to be of practical interest as they may be found in the contact configuration with flat indenters and flat indenter with rounded corners.

Contact between two dissimilar elastic bodies, as depicted in Figure 1, will be investigated in two different ways: by prescribing the respective elastic constants to each of the bodies and by prescribing high values to the elastic parameters of the indenter and modifying the elasticity parameters of the half-space according to (7). The discrepancy between the two solutions indicates the indenter boundary effects at issue presently.

In the present study an ABAQUS-based finite element method is used to analyze frictional contact between two dissimilar elastic bodies, as depicted in Figure 1, drawing upon the experience gained during previous and similar analyses [Elaguine et al. 2006; Jelagin and Larsson 2008a; 2008b]. In Figure 2 the

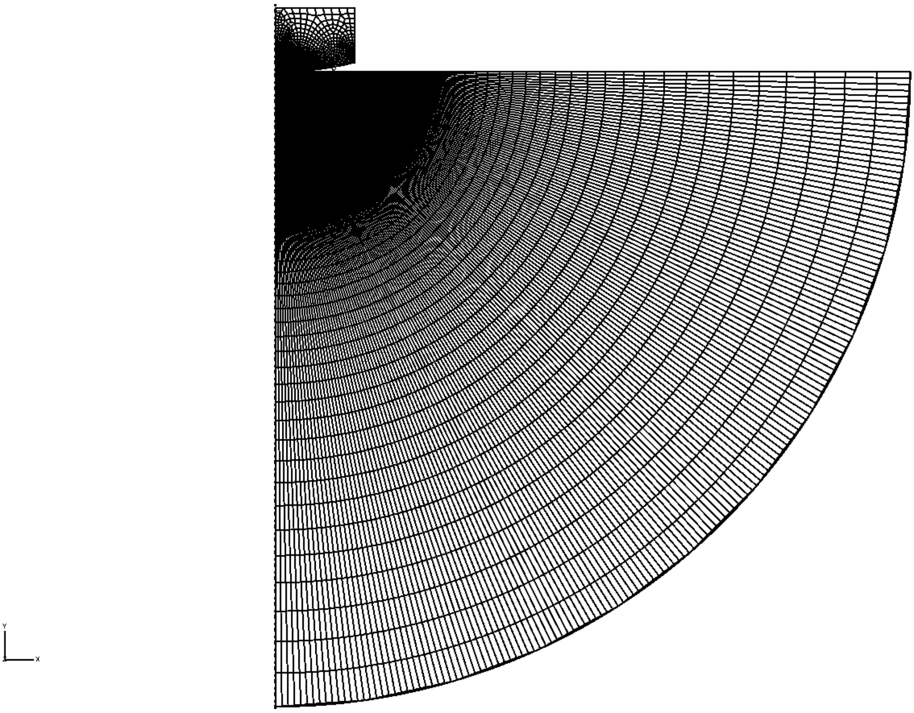

Figure 2. Finite element mesh; indenter with spherical contact profile.

finite element mesh is shown for the case of a spherical indenter with axisymmetry taken into account and with eight-noded isoparametric quadrilateral elements used. The contact pair is shown in Figure 2 for the particular case of the indenter with spherical contact profile and with $w = 25a_{\text{rigid\_sphere}}$. One may notice the domain with especially dense mesh in the vicinity of the contact region with the element size chosen to have at least 50 elements in contact. The outer boundary of the half-space was introduced to be at least 200 times the maximum contact radius in order to avoid remote boundary effects. At the outer boundary of the half-space the horizontal displacements were free to move while the vertical ones were set to vanish. The outer boundary of the indenter was set free outside the contact region. The load was applied by prescribing a uniform vertical displacement to the indenter's upper boundary.

A surface based contact formulation was used to model the interaction between two elastic bodies. At normal contact behavior, a hard contact formulation was used, where surfaces may not penetrate each other. To model the basic Coulomb friction Lagrange multiplier method was employed which allowed for sticking constraints to be enforced exactly.

In order to validate the numerical procedure developed presently, the global and local field values found at frictionless contact between a linear elastic half-space and rigid flat and spherical indenters were compared with the analytical solution due to Hertz [1882]. The global values were found to be accurate up to 0.3%, while the accuracy of the local field values was found to be within 1%.

The global and local field values obtained at frictional contact between a rigid indenter and a linear elastic half-space were compared to the ones found with an alternative computational procedure developed by Storåkers and Elaguine [2005]. Results were found to agree with 1% accuracy. As shown

	elastic-elastic contact E (GPa)	 ν	rigid-elastic contact E (GPa)	 ν
Indenter	200	0.300	1000	0.499
Halfspace	70	0.220	47.2	0.377

Table 1. Material parameters for the contact pair.

by these authors for the case of smooth and convex but otherwise arbitrary profiles and monotonically increasing load, the stick-slip radius is invariant of the loading and profile geometry. Presently, it has been found at monotonic frictional indentation of rigid flat, spherical and flat and rounded indenters that the relative stick-slip radius was almost constant and never varied more than one element size.

3. Results and discussion

The effect of indenter elasticity on a contact induced stress state is investigated presently for the case of a steel indenter pressed into a glass halfspace. The elasticity parameters for the contact materials are given in Table 1, along with material parameters for the equivalent rigid-elastic contact pair. The interfacial friction coefficient, μ, is set to 0.1 as measured by Elaguine et al. [2006].

Numerical studies are performed for the case of flat and rounded contact profiles as shown in Figure 1. The relative radius of the flat part, b/a, is varied between 0 and 1 giving in the limits spherical and flat indenters respectively. The indenter height, l, is kept fixed being 7 times the maximum contact radii attained during simulations, $l \approx 7a_{\text{MAX}}$. The round-off radius of the rounded part is kept fixed at $R \approx 30a_{\text{MAX}}$. The validity of the Hertz theory assumption regarding the contact area being small as compared to indenter dimensions is then controlled by the ratio between indenter radius, w, and contact area radius, a. The analysis is performed presently for the cases of $1 \leq w/a \leq 50$, where the geometries with high w/a ratios are considered to be close to the Hertz theory, and the lower ratios represent an indenter with dimensions finite as compared to the contact size. The indenter shown in Figure 3 is used in simulations to represent a perfectly flat punch with $w/a > 1$; it consists of two cylinders the first one of radius a and length l, and the second one with radius $w - a$ and a bit shorter so it does not come in

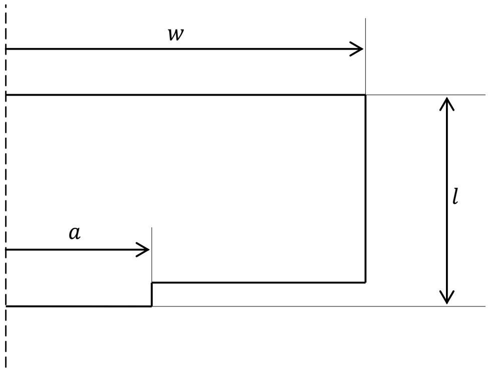

Figure 3. The flat indenter with $w \gg a$.

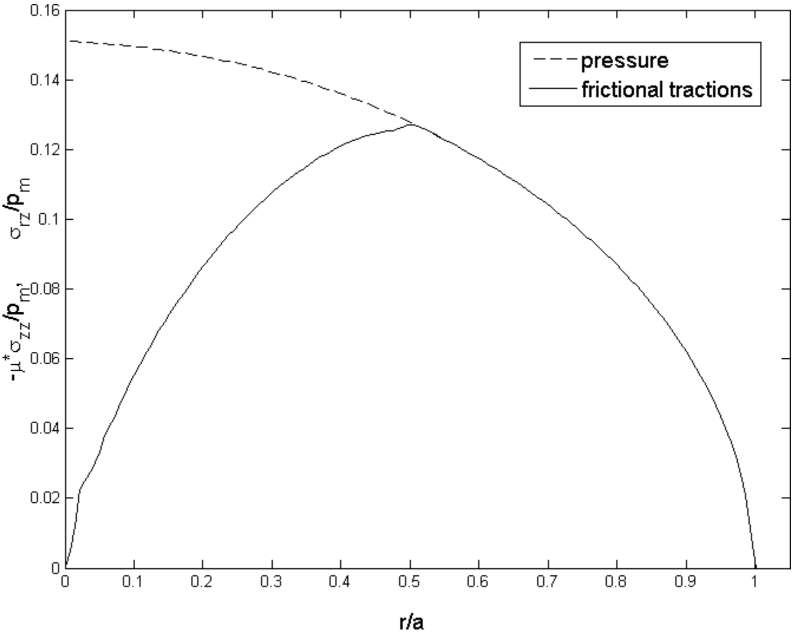

Figure 4. Normal and tangential tractions at spherical indentation ($w >> a$).

contact with the specimen. It has to be pointed out that in Figure 3 proportions are not kept for illustrative reasons, in the simulations the first cylinder had the length $l = 7a_{\mathrm{MAX}}$ and the second cylinder had the length of $l - 0.05a_{\mathrm{MAX}}$.

In all the simulations performed the load was applied in displacement control mode, by prescribing a uniform vertical displacement, δ, to the upper boundary of the indenter. All comparative studies have been performed at fixed $\delta \approx 0.02a_{\mathrm{MIN}}$ (chosen to be small compared to the contact radii in all the simulations). In the presentation below, results pertinent to spherical indentation are depicted in Figure 4, flat punch results are depicted in Figures 5–9 and in Figures 10–12 a comparison is made between the results for different indenter geometries. Contact features such as pressure distribution, tangential tractions, vertical and horizontal displacements, contact area and stick-slip radius are considered and pertinent results presented.

In Figure 4 then, the pressure and frictional traction distributions are shown, for the case of a spherical indenter ($b = 0$), $w/a > 50$, and elastic-elastic contact. The distributions are normalized with the mean pressure, $p_0 = P/(\pi a^2)$, and for illustrative purposes the pressure distribution is multiplied by the friction coefficient. Obviously, the region where the distributions coincide correspond to the slip region; see (5) and (6). The relative stick-slip radius in the present case was found to be $c/a = 0.5$, which is well within one element length from the 0.497 given by the analytical formula developed by Spence. It has been found that for the case of $w/a > 50$, normal and tangential tractions computed with the equivalent rigid elastic formulation differ less than 0.5% from the results obtained with the elastic-elastic model for all the contact geometries studied, i.e., $0 \leq b/a \leq 1$.

Furthermore, it has been shown by Storåkers and Elaguine [2005] that the relative stick-slip radius is independent of profile geometry provided that profiles are smooth and convex. Presently, in all the

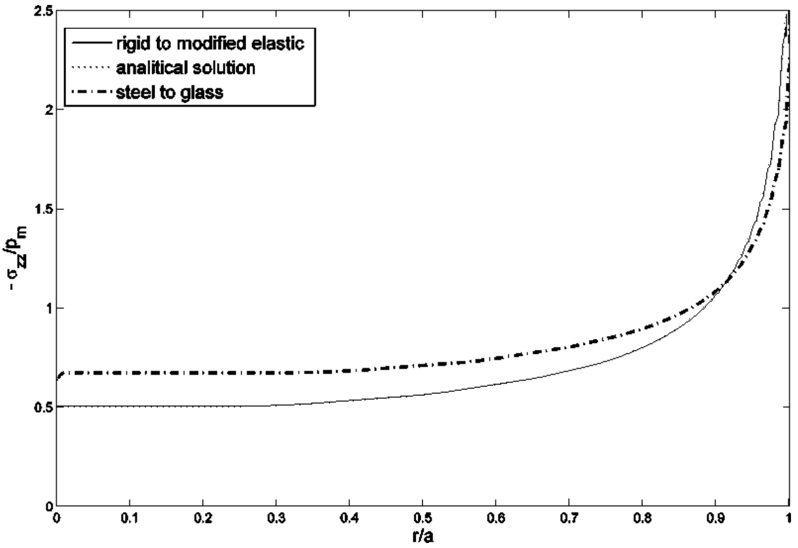

Figure 5. Pressure distribution at frictionless flat punch indentation ($w = a$).

simulations performed for the big indenters ($w/a > 50$), the stick-slip radius was found approximately constant and equal to 0.5 both for elastic-elastic and equivalent rigid-elastic formulations.

In Figure 5 normalized pressure distributions are shown for the frictionless flat punch indentation, ($b/a = w/a = 1$). Distributions obtained with elastic-elastic and equivalent rigid-elastic formulations are presented along with the analytical solution; see [Johnson 1985]. The figure shows that the pressure distribution obtained with a rigid indenter basically coincides with the analytical solution. The distribution corresponding to the steel to glass contact deviates however from the analytical and rigid elastic distribution; as one may observe in Figure 5 the pressure in the middle of the contact area is approximately 35% higher for the elastic-elastic as compared to the rigid-elastic case. Furthermore, at the vicinity of the contact boundary indenter elasticity results in somewhat lower pressure. This difference between the two sets of results is due to the fact that the steel indenter undergoes significant deformation under action of high pressure at the vicinity of the contact boundary and the resulting contact geometry deviates from the perfectly flat punch. This is shown in Figure 6, where the vertical displacements on the surface of the halfspace are presented normalized with maximum indentation depth. It may be seen that displacements induced in the contact area by a steel punch deviates from the one induced by a rigid punch by approximately 12% at the contact boundary. The simulations have also been performed with steel indenters having heights $l/a = 1$and 5, the shape of vertical surfaces displacements were found to be independent of height. However, in simulations of flat punch indentation performed at $w/a \gg 1$, the indenter elasticity was found to have a very minor effect on the pressure distribution and surface displacement profiles, resulting in approximately 1% variation from the rigid-modified elastic case. This indicates that the effect of local indenter deformations on the pressure and frictional tractions distributions is minute.

Regarding the results in Figures 5 and 6 for frictionless indentation, it is important to emphasize that the influence of friction on the pressure distribution, Figure 5 and the vertical surface displacements, Figure 6, was found presently to be very small. This has also been shown in several previous studies; see, for example, [[Hills and Sackfield 1987; Andersson 1996; Storåkers and Elaguine 2005]]. Consequently,

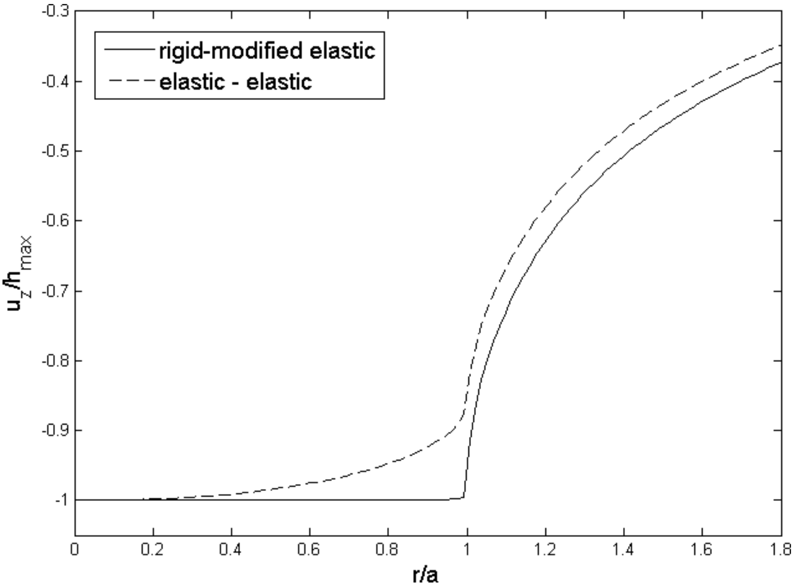

Figure 6. Vertical surface displacements at flat punch indentation, rigid-elastic vs elastic-elastic formulation.

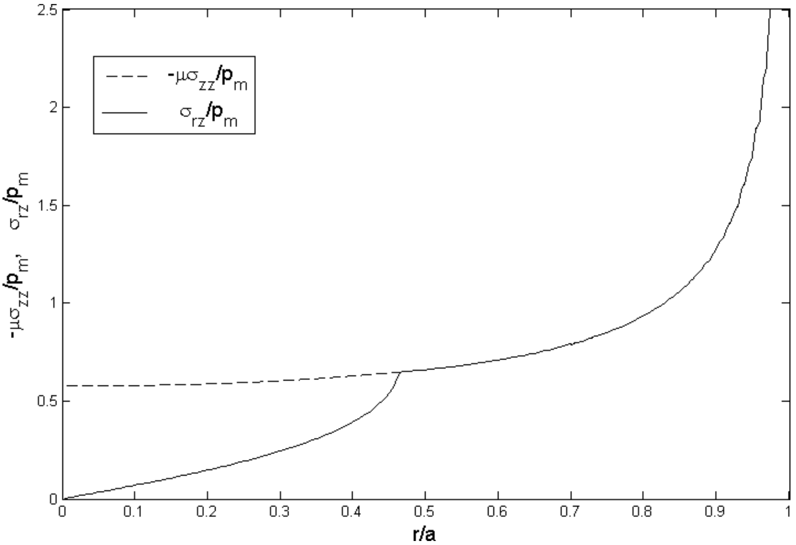

Figure 7. Normal and tangential tractions, flat punch indentation at finite friction, rigid-elastic contact.

the impact of the finite size of the elastic indenter on these quantities would be the same for frictionless and finite frictional cases.

Figures 7 and 8 examine frictional flat punch indentation with rigid-elastic and elastic-elastic solutions respectively. Normalized shear tractions are presented, along with normalized pressure distributions multiplied by friction coefficients. It may be observed in Figure 7 that the relative stick-slip radius for the rigid flat punch is approximately 0.5, equal to the one found for profiles with $w/a > 50$. However, as

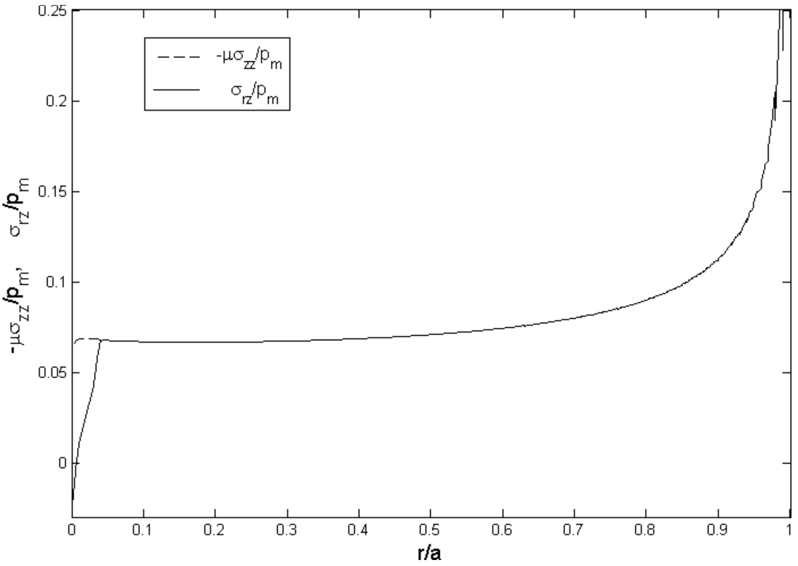

Figure 8. Normal and tangential tractions, flat punch indentation at finite friction, elastic-elastic contact.

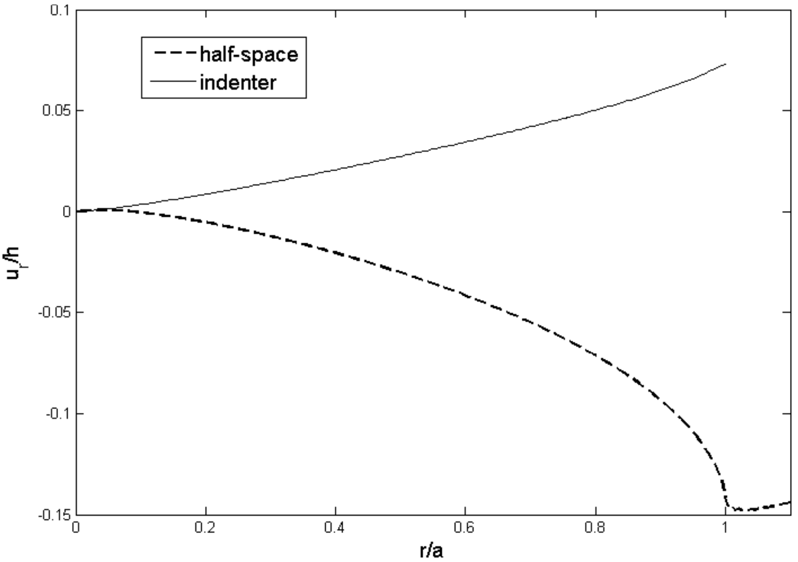

Figure 9. Horizontal surface displacements at frictional flat punch indentation.

shown in Figure 8, the relative stick-slip radius found at steel to glass contact is much smaller, approximately 0.04. In Figure 9 the horizontal displacements on the surfaces of the steel indenter and the glass halfspace are shown normalized with the depth of indentation. It may be seen that while the material in the glass specimen tend towards the center of the contact area, the steel indenter undergoes some elastic expansion with the material moving away from the axis of symmetry. This elastic expansion gives rise to additional shear tractions on the interface which result in a much smaller stick zone radius.

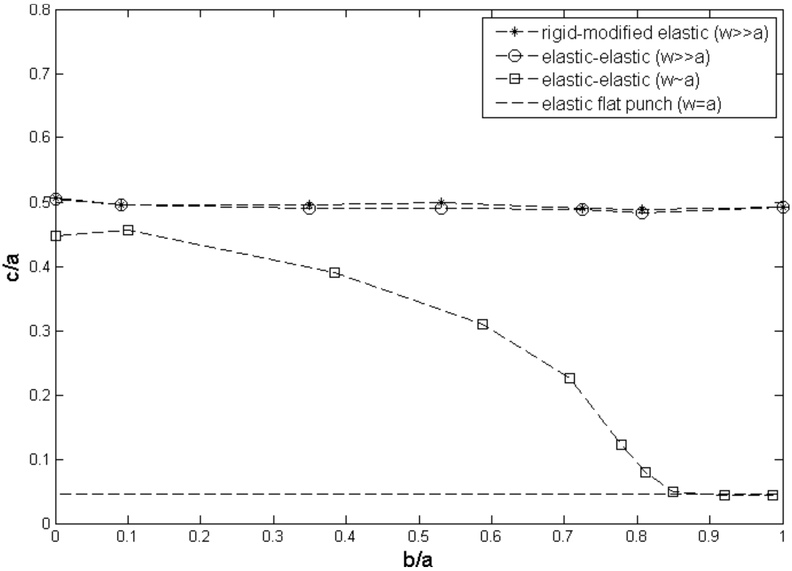

Figure 10. Relative stick-slip radii at flat and rounded contact.

As seen from the study of the limiting cases of $w/a > 50$ and $w/a = 1$ (Figures 5–9) the indenter elasticity may have a profound influence on the induced pressure and frictional tractions at dissimilar elastic contact. In order to examine this effect further the contacts between flat and rounded indenters, with a size comparable with the size of the contact area, have been studied. The indenter radius has been set to three times the contact area at rigid spherical indentation $w = a_{\mathrm{MAX}}$. The radius of the flat part, b, has been varied while the indenter radius was kept constant.

In Figure 10 the relative stick-slip radii, c/a, obtained at elastic-elastic indentation with a finite flat and rounded indenter are shown as a function of b/a. Also in Figure 10 the stick-slip radii are presented for flat and rounded indenters with $w \gg a$ as well as for the elastic-elastic flat punch indentation at $w = a$. As one may observe in Figure 10 the stick-slip radii at $w \gg a$ are invariant of contact geometry and of contact formulation and are approximately equal to $0.5a$. The same stick-slip radii have been found at rigid-modified elastic contact for the flat and rounded indenter with $w = 3a_{\mathrm{rigid\_sphere}}$, results are not shown in Figure 10 for brevity. At elastic-elastic contact however this invariance is lost. It may be seen that for finite indenters with shapes close to spherical ($b/a <= 0.1$) the stick-slip radius deviates approximately 10% from the rigid-elasic case. As b/a increases the stick-slip radius decreases and for $b/a > 0.8$ it is equal to the one at elastic-elastic flat punch indentation.

The results presented in Figure 10 indicate the existence of the indenter boundary effect at indentation of a flat and rounded punch with dimensions comparable to the contact radius. The b/a variation was achieved presently by varying the size of the flat part with respect to the indenter size, i.e. b/a varying between 0 and 1 corresponds to b/w varying between 0 and 1 and w/a varying from 3 to 1.

In Figure 11 the contact area radii at spherical and flat and rounded elastic-elastic contacts are shown as function of w/a. Results are normalized with the corresponding contact area radii obtained at equivalent rigid-elastic contact. As it may be observed in Figure 11 the contact radii obtained with elastic-elastic and rigid-elastic formulations coincide for at least $w > 10a$. At relative indenter sizes $w < 10a$ the contact

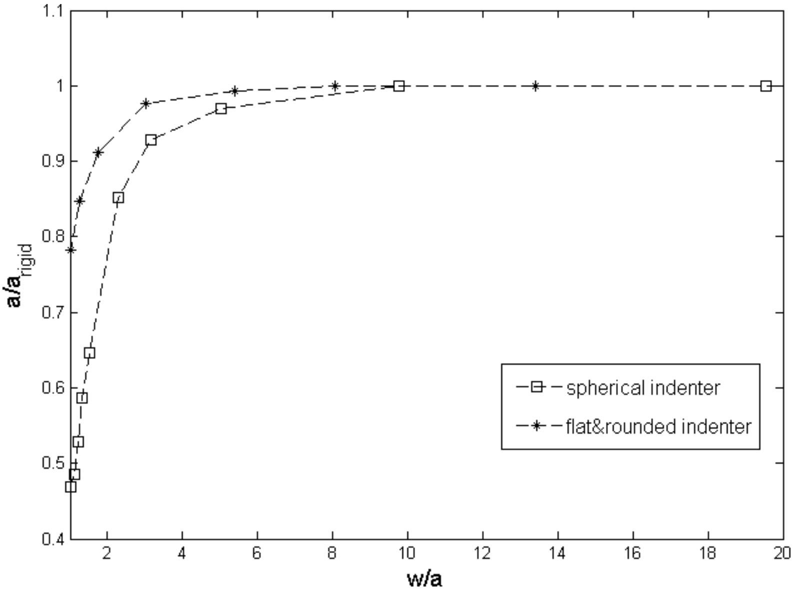

Figure 11. Contact area at elastic-elastic contact spherical and flat and rounded indenters.

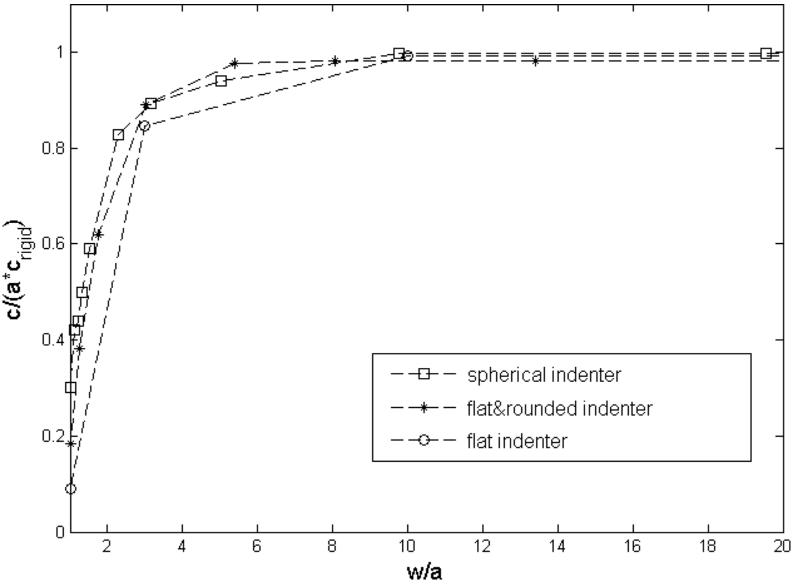

Figure 12. Stick-slip radii at elastic-elastic contact as a function of indenter size relative to the contact area.

area is somewhat smaller than the one at rigid-elastic contact, the amount of reduction depending on the contact geometry. The difference is however less than 10% for $w > 4a$ in the spherical case and for $w > 2a$ for the flat and rounded case. For the flat and rounded contact the radius of the flat part was taken to be equal to the contact area at rigid spherical indentation $b = a_{\text{rigid\_sphere}}$, the relative size of the flat part, b/a, was varying between 0.54 for $w >= 6a$ and 0.7 for $w = a$. The reason behind the sharp decrease of the contact area at small values on w/a is the fact that the effect of indenter stiffness is not adequately accounted for by the reduced modulus of the halfspace. The particular indenter shape investigated has $l/a = 20$, and at small w/a the indenter deforms significantly more than predicted by Hertz contact theory.

In Figure 12 the relative stick-slip radii at spherical, flat and flat and rounded elastic-elastic contact are shown as function of w/a. As in Figure 11 results are normalized with the ones obtained at rigid elastic contact. One may observe that indenter elasticity doesn't influence the stick-slip radius for $w > 10a$, at $w/a < 10$ the stick region starts to decrease and also becomes geometry dependent.

It has to be emphasized that the results depicted in Figures 10–12 relate to the effect that the global indenter stress state has on the pressure and frictional tractions distributions. Therefore, as the self-similarity is lost here, the results presented are strictly valid only for the particular geometries investigated; altering the indenter height, elastic properties and/or load application mode would alter the effect. Rodriguez et al. [2011] evaluated the effect of the elastic indenter deformation on the instrumented indentation measurements. They preformed FE simulations of diamond sphere frictionless indentation into different elastic materials at the following contact parameters $w/a \approx 3.2$, $l/a \approx 3.2$, $R/\delta_{\max} = 10$, $\delta_{\max}$ being the mutual approach distance, and a is the contact radius estimated based on Hertz theory. Analogous to the present study, they ran comparative analysis with elastic-elastic and rigid-modified elastic contact simulations. They reported that indenter elasticity taken into account results in a slight increase of the contact radius as compared to the rigid-elastic solution; in particular, for the case of $E_{\text{specimen}}/E_{\text{indenter}} = 0.39$ they found 2.1% increase of the contact radius. As it may be seen in Figure 11, an approximately 7% reduction in the contact area radius is observed presently when indenter elasticity is taken into account at $w/a = 3.2$. The discrepancy between present results and the ones Rodriguez et al. is due to the fact that the rest of contact parameters are different; present simulations are performed at $E_{\text{specimen}}/E_{\text{indenter}} = 0.39$ and $l/a \approx 20$, $R/\delta_{\max} = 1e3$. In order to check the effect of indenter height on the contact radius the analysis has been performed presently at $l/a = w/a \approx 3$ keeping the rest of parameters as in other simulations and it has been found that the contact radius increases approximately 1.5% in this case due to indenter elasticity. This is close to the 2.1% found by Rodriguez et al., with the remaining difference most likely due to differences in curvature radii and material properties used.

Results presented in Figures 11 and 12 indicate that indenter boundaries significantly affect the distributions of pressure and frictional tractions only when w is less than say $4a$, the exact range depending of course on indenter geometry. In case of the contact geometries close to spherical ($b \to 0$) the loads required to produce $w < 4a$ will induce significant plastic deformations or fracture in most of the practically interesting contact pairs.

Contact at flat and rounded profiles with a flat part radius comparable with the indenter radius may result in $w/a \approx 1$ even at moderate loads. Pau et al. [2006] used ultrasound based technique to examine the contact geometry at indentation with a steel flat indenter with rounded corners into a steel plate. The indenter used had a radius of 10 mm and the radius of the flat part was 2.5 mm. The reported measurements were performed at a load level which resulted in $a \approx 4$ mm, $b/a \approx 0.63$ and thus in $w/a \approx 2.5$. As shown in Figure 11 the contact area for the flat and rounded indenter at $w/a = 2.5$, $b/a = 0.57$ is approximately 5% smaller as compared to the one obtained at rigid-modified elastic contact. The relative stick-slip radius for this geometry is shown in Figure 12 and is approximately 78% of the one found at rigid-modified elastic contact. At smaller loads giving $b/a \approx 1$, the indenter geometry used

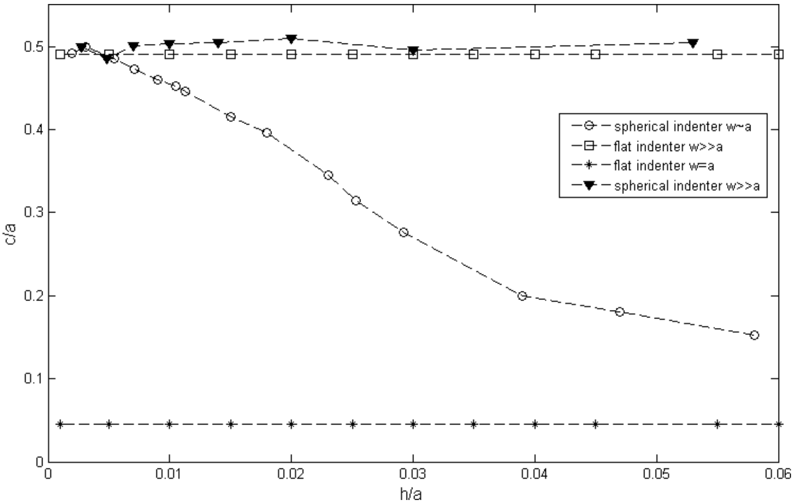

Figure 13. Stick-slip radii at elastic-elastic contact as a function of relative indentation depth.

by Pau et al. [2006] would result in $w/a \approx 4$. In this case, based on the results presented in Figure 11 the effect of the indenter boundaries on the contact area will be very minor. The relative stick-slip radius will be reduced by approximately 5% as compared to the rigid-modified elastic formulation.

As it has been pointed by Chaudhri in relation to the postprocessing of nanoindentation tests data (see also Lim and Chaudhri [2003]), the Boussinesq [1885] and Sneddon [1965] solutions are strictly valid only for rigid indenters. Results presented in Figures 5–8 substantiate this observation for the case of a flat cylindrical indenter $w = a$ — the rigid-modified elastic formulation is not capable of properly accounting for the elastic deformation of the indenter. However, based on the results in Figure 12 and the related discussion it appears to be possible to use the rigid-modified elastic formulation to evaluate the frictional indentation with a elastic flat-ended punch, provided that it's geometry results in $w/a \gg 1$.

In Figure 13, the stick-slip radii found at elastic-elastic contact are shown as a function of the relative indentation depth. Results in Figure 13 are given for flat indenters with $w \gg a$ and $w = a$, as well as for spherical indenters with $w \gg a$, and $w \sim a$. In the case of a spherical indenter with finite dimensions the relative indenter radius, w/a, varies with increasing depth of indentation between 11.72 and 1.05. As one may observe in Figure 13, the relative stick-slip radii for flat indenters and for the spherical indenter with $w \gg a$ remain approximately constant at relative indentation depths varying between $2e{-}3$ and $6e{-}2$. In case of a spherical indenter with $w \sim a$ the stick-slip radius decreases from $0.5a$ to $0.15a$, which agrees well with approximately the 70% decrease in stick-slip radius depicted in Figure 12.

4. Concluding remarks

The influence of the boundary effects on the frictional contact of dissimilar elastic solids has been examined presently for the case of flat and rounded contact profiles. In particular, the effect of relative indenter size, w/a on the pressure and tangential tractions distribution has been evaluated based on the comparison between elastic-elastic and rigid-modified elastic contact formulations. In general, it has been found that the results obtained with these two formulations start to deviate significantly at $w/a < 4$. This indicates that the approximation given in (7) does not account properly for the indenter elasticity at small w/a, and the contact tractions distributions depend than on the global stress state in the indenter. Thus, solution of the coupled problem taking into account the indenter geometry and constraints is required in order to accurately describe the contact between specimen and the indenter with the dimensions close to the contact area radius.

The practically important class of contacts with $w/a \approx 1$ are the complete or nearly complete contacts, i.e. flat indenters with rounded corners and $b/a \approx 1$. In these situations indenter boundary effects should be accounted for in order to obtain an accurate description of contact interactions. One practically important case where this effect is of significance is indentation testing with flat punch [Chaudhri 2001]. At the same time most of the practically important contacts at profile geometries close to spherical $b/a << 1$ will have the indenter dimensions much bigger as compared to the contact radius as long as the load is relatively small and linear elasticity prevails. The boundary effects will however affect contact conditions for these geometries in case of multiple contacts located close to each other as may be the case in micromechanical simulations with discrete element method.

In the present study, the effect of local elastic deformations of the indenter on the normal and tangential tractions was found to be minute for all the geometries investigated. Thus, it may furthermore be concluded that the computational procedure developed by Storåkers and Elaguine [2005] based on self-similarity can be used to accurately evaluate frictional dissimilar elastic contact at flat and rounded contact profiles at least for $w/a > 4$.

References

[Andersson 1996] M. Andersson, "Stress distribution and crack initiation for an elastic contact including friction", *Int. J. Solids Struct.* **33**:25 (1996), 3673–3696.

[Argatov 2002] I. I. Argatov, "The pressure of a punch with a rounded edge on an elastic half-space", *J. Appl. Math. Mech.* **66**:4 (2002), 637–643.

[Argatov 2010] I. I. Argatov, "Frictionless and adhesive nanoindentation: asymptotic modeling of size effects", *Mech. Mater.* **42**:8 (2010), 807–815.

[Banerjee et al. 2009] N. Banerjee, D. A. Hills, and D. Dini, "The derivation and application of a semi-infinite flat and rounded asymptotic frictionless contact", *Int. J. Mech. Sci.* **51**:9–10 (2009), 662–666.

[Biwa and Storåkers 1995] S. Biwa and B. Storåkers, "An analysis of fully plastic Brinell indentation", *J. Mech. Phys. Solids* **43**:8 (1995), 1303–1333.

[Borodich 1993] F. M. Borodich, "The Hertz frictional contact between nonlinear elastic anisotropic bodies (the similarity approach)", *Int. J. Solids Struct.* **30**:11 (1993), 1513–1526.

[Borodich and Galanov 2002] F. M. Borodich and B. A. Galanov, "Self-similar problems of elastic contact for non-convex punches", *J. Mech. Phys. Solids* **50**:11 (2002), 2441–2461.

[Borodich and Keer 2004] F. M. Borodich and L. M. Keer, "Evaluation of elastic modulus of materials by adhesive (no-slip) nano-indentation", *Proc. R. Soc. Lond. A* **460**:2042 (2004), 507–514.

[Boussinesq 1885] J. Boussinesq, *Applications des potentiels à l'étude de l'équilibre et du mouvement des solides élastiques*, Gauthier-Villars, Paris, 1885.

[Carlsson et al. 2000] S. Carlsson, S. Biwa, and P.-L. Larsson, "On frictional effects at inelastic contact between spherical bodies", *Int. J. Mech. Sci.* **42**:1 (2000), 107–128.

[Chaudhri 2001] M. M. Chaudhri, "A note on a common mistake in the analysis of nanoindentation data", *J. Mater. Res.* **16**:2 (2001), 336–339.

[Ciavarella 1999] M. Ciavarella, "Indentation by nominally flat or conical indenters with rounded corners", *Int. J. Solids Struct.* **36**:27 (1999), 4149–4181.

[Ciavarella and Hills 1999] M. Ciavarella and D. A. Hills, "The influence of the indenter tip-radius on indentation testing of brittle materials", *J. Eur. Ceram. Soc.* **19**:2 (1999), 239–245.

[Cundall and Hart 1992] P. A. Cundall and R. D. Hart, "Numerical modeling of discontinua", *Eng. Computation.* **9**:2 (1992), 101–113.

[Elaguine et al. 2006] D. Elaguine, M.-A. Brudieu, and B. Storåkers, "Hertzian fracture at unloading", *J. Mech. Phys. Solids* **54**:11 (2006), 2453–2473.

[Fu 2006] G. H. Fu, "Effects of tip rounding on the fundamental relations used in the analysis of nanoindentation data", *Mater. Lett.* **60**:29–30 (2006), 3855–3856.

[Fu and Cao 2009] G. H. Fu and T. S. Cao, "On the fundamental relation used in nanoindentation with piecewisely defined indenters", *Mater. Sci. Eng. A* **513-514** (2009), 276–278.

[Harsono et al. 2011] E. Harsono, S. Swaddiwudhipong, Z. S. Liu, and L. Shen, "Numerical and experimental indentation tests considering size effects", *Int. J. Solids Struct.* **48**:6 (2011), 972–978.

[Hertz 1882] H. Hertz, "Ueber die Berührung fester elastischer Körper", *J. Reine Angew. Math.* **92** (1882), 156–171.

[Heyliger and McMeeking 2001] P. R. Heyliger and R. M. McMeeking, "Cold plastic compaction of powders by a network model", *J. Mech. Phys. Solids* **49**:9 (2001), 2031–2054.

[Hill and Storåkers 1990] R. Hill and B. Storåkers, "A concise treatment of axisymmetric indentation in elasticity", pp. 199–210 in *Elasticity: mathematical methods and applications*, edited by G. Eason and R. W. Ogden, Ellis Horwood, Chichester, 1990.

[Hill et al. 1989] R. Hill, B. Storåkers, and A. B. Zdunek, "A theoretical study of the Brinell hardness test", *Proc. R. Soc. Lond. A* **423**:1865 (1989), 301–330.

[Hills and Dini 2006] D. A. Hills and D. Dini, "A new method for the quantification of nucleation of fretting fatigue cracks using asymptotic contact solutions", *Tribol. Int.* **39**:10 (2006), 1114–1122.

[Hills and Sackfield 1987] D. A. Hills and A. Sackfield, "The stress field induced by normal contact between dissimilar spheres", *J. Appl. Mech.* (*ASME*) **54**:1 (1987), 8–14.

[Hills et al. 1993] D. A. Hills, D. Nowell, and A. Sackfield, *Mechanics of elastic contacts*, Butterworth-Heinemann, Oxford, 1993.

[Huang et al. 2006] Y. Huang, F. Zhang, K. C. Hwang, W. D. Nix, G. M. Pharr, and G. Feng, "A model of size effects in nano-indentation", *J. Mech. Phys. Solids* **54**:8 (2006), 1668–1686.

[Jaffar 2002] M. J. Jaffar, "Frictionless contact between an elastic layer on a rigid base and a circular flat-ended punch with rounded edge or a conical punch with rounded tip", *Int. J. Mech. Sci.* **44**:3 (2002), 545–560.

[Jelagin and Larsson 2008a] D. Jelagin and P.-L. Larsson, "On indentation and initiation of fracture in glass", *Int. J. Solids Struct.* **45**:10 (2008), 2993–3008.

[Jelagin and Larsson 2008b] D. Jelagin and P.-L. Larsson, "Hertzian fracture at finite friction: a parametric study", *Wear* **265**:5–6 (2008), 840–848.

[Johnson 1985] K. L. Johnson, *Contact mechanics*, Cambridge University Press, Cambridge, 1985.

[Larsson and Storåkers 2002] J. Larsson and B. Storåkers, "On oblique contact of creeping solids", *J. Mech. Phys. Solids* **50**:10 (2002), 2029–2055.

[Lim and Chaudhri 2003] Y. Y. Lim and M. M. Chaudhri, "Experimental investigations of the normal loading of elastic spherical and conical indenters on to elastic flats", *Philos. Mag.* **83**:30 (2003), 3427–3462.

[Martin and Bouvard 2003] C. L. Martin and D. Bouvard, "Study of the cold compaction of composite powders by the discrete element method", *Acta Mater.* **51**:2 (2003), 373–386.

[Martin et al. 2003] C. L. Martin, D. Bouvard, and S. Shima, "Study of particle rearrangement during powder compaction by the discrete element method", *J. Mech. Phys. Solids* **51**:4 (2003), 667–693.

[Matsuoka and Yamamoto 1993] H. Matsuoka and S. Yamamoto, “A microscopic study on shear mechanism of granular materials by DEM and experiments”, pp. 155–160 in *Powders and grains 93* (Birmingham, 1993), edited by C. Thornton, Balkema, Rotterdam, 1993.

[Mossakovskii 1963] V. I. Mossakovskii, “Compression of elastic bodies under conditions of adhesion (axisymmetric case)”, *Prikl. Mat. Mekh.* **27**:3 (1963), 418–427. In Russian; translated in *J. Appl. Math. Mech.* **27**:3 (1963), 630–643.

[Nowell et al. 2006] D. Nowell, D. Dini, and D. A. Hills, “Recent developments in the understanding of fretting fatigue”, *Eng. Fract. Mech.* **73**:2 (2006), 207–222.

[Pau et al. 2006] M. Pau, B. Leban, and A. Baldi, “Experimental analysis of contact for the indentation of a flat rounded punch”, *Int. J. Solids Struct.* **43**:25–26 (2006), 7959–7965.

[Rodriguez et al. 2011] S. A. Rodriguez, J. Alcala, and R. M. Souza, “Effects of elastic indenter deformation on spherical instrumented indentation tests: the reduced elastic modulus”, *Philos. Mag.* **91**:7–9 (2011), 1370–1386.

[Skrinjar and Larsson 2004] O. Skrinjar and P.-L. Larsson, “On discrete element modelling of compaction of powders with size ratio”, *Comput. Mater. Sci.* **31**:1–2 (2004), 131–146.

[Sneddon 1965] I. Sneddon, “The relation between load and penetration in the axisymmetric Boussinesq problem for a punch of arbitrary profile.”, *Int. J. Eng. Sci.* **3** (1965), 47–57.

[Spence 1968] D. A. Spence, “Self similar solutions to adhesive contact problems with incremental loading”, *Proc. R. Soc. Lond. A* **305**:1480 (1968), 55–80.

[Spence 1975a] D. A. Spence, “The Hertz contact problem with finite friction”, *J. Elasticity* **5**:3–4 (1975), 297–319.

[Spence 1975b] D. A. Spence, “Similarity considerations for contact between dissimilar elastic bodies”, pp. 67–76 in *The mechanics of the contact between deformable bodies: proceedings of the IUTAM Symposium on Mechanics of Contact* (Enschede, 1974), edited by A. D. de Pater and J. J. Kalker, Delft University Press, Delft, 1975.

[Storåkers and Elaguine 2005] B. Storåkers and D. Elaguine, “Hertz contact at finite friction and arbitrary profiles”, *J. Mech. Phys. Solids* **53**:6 (2005), 1422–1447.

[Storåkers and Larsson 1994] B. Storåkers and P.-L. Larsson, “On Brinell and Boussinesq indentation of creeping solids”, *J. Mech. Phys. Solids* **42**:2 (1994), 307–332.

[Storåkers et al. 1997] B. Storåkers, S. Biwa, and P.-L. Larsson, “Similarity analysis of inelastic contact”, *Int. J. Solids Struct.* **34**:24 (1997), 3061–3083.

[Thornton and Antony 1998] C. Thornton and S. J. Antony, “Quasi-static deformation of particulate media”, *Phil. Trans. R. Soc. A* **356**:1747 (1998), 2763–2782.

[Thornton and Lanier 1997] C. Thornton and J. Lanier, “Uniaxial compression of granular media: numerical simulations and physical experiment”, pp. 223–226 in *Powders and grains 97* (Durham, NC, 1997), edited by R. P. Behringer and J. T. Jenkins, Balkema, Rotterdam, 1997.

Received 24 May 2011. Revised 4 Jan 2012. Accepted 9 Jan 2012.

DENIS JELAGIN: `denis.jelagin@abe.kth.se`
Division of Highway and Railway Engineering, Royal Institute of Technology, SE-10044, Stockholm, Sweden

PER-LENNART LARSSON: `pelle@hallf.kth.se`
Department of Solid Mechanics, Royal Institute of Technology, SE-10044, Stockholm, Sweden

JOURNAL OF MECHANICS OF MATERIALS AND STRUCTURES
Vol. 7, No. 2, 2012

REFLECTION OF P AND SV WAVES FROM THE FREE SURFACE OF A TWO-TEMPERATURE THERMOELASTIC SOLID HALF-SPACE

BALJEET SINGH AND KIRAN BALA

The present paper is concerned with the propagation of plane waves in an isotropic generalized thermoelastic solid half-space with two temperatures. The governing equations are modified in the context of the Lord–Shulman theory of generalized thermoelasticity and are solved to show the existence of three plane waves, namely, P, thermal, and SV waves in the x-z plane. The reflection of the P and SV waves from a thermally insulated free surface is studied to obtain the reflection coefficients in closed form. For numerical computations of the speeds and reflection coefficients, a particular material is chosen. The speeds of the plane waves are shown graphically against the two-temperature parameter. The reflection coefficients are also shown graphically against the angle of incidence for different values of the two-temperature parameter.

1. Introduction

Lord and Shulman [1967] and Green and Lindsay [1972] extended the classical dynamical coupled theory of thermoelasticity to generalized thermoelasticity theories. Their theories treat heat propagation as a wave phenomenon rather than a diffusion phenomenon and predict a finite speed of heat propagation. Ignaczak and Ostoja-Starzewski [2010] explained these theories in detail. The representative theories in the range of generalized thermoelasticity are reviewed in [Hetnarski and Ignaczak 1999]. Wave propagation in thermoelasticity has many applications in various engineering fields. Several problems in wave propagation in coupled or generalized thermoelasticity have been studied by various researchers [Deresiewicz 1960; Sinha and Sinha 1974; Sinha and Elsibai 1996; 1997; Sharma et al. 2003; Othman and Song 2007; Singh 2008; 2010].

Gurtin and Williams [1966; 1967] suggested a second law of thermodynamics for continuous bodies in which the entropy due to heat conduction was governed by one temperature, that of the heat supply by another. Based on this suggestion, Chen and Gurtin [1968] and Chen et al. [1968; 1969] formulated a theory of thermoelasticity which depends on two distinct temperatures, the conductive temperature Φ and the thermodynamic temperature T. Two-temperature theory involves a material parameter $a^* > 0$. The limit $a^* \to 0$ implies that $\Phi \to T$ and hence classical theory can be recovered from two-temperature theory. The two-temperature model has been widely used to predict electron and phonon temperature distributions in ultrashort laser processing of metals.

Warren and Chen [1973] stated that these two temperatures can be equal in time-dependent problems under certain conditions, whereas Φ and T are generally different in particular problems involving wave propagation. Following [Boley and Tolins 1962], they studied wave propagation in the two-temperature theory of coupled thermoelasticity. They showed that the two temperatures T and Φ and the strain are

---

Keywords: two-temperature parameter, generalized thermoelasticity, plane waves, reflection coefficients.

represented in the form of a traveling wave plus a response, which occurs instantaneously throughout the body. Puri and Jordan [2006] discussed the propagation of harmonic plane waves in two-temperature theory. Quintanilla and Jordan [2009] presented exact solutions of two initial-boundary value problems in the two-temperature theory with dual-phase-lag delay.

Youssef [2006] formulated a theory of two-temperature generalized thermoelasticity. Kumar and Mukhopadhyay [2010] extended the work of Puri and Jordan [2006] in the context of the linear theory of two-temperature generalized thermoelasticity formulated in [Youssef 2006]. Magaña and Quintanilla [2009] studied the uniqueness and growth of solutions in two-temperature generalized thermoelastic theories. Youssef [2011] also presented a theory of two-temperature thermoelasticity without energy dissipation. Ezzat and El-Karamany [2011] developed a two-temperature theory in generalized magnetothermoelasticity with two relaxation times.

In the present paper, we have applied the theory of [Youssef 2006] to the study of wave propagation in an isotropic two-temperature thermoelastic solid. The expressions for the speeds of plane waves are obtained. The required boundary conditions at a thermally insulated stress-free surface are satisfied by the appropriate solutions in an isotropic thermoelastic solid half-space to obtain the reflection coefficients in closed form for a particular incident wave. The speeds and reflection coefficients of plane waves are computed numerically for a particular model of the half-space to observe the effect of the two-temperature parameter.

2. Basic equations

Following [Youssef 2006], the governing equations for two-temperature anisotropic generalized thermoelasticity with one relaxation parameter are:

- The stress-strain-temperature relations:

$$\sigma_{ij} = c_{ijkl}e_{kl} - \gamma_{ij}(T - \Phi_0), \tag{1}$$

- The displacement-strain relation:

$$e_{ij} = \tfrac{1}{2}(u_{i,j} + u_{j,i}), \tag{2}$$

- The equation of motion:

$$\rho\ddot{u} = \sigma_{ji,j} + \rho F_i, \tag{3}$$

- The energy equation:

$$-q_{i,i} = \rho T_0 \dot{S}, \tag{4}$$

- The modified Fourier's law:

$$-K_{ij}\phi_{,j} = q_i + \tau_0 \dot{q}_i, \tag{5}$$

- The entropy-strain-temperature relation:

$$\rho S = \frac{\rho c_E}{T_0}\theta + \gamma_{ij}e_{ij}. \tag{6}$$

Here, γ_{ij} are the coupling parameters, T is the mechanical temperature, $\Phi_0 = T_0$ is the reference temperature, $\theta = T - T_0$ with $|\theta/T_0| \ll 1$, σ_{ij} is the stress tensor, e_{kl} is the strain tensor, c_{ijkl} is the tensor of elastic constants, ρ is the mass density, q_i is the heat conduction vector, K_{ij} is the thermal conductivity tensor, c_E is the specific heat at constant strain, u_i are the components of the displacement vector, S is the entropy per unit mass, τ_0 is the thermal relaxation time (which will ensure that the heat conduction equation will predict finite speeds of heat propagation), and ϕ is the conductive temperature satisfying the relation

$$\Phi - T = a^* \Phi_{,ii}, \tag{7}$$

where $a^* > 0$ is the two-temperature parameter.

3. Formulation and solution of the problem

We consider a homogeneous and isotropic thermoelastic medium of infinite extent, with a Cartesian coordinate system (x, y, z), which is previously at a uniform temperature. The origin is taken on the plane surface and the z-axis is taken normally into the medium ($z \geq 0$). The surface $z = 0$ is assumed stress-free and thermally insulated. The present study is restricted to the plane strain parallel to the x-z plane, with the displacement vector $\mathbf{u} = (u_1, 0, u_3)$. With the help of (1)–(3), we obtain the following two components of the equation of motion:

$$(\lambda + 2\mu)u_{1,11} + (\lambda + \mu)u_{3,13} + \mu u_{1,33} - \gamma\theta_{,1} = \rho\ddot{u}_1, \tag{8}$$

$$(\lambda + 2\mu)u_{3,33} + (\lambda + \mu)u_{1,13} + \mu u_{3,11} - \gamma\theta_{,3} = \rho\ddot{u}_3. \tag{9}$$

Equations (4)–(6) lead to the following heat conduction equation:

$$K(\Phi_{,11} + \Phi_{,33}) = \rho c_E(\dot{\theta} + \tau_0\ddot{\theta}) + \gamma T_0(\dot{u}_{1,1} + \tau_0\ddot{u}_{1,1}) + \gamma T_0(\dot{u}_{3,3} + \tau_0\ddot{u}_{3,3}), \tag{10}$$

and (7) becomes

$$\Phi - T = a^*(\Phi_{,11} + \Phi_{,33}). \tag{11}$$

The displacement components u_1 and u_3 are written in terms of potentials q and ψ as

$$u_1 = \frac{\partial q}{\partial x} - \frac{\partial \psi}{\partial z}, \quad u_3 = \frac{\partial q}{\partial z} + \frac{\partial \psi}{\partial x}. \tag{12}$$

Using (12) in (8)–(11), we obtain

$$(\lambda + 2\mu)\left(\frac{\partial^2 q}{\partial x^2} + \frac{\partial^2 q}{\partial z^2}\right) - \gamma\left[\Phi - a^*\left(\frac{\partial^2 \Phi}{\partial x^2} + \frac{\partial^2 \Phi}{\partial z^2}\right)\right] = \rho\frac{\partial^2 q}{\partial t^2}, \tag{13}$$

$$\begin{aligned} K(\Phi_{,11} + \Phi_{,33}) = \rho c_E\left(\frac{\partial \Phi}{\partial t} + \tau_0\frac{\partial^2 \Phi}{\partial t^2}\right) - a^*\rho c_E\left(1 + \tau_0\frac{\partial}{\partial t}\right)\frac{\partial}{\partial t}\left(\frac{\partial^2 \Phi}{\partial x^2} + \frac{\partial^2 \Phi}{\partial z^2}\right) \\ + \gamma T_0\left(1 + \tau_0\frac{\partial}{\partial t}\right)\frac{\partial}{\partial t}\left(\frac{\partial^2 q}{\partial x^2} + \frac{\partial^2 q}{\partial z^2}\right), \end{aligned} \tag{14}$$

$$\mu\left(\frac{\partial^2 \psi}{\partial x^2} + \frac{\partial^2 \psi}{\partial z^2}\right) = \rho\frac{\partial^2 \psi}{\partial t^2}. \tag{15}$$

Here (15) is uncoupled, whereas (13) and (14) are coupled in q and Φ. Solutions (13)–(15) are now sought in the form of a harmonic traveling wave:

$$(q, \Phi, \psi) = (A, B, C) \exp(ik(x \sin\theta + z \cos\theta - vt)), \tag{16}$$

in which v is the phase speed, k is the wave number, and $(\sin\theta, \cos\theta)$ denotes the projection of the wave normal onto the x-z plane. Inserting (16) into (13)–(15), we obtain the following formulae for the speeds of the plane waves:

$$v_1 = \sqrt{\frac{1}{2\rho}\Big[\{(K_a + \epsilon) + (\lambda + 2\mu)\} + \sqrt{(K_a + \epsilon)^2 + (\lambda + 2\mu)^2 - 2(K_a - \epsilon)(\lambda + 2\mu)}\,\Big]}, \tag{17}$$

$$v_2 = \sqrt{\frac{1}{2\rho}\Big[\{(K_a + \epsilon) + (\lambda + 2\mu)\} - \sqrt{(K_a + \epsilon)^2 + (\lambda + 2\mu)^2 - 2(K_a - \epsilon)(\lambda + 2\mu)}\,\Big]}, \tag{18}$$

$$v_3 = \sqrt{\frac{\mu}{\rho}}, \tag{19}$$

where $\epsilon = (\gamma^2 T_0)/(\rho c_E)$ is the thermocoupling coefficient and $K_a = K/(c_E \tau^*(1 + a^* k^2))$, with $\tau^* = \tau_0 + i/\omega$, $\omega = kv$. The speeds v_1, v_2, and v_3 correspond to the P, thermal, and SV waves, respectively. From (17)–(19), it is clear that the speeds of the modified P and thermal waves are functions of the two-temperature parameter a^*. The speed of the SV wave is not affected by a^*.

If we neglect the thermal parameters (that is, $K_a = 0$, $\epsilon = 0$), the speed v_1 reduces to $\sqrt{(\lambda + 2\mu)/\rho}$, the speed of a P wave in an elastic solid. The thermal wave will disappear.

4. Boundary conditions

Let us now consider an incident P or SV wave. The boundary conditions at the stress-free thermally insulated surface $z = 0$ are satisfied if the incident P or SV wave gives rise to a reflected shear (SV) and two reflected longitudinal waves (P and thermal). The required boundary conditions at the free surface $z = 0$ are:

- Vanishing of the normal stress component:

$$\sigma_{zz} = 0, \tag{20}$$

- Vanishing of the tangential stress component:

$$\sigma_{zx} = 0, \tag{21}$$

- Vanishing of the normal heat flux component:

$$\frac{\partial \Phi}{\partial z} = 0, \tag{22}$$

where

$$\sigma_{zz} = \lambda\Big(\frac{\partial^2 q}{\partial x^2} + \frac{\partial^2 q}{\partial z^2}\Big) + 2\mu\Big(\frac{\partial^2 \psi}{\partial x \partial z}\Big) + 2\mu\frac{\partial^2 q}{\partial z^2} - \gamma\Big[\Phi - a^*\Big(\frac{\partial^2 \Phi}{\partial x^2} + \frac{\partial^2 \Phi}{\partial z^2}\Big)\Big], \tag{23}$$

$$\sigma_{zx} = \mu\Big[2\frac{\partial^2 q}{\partial x \partial z} - \frac{\partial^2 \psi}{\partial z^2} + \frac{\partial^2 \psi}{\partial x^2}\Big]. \tag{24}$$

The appropriate displacement potentials ψ, q, and Φ are taken in the form

$$\psi = C_1 \exp(ik_3(x \sin\theta_0 + z\cos\theta_0 - v_3 t)) + C_2 \exp(ik_3(x \sin\theta_3 - z\cos\theta_3 - v_3 t)), \tag{25}$$

$$q = A_1 \exp(ik_1(x \sin\theta_0 + z\cos\theta_0 - v_1 t)) + A_2 \exp(ik_1(x \sin\theta_1 - z\cos\theta_1 - v_1 t)) + A_3 \exp(ik_2(x \sin\theta_2 - z\cos\theta_2 - v_2 t)), \tag{26}$$

$$\Phi = \eta_1 A_1 \exp(ik_1(x \sin\theta_0 + z\cos\theta_0 - v_1 t)) + \eta_1 A_2 \exp(ik_1(x \sin\theta_1 - z\cos\theta_1 - v_1 t)) + \eta_2 A_3 \exp(ik_2(x \sin\theta_2 - z\cos\theta_2 - v_2 t)), \tag{27}$$

where the wave normal to the incident P or SV wave makes an angle θ_0 with the positive direction of the z-axis and those of the reflected P, thermal, and SV waves make angles θ_1, θ_2, and θ_3, respectively, with the same direction, and

$$\frac{\eta_1}{{k_1}^2} = \frac{\rho {v_1}^2 - (\lambda + 2\mu)}{\gamma(1 + a^* {k_1}^2)}, \qquad \frac{\eta_2}{{k_2}^2} = \frac{\rho {v_2}^2 - (\lambda + 2\mu)}{\gamma(1 + a^* {k_2}^2)}. \tag{28}$$

5. Reflection coefficients

The ratios of the amplitudes of the reflected waves to the amplitude of incident P wave, namely C_2/A_1, A_2/A_1, and A_3/A_1, are the reflection coefficients (amplitude ratios) of the reflected SV, reflected P, and reflected thermal waves, respectively. Similarly, for the incident SV wave, C_2/C_1, A_2/C_1, and A_3/C_1 are the reflection coefficients of the reflected SV, reflected P, and reflected thermal waves, respectively. The wave numbers k_1, k_2, and k_3 and the angles θ_0, θ_1, θ_2, and θ_3 are connected by the relation

$$k_1 \sin\theta_0 = k_3 \sin\theta_0 = k_1 \sin\theta_1 = k_2 \sin\theta_2 = k_3 \sin\theta_3, \tag{29}$$

at the surface $z = 0$. In order to satisfy the boundary conditions (20)–(22), we write (29) as

$$\frac{\sin\theta_0}{v_1 \text{ or } v_3} = \frac{\sin\theta_1}{v_1} = \frac{\sin\theta_2}{v_2} = \frac{\sin\theta_3}{v_3}. \tag{30}$$

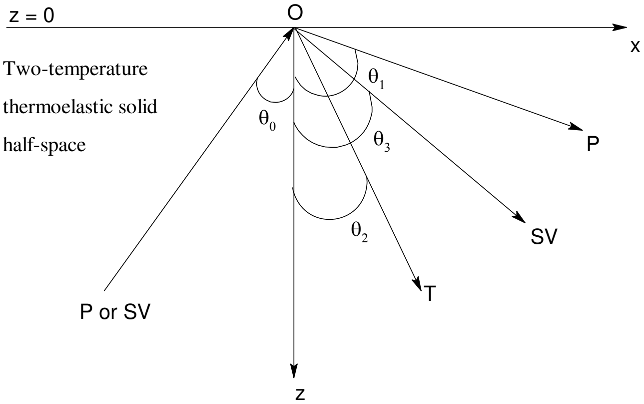

Figure 1. Geometry of the problem.

5.1. ***Incident P wave.*** Making use of the potentials given by (25)–(27) in the boundary conditions (20)–(22), we obtain a system of three nonhomogeneous equations which results in the following expressions for the reflection coefficients of the SV, P, and thermal waves:

$$\frac{C_2}{A_1}=\frac{D_1}{D},\qquad \frac{A_2}{A_1}=\frac{D_2}{D},\qquad \frac{A_3}{A_1}=\frac{D_3}{D}, \tag{31}$$

where

$$\begin{aligned} D=\frac{{v_1}^2}{v_2v_3}\Bigg[&2\mu\sin\theta_0\sin 2\theta_0(\eta_2-\eta_1)\sqrt{1-\frac{{v_3}^2}{{v_1}^2}\sin^2\theta_0}\sqrt{1-\frac{{v_2}^2}{{v_1}^2}\sin^2\theta_0}\\ &-\frac{v_1}{v_3}\left(1-2\frac{{v_3}^2}{{v_1}^2}\sin^2\theta_0\right)(\rho{v_1}^2-2\mu\sin^2\theta_0)\left(-\eta_2\sqrt{1-\frac{{v_2}^2}{{v_1}^2}\sin^2\theta_0}+\eta_1\frac{v_2}{v_1}\cos\theta_0\right)\Bigg], \end{aligned} \tag{32}$$

$$D_1=\frac{v_1}{v_2}\sin 2\theta_0(\rho{v_1}^2-2\mu\sin^2\theta_0)(\eta_2-\eta_1)\sqrt{1-\frac{{v_2}^2}{{v_1}^2}\sin^2\theta_0}\left(1+\sqrt{1-\frac{{v_2}^2}{{v_1}^2}\sin^2\theta_0}\right), \tag{33}$$

$$\begin{aligned} D_2=\frac{{v_1}^2}{v_2v_3}\Bigg[&2\mu\sin\theta_0\sin 2\theta_0(\eta_2-\eta_1)\sqrt{1-\frac{{v_3}^2}{{v_1}^2}\sin^2\theta_0}\sqrt{1-\frac{{v_2}^2}{{v_1}^2}\sin^2\theta_0}\\ &-\frac{v_1}{v_3}\left(1-2\frac{{v_3}^2}{{v_1}^2}\sin^2\theta_0\right)(\rho{v_1}^2-2\mu\sin^2\theta_0)\left(\eta_2\sqrt{1-\frac{{v_2}^2}{{v_1}^2}\sin^2\theta_0}+\eta_1\frac{v_2}{v_1}\cos\theta_0\right)\Bigg], \end{aligned} \tag{34}$$

$$D_3=2\eta_1\cos\theta_0\frac{{v_1}^2}{{v_3}^2}\left(1-2\frac{{v_3}^2}{{v_1}^2}\sin^2\theta_0\right)(\rho{v_1}^2-2\mu\sin^2\theta_0). \tag{35}$$

5.2. ***Incident SV wave.*** Similarly, making use of the potentials given by (25)–(27) in the boundary conditions (20)–(22), we obtain the following expressions for the reflection coefficients of the SV, P, and thermal waves:

$$\frac{C_2}{C_1}=\frac{D_1'}{D'},\qquad \frac{A_2}{C_1}=\frac{D_2'}{D'},\qquad \frac{A_3}{C_1}=\frac{D_3'}{D'}. \tag{36}$$

Here,

$$\begin{aligned} D'=-\frac{{v_3}^3}{v_1v_2}\Bigg[&\frac{2\mu}{{v_1}^2}\sin\theta_0\sin 2\theta_0(\eta_1-\eta_2)\sqrt{1-\frac{{v_3}^2}{{v_1}^2}\sin^2\theta_0}\sqrt{1-\frac{{v_2}^2}{{v_1}^2}\sin^2\theta_0}\\ &+\left(1-2\frac{{v_3}^2}{{v_1}^2}\sin^2\theta_0\right)(\rho{v_1}^2-2\mu\sin^2\theta_0)\left(\frac{\eta_2}{v_1}\sqrt{1-\frac{{v_2}^2}{{v_1}^2}\sin^2\theta_0}-\eta_1\frac{v_2}{{v_1}^2}\cos\theta_0\right)\Bigg], \end{aligned} \tag{37}$$

$$\begin{aligned} D_1'=-\frac{{v_3}^3}{v_1v_2}\Bigg[&\frac{\mu}{v_1}\sin^2 2\theta_0\sqrt{1-\frac{{v_2}^2}{{v_1}^2}\sin^2\theta_0}(\eta_2-\eta_1)\\ &-\frac{(\rho{v_1}^2-2\mu\sin^2\theta_0)}{v_1}\left(\eta_2\cos 2\theta_0\sqrt{1-\frac{{v_2}^2}{{v_1}^2}\sin^2\theta_0}-\frac{\eta_1}{v_1}v_2\cos\theta_0\right)\Bigg], \end{aligned} \tag{38}$$

$$D_2' = 2\mu\eta_2 \frac{v_3}{v_2} \sin\theta_0 \sqrt{1 - \frac{{v_2}^2}{{v_1}^2} \sin^2\theta_0} [\frac{v_3}{v_1} \cos 2\theta_0 \sqrt{1 - \frac{{v_3}^2}{{v_1}^2} \sin^2\theta_0} + \cos\theta_0 (1 - 2\frac{{v_3}^2}{{v_1}^2} \sin^2\theta_0)], \tag{39}$$

$$D_3' = -2\mu\eta_1 \frac{v_3}{v_1} \sin 2\theta_0 [\frac{v_3}{v_1} \cos 2\theta_0 \sqrt{1 - \frac{{v_3}^2}{{v_1}^2} \sin^2\theta_0} + \cos\theta_0 (1 - 2\frac{{v_3}^2}{{v_1}^2} \sin^2\theta_0)]. \tag{40}$$

6. Numerical results and discussion

To study numerically the effects of the two-temperature parameter on the speeds of propagation and reflection coefficients, we consider the following physical constants of aluminum as an isotropic thermoelastic solid half-space:

$$\lambda = 7.59 \times 10^{10}\,\mathrm{Nm}^{-2}, \quad \mu = 1.89 \times 10^{10}\,\mathrm{Nm}^{-2}, \quad K = 237\,\mathrm{Wm}^{-1}\mathrm{deg}^{-1},$$
$$C_e = 24.2\,\mathrm{Jkg}^{-1}\mathrm{deg}^{-1}, \quad \rho = 2.7 \times 10^3\,\mathrm{kgm}^{-3}, \quad T_0 = 296\,\mathrm{K}, \quad \tau_0 = 0.05\,\mathrm{s}, \quad \omega = 20\,\mathrm{s}^{-1}.$$

Using the relation $V_j^{-1} = v_j^{-1} - \imath\omega^{-1} q_j$ $(j = 1, \ldots, 3)$, the real values of the propagation speeds of the P, SV, and thermal waves are computed for the range $0 \le a^* \le 1$ of the two-temperature parameter. The speeds of the P, SV, and thermal waves are shown graphically against the two-temperature parameter a^* in Figure 2. The speed of the P wave decreases with an increase in the two-temperature parameter, whereas the speed of the thermal wave increases. The speed of the SV wave is not affected by change in the two-temperature parameter.

With the help of (31), the reflection coefficients of the reflected P, SV, and thermal waves are computed for the incidence of a P wave. For the range $0° < \theta_0 \le 90°$ of the angle of incidence of the P wave, the reflection coefficients of the P, thermal, and SV waves are shown graphically in Figure 3, when $a^* = 0$, 0.5, and 1. For $a^* = 1$, the reflection coefficient of the P wave decreases from its maximum value of 1.211 at $\theta_0 = 1°$ to its minimum value of 0.88 at $\theta_0 = 69°$. Thereafter, it increases up to the grazing incidence. For $a^* = 1$, the reflection coefficient of the thermal wave decreases from its maximum

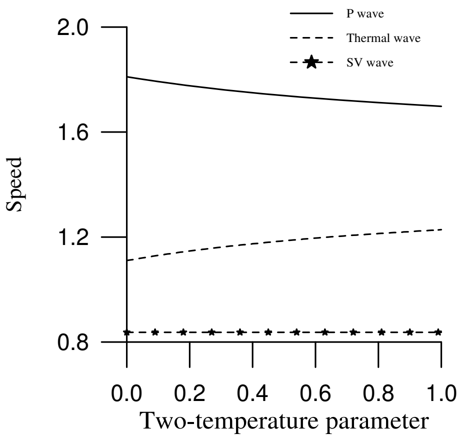

Figure 2. Variations of speed of reflected P wave (solid line), thermal wave (dashed line, and SV wave (dashed line with stars) against the two-temperature parameter.

value of 0.7132 at $\theta = 1°$ to its minimum value of zero at $\theta_0 = 90°$. For $a^* = 1$, the reflection coefficient of SV wave increases from its minimum value of zero at normal incidence to its maximum value of 0.5062 at $\theta_0 = 48°$. Beyond $\theta_0 = 48°$, it decreases to its minimum value of zero at grazing incidence. From Figure 3, it is observed that the effect of a^* on the reflection coefficients of the P and thermal waves is maximal at normal incidence. The effect of the two-temperature parameter on these waves decreases with increase in the angle of incidence. For grazing incidence, there is no effect of the two-temperature parameter on these reflected waves. The reflection coefficient of SV is also affected by two-temperature parameter. For normal and grazing incidences, there is no effect of two-temperature parameter on the reflected SV wave. The maximal effect of the two-temperature parameter on the reflected SV wave is observed at $\theta_0 = 45°$.

With the help of (36), the reflection coefficients of the reflected P, SV, and thermal waves are computed for the incidence of a SV wave. For the range $0° < \theta_0 \leq 27°$ of the angle of incidence of the SV wave, the reflection coefficients of the P, thermal, and SV waves are shown graphically in Figure 4, when $a^* = 0$, 0.5 and 1. For $a^* = 1$, the reflection coefficient of the P wave increases from its minimum

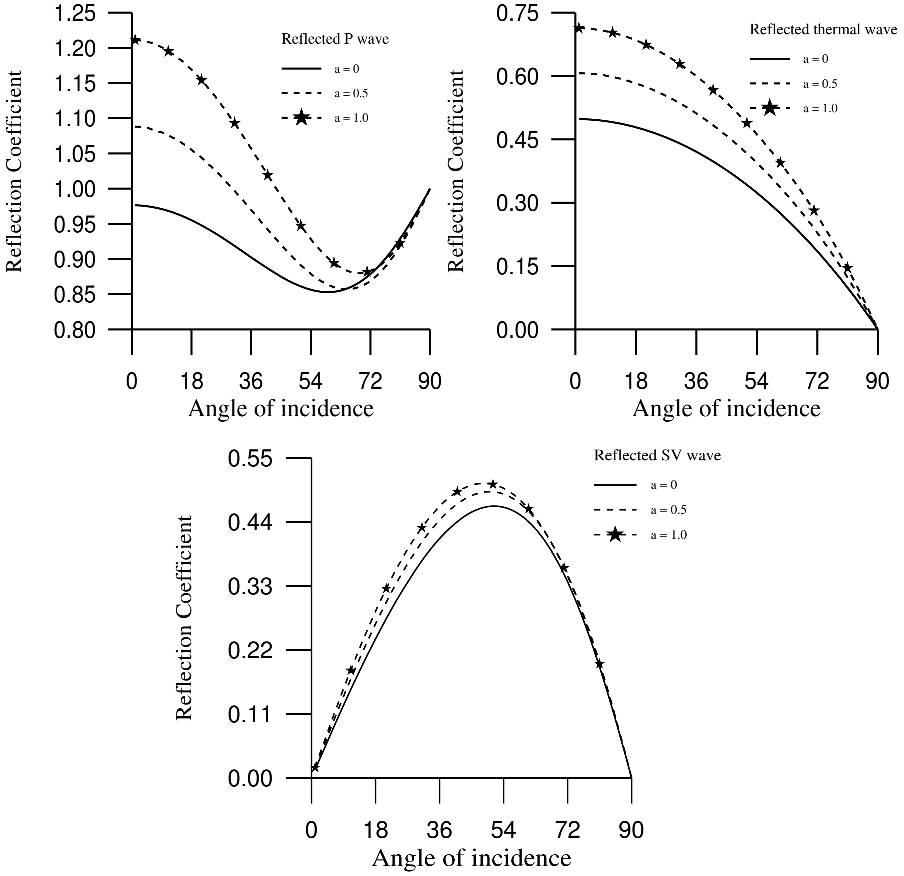

Figure 3. Variation in the reflection coefficients of the reflected P (top left), thermal (top right), and SV (bottom) waves against the angle of incidence of the incident P wave.

value of 0.07 at $\theta_0 = 1°$ to its maximum value of 1.926 at $\theta_0 = 27°$. For $a^* = 1$, the reflection coefficient of the thermal wave increases from its minimum value of 0.02 at $\theta = 1°$ to its maximum value of 0.3887 at $\theta_0 = 23°$. Thereafter, it decreases up to the angle of incidence $\theta = 27°$. For $a^* = 1$, the reflection coefficient of the SV wave decreases from its maximum value of one at normal incidence to its minimum value of 0.5992 at $\theta_0 = 26°$. Thereafter, it increases to a value of 0.6058 at $\theta_0 = 27°$. From Figure 4, it is observed that the effect of a^* on the reflection coefficients of the P wave is maximal at angles near $\theta_0 = 20°$. There is no effect of the two-temperature parameter on this wave at normal incidence. At normal incidence, the reflected thermal and SV waves are also not affected by a^*. The effect of a^* on these reflected waves increases with the increase in the angle of incidence and it becomes maximal at angles near $\theta_0 = 25°$.

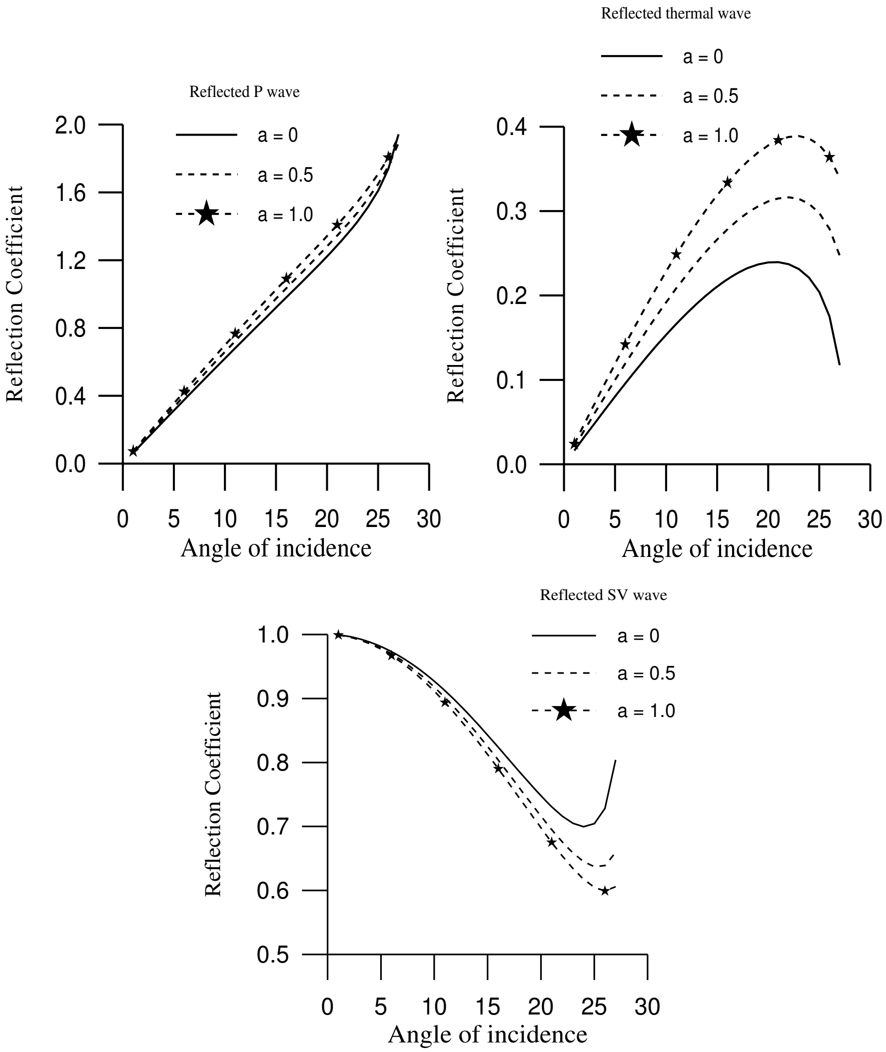

Figure 4. Variation in the reflection coefficients of the reflected P (top left), thermal (top right), and SV (bottom) waves against the angle of incidence of the incident SV wave.

7. Conclusion

The two-dimensional solution of the governing equations of an isotropic two-temperature thermoelastic medium indicates the existence of three plane waves, namely the P, thermal, and SV waves. The expressions for the speeds of the P, thermal, and SV waves are obtained explicitly. The reflection coefficients of the reflected P, thermal, and SV waves are also obtained in closed form for the incidence of P and SV waves. The speeds and reflection coefficients of plane waves are computed for a particular material representing the model. From the theory and numerical results, it is observed that the speeds and reflection coefficients of the plane waves are significantly affected by the two-temperature parameter.

References

[Boley and Tolins 1962] B. A. Boley and I. S. Tolins, "Transient coupled thermoelastic boundary value problems in the half-space", *J. Appl. Mech.* (*ASME*) **29**:4 (1962), 637–646.

[Chen and Gurtin 1968] P. J. Chen and M. E. Gurtin, "On a theory of heat conduction involving two temperatures", *Z. Angew. Math. Phys.* **19**:4 (1968), 614–627.

[Chen et al. 1968] P. J. Chen, M. E. Gurtin, and W. O. Williams, "A note on non-simple heat conduction", *Z. Angew. Math. Phys.* **19**:6 (1968), 969–970.

[Chen et al. 1969] P. J. Chen, M. E. Gurtin, and W. O. Williams, "On the thermodynamics of non-simple elastic materials with two temperatures", *Z. Angew. Math. Phys.* **20**:1 (1969), 107–112.

[Deresiewicz 1960] H. Deresiewicz, "Effect of boundaries on waves in a thermoelastic solid: reflexion of plane waves from a plane boundary", *J. Mech. Phys. Solids* **8**:3 (1960), 164–172.

[Ezzat and El-Karamany 2011] M. A. Ezzat and A. S. El-Karamany, "Two-temperature theory in generalized magneto-thermo-elasticity with two relaxation times", *Meccanica* (*Milano*) **46**:4 (2011), 785–794.

[Green and Lindsay 1972] A. E. Green and K. A. Lindsay, "Thermoelasticity", *J. Elasticity* **2**:1 (1972), 1–7.

[Gurtin and Williams 1966] M. E. Gurtin and W. O. Williams, "On the Clausius–Duhem inequality", *Z. Angew. Math. Phys.* **17**:5 (1966), 626–633.

[Gurtin and Williams 1967] M. E. Gurtin and W. O. Williams, "An axiomatic foundation for continuum thermodynamics", *Arch. Ration. Mech. Anal.* **26**:2 (1967), 83–117.

[Hetnarski and Ignaczak 1999] R. B. Hetnarski and J. Ignaczak, "Generalized thermoelasticity", *J. Therm. Stresses* **22**:4-5 (1999), 451–476.

[Ignaczak and Ostoja-Starzewski 2010] J. Ignaczak and M. Ostoja-Starzewski, *Thermoelasticity with finite wave speeds*, Oxford University Press, Oxford, 2010.

[Kumar and Mukhopadhyay 2010] R. Kumar and S. Mukhopadhyay, "Effects of thermal relaxation time on plane wave propagation under two-temperature thermoelasticity", *Int. J. Eng. Sci.* **48**:2 (2010), 128–139.

[Lord and Shulman 1967] H. W. Lord and Y. Shulman, "A generalized dynamical theory of thermoelasticity", *J. Mech. Phys. Solids* **15**:5 (1967), 299–309.

[Magaña and Quintanilla 2009] A. Magaña and R. Quintanilla, "Uniqueness and growth of solutions in two-temperature generalized thermoelastic theories", *Math. Mech. Solids* **14**:7 (2009), 622–634.

[Othman and Song 2007] M. I. A. Othman and Y. Song, "Reflection of plane waves from an elastic solid half-space under hydrostatic initial stress without energy dissipation", *Int. J. Solids Struct.* **44**:17 (2007), 5651–5664.

[Puri and Jordan 2006] P. Puri and P. M. Jordan, "On the propagation of harmonic plane waves under the two-temperature theory", *Int. J. Eng. Sci.* **44**:17 (2006), 1113–1126.

[Quintanilla and Jordan 2009] R. Quintanilla and P. M. Jordan, "A note on the two temperature theory with dual-phase-lag delay: some exact solutions", *Mech. Res. Commun.* **36**:7 (2009), 796–803.

[Sharma et al. 2003] J. N. Sharma, V. Kumar, and D. Chand, "Reflection of generalized thermoelastic waves from the boundary of a half-space", *J. Therm. Stresses* **26**:10 (2003), 925–942.

[Singh 2008] B. Singh, "Effect of hydrostatic initial stresses on waves in a thermoelastic solid half-space", *Appl. Math. Comput.* **198**:2 (2008), 494–505.

[Singh 2010] B. Singh, "Reflection of plane waves at the free surface of a monoclinic thermoelastic solid half-space", *Eur. J. Mech. A Solids* **29**:5 (2010), 911–916.

[Sinha and Elsibai 1996] S. B. Sinha and K. A. Elsibai, "Reflection of thermoelastic waves at a solid half-space with two relaxation times", *J. Therm. Stresses* **19**:8 (1996), 749–762.

[Sinha and Elsibai 1997] S. B. Sinha and K. A. Elsibai, "Reflection and refraction of thermoelastic waves at an interface of two semi-infinite media with two relaxation times", *J. Therm. Stresses* **20**:2 (1997), 129–146.

[Sinha and Sinha 1974] A. N. Sinha and S. B. Sinha, "Reflection of thermoelastic waves at a solid half-space with thermal relaxation", *J. Phys. Earth* **22**:2 (1974), 237–244.

[Warren and Chen 1973] W. E. Warren and P. J. Chen, "Wave propagation in the two temperature theory of thermoelasticity", *Acta Mech.* **16**:1–2 (1973), 21–33.

[Youssef 2006] H. M. Youssef, "Theory of two-temperature-generalized thermoelasticity", *IMA J. Appl. Math.* **71**:3 (2006), 383–390.

[Youssef 2011] H. M. Youssef, "Theory of two-temperature thermoelasticity without energy dissipation", *J. Therm. Stresses* **34**:2 (2011), 138–146.

Received 9 Jul 2011. Revised 14 Aug 2011. Accepted 23 Sep 2011.

BALJEET SINGH: `bsinghgc11@yahoo.com`
Department of Mathematics, Postgraduate Government College, Sector 11, Chandigarh 160011, India

KIRAN BALA: `kirandulat@gmail.com`
Department of Mathematics, Government College, Barwala, Panchkula, Haryana, India

JOURNAL OF MECHANICS OF MATERIALS AND STRUCTURES
Vol. 7, No. 2, 2012

A NONLINEAR TIMOSHENKO BEAM FORMULATION BASED ON STRAIN GRADIENT THEORY

REZA ANSARI, RAHEB GHOLAMI AND MOHAMMAD ALI DARABI

Developed herein is a comprehensive geometrically nonlinear size-dependent microscale Timoshenko beam model based on strain gradient and von Kármán theories. The nonlinear governing equations and the corresponding boundary conditions are derived from employing Hamilton's principle. A simply supported microbeam is considered to delineate the nonlinear size-dependent free vibration behavior of the presented model. Utilizing the harmonic balance method, the solution for free vibration is presented analytically. The influence of the geometric parameters, Poisson's ratio, and material length-scale parameters on the linear frequency and nonlinear frequency ratio are thoroughly investigated. The results obtained from the present model are compared, in special cases, with those of the linear strain gradient theory, linear and nonlinear modified couple stress theory, and linear and nonlinear classical models; excellent agreement is found. It is concluded that the nonlinear natural frequency and nonlinear frequency ratio predicted by strain gradient theory are more precise than those from the other theories mentioned, especially for shorter beams.

1. Introduction

Micro- and nanoscale beams are increasingly used in micro- and nanoelectromechanical systems such as vibration shock sensors [Lun et al. 2006], electrostatically excited microactuators [Moghimi Zand and Ahmadian 2009; Mojahedi et al. 2010], microswitches [Coutu et al. 2004], and atomic force microscopes [Mahdavi et al. 2008]. The thickness of microscale beams is on the order of microns and submicrons. The size-dependent deformation behavior in microscale beams has been detected experimentally [Fleck et al. 1994; Lam et al. 2003]. Moreover, experiments confirm the significance of the effects of nonlinearity on the behavior of micro and nanomechanical resonators [Turner et al. 1998; Craighead 2000; Scheible et al. 2002].

Due to the absence of a material length-scale parameter, classical continuum mechanics is not able to interpret and predict such a size-dependent phenomenon which occurs in micron and submicron-scale structures. Accordingly, many attempts have been made to develop different size-dependent continuum theories such as the couple stress elasticity [Mindlin and Tiersten 1962; Toupin 1962], nonlocal elasticity [Eringen 1972], strain gradient elasticity [Aifantis 1999], and surface elasticity [Gurtin et al. 1998] theories. On the basis of elasticity theory, Yang et al. [2002] proposed a modified couple stress theory for elasticity in which only one higher-order material constant exists in the constitutive equations. In recent years, this theory has been applied by many researchers to interpret the size-dependent static and

---

Keywords: microbeams, strain gradient elasticity, modified couple stress theory, size effect, nonlinear behavior, Timoshenko beam theory.

vibration behaviors of microstructures [Lazopoulos 2004; Park and Gao 2006; Kong et al. 2008; Ma et al. 2008; 2010; 2011; Asghari et al. 2010b; 2010a; Lazopoulos and Lazopoulos 2010].

Lazopoulos [2004] was apparently the first to employ the von Kármán kinematic relations in nonclassical analyses of beams and plates. Mindlin [1965] proposed a higher-order gradient theory for elastic materials by considering the first and second derivatives of the strain tensor effective on the strain energy density. In [Fleck and Hutchinson 1993; 1997; 2001], Mindlin's proposition was reformulated by considering only the first derivative of the strain this was called strain gradient theory. In comparison to couple stress theory, this theory comprises several higher-order stress components together with the classical and couple stresses. This means that couple stress theory can be attained via strain gradient theory by omitting the additional higher-order stress components. In this direction, Lam et al. [2003] modified strain gradient theory by considering three higher-order material constants in the constitutive equations. Also, this theory can be regenerated into the modified couple stress theory of [Yang et al. 2002] by setting the two material length-scale parameters equal to zero. In another work, Ma et al. [2011] developed a nonclassical Mindlin plate model based on modified couple stress theory. Tsepoura et al. [2002] have investigated the size effect of the Bernoulli–Euler beam model. In [Papargyri-Beskou et al. 2003b; Park and Gao 2006], based on the gradient elasticity theory with surface energy of [Vardoulakis and Sulem 1995], a higher-order Bernoulli–Euler beam model was expanded. Also, a cantilever beam subjected to bending and a cracked bar under stretching have been investigated by using the strain gradient beam model of [Giannakopoulos and Stamoulis 2007]. Wang et al. [2010], on the basis of strain gradient elasticity theory, developed a microscale Timoshenko beam model in which the Poisson effect was incorporated and also investigated the static bending and free vibration of a simply supported microscale Timoshenko beam to illustrate this model. Kahrobaiyan et al. [2011] developed a nonlinear size-dependent Euler–Bernoulli beam model based on strain gradient theory.

In the current work, by employing strain gradient theory and Hamilton's principle, a large-deformation size-dependent Timoshenko microbeam model is presented. The present model accommodates some previously published beam models including the linear couple stress [Park and Gao 2006; Kong et al. 2008; Ma et al. 2008], linear strain gradient [Kaneko 1975; Kahrobaiyan et al. 2011], nonlinear couple stress [Asghari et al. 2010b], nonlinear strain gradient [Kahrobaiyan et al. 2011] theories. Then, utilizing this model, the nonlinear size-dependent free vibration behavior of simply supported microbeams is described using the harmonic balance method. The numerical results are illustrated to study the effects of the geometric parameters, Poisson's ratio, and material length-scale parameters on the linear frequency and nonlinear frequency ratio.

2. Preliminaries

In comparison to the modified couple stress theory of [Yang et al. 2002], Lam et al. [2003] has presented a strain gradient elasticity theory which in addition to the symmetric rotation gradient tensor presents two additional gradient tensors, the dilatation gradient tensor and the deviatoric stretch gradient tensor. These tensors are specified by two classical material constants for isotropic linear elastic materials and three independent material length-scale parameters. The stored strain energy U_m in a continuum constructed by a linear elastic material occupying a region Ω with infinitesimal deformations is given by

$$U_m = \frac{1}{2}\int_{\Omega}\left(\sigma_{ij}\varepsilon_{ij} + p_i\gamma_i + \tau^{(1)}_{ijk}\eta^{(1)}_{ijk} + m^s_{ij}\chi^s_{ij}\right) dv, \tag{1}$$

in which the components of the strain tensor, the dilatation gradient tensor, the deviatoric stretch gradient tensor, and the symmetric rotation gradient tensor, respectively represented by ε_{ij}, γ_i, $\eta^{(1)}_{ijk}$, and χ^s_{ij} [Lam et al. 2003], are defined as

$$\varepsilon_{ij} = \tfrac{1}{2}(u_{i,j} + u_{j,i}), \qquad \gamma_i = \varepsilon_{mm,i}, \tag{2a}$$

$$\eta^{(1)}_{ijk} = \tfrac{1}{3}(\varepsilon_{jk,i} + \varepsilon_{ki,j} + \varepsilon_{ij,k}) - \tfrac{1}{15}\delta_{ij}(\varepsilon_{mm,k} + 2\varepsilon_{mk,m}) - \tfrac{1}{15}[\delta_{jk}(\varepsilon_{mm,i} + 2\varepsilon_{mi,m}) + \delta_{ki}(\varepsilon_{mm,j} + 2\varepsilon_{mj,m})], \tag{2b}$$

$$\chi^s_{ij} = \tfrac{1}{2}(\theta_{i,j} + \theta_{j,i}), \qquad \theta_i = \tfrac{1}{2}(\mathrm{curl}(u))_i, \tag{2c}$$

where u_i represents the components of the displacement vector u, θ_i is the infinitesimal rotation vector θ, and δ is Kronecker's delta. For a linear isotropic elastic material, the stresses are explained by the kinematic parameters effective on the strain energy density which are given in the following constitutive relations [Lam et al. 2003]:

$$\sigma_{ij} = \lambda tr(\varepsilon)\delta_{ij} + 2\mu\varepsilon_{ij}, \qquad p_i = 2\mu l_0^2 \gamma_i, \qquad \tau^{(1)}_{ijk} = 2\mu l_1^2 \eta^{(1)}_{ijk}, \qquad m^s_{ij} = 2\mu l_2^2 \chi^s_{ij}. \tag{3}$$

The parameters $\boldsymbol{p}$, $\boldsymbol{\tau}^{(1)}$, and $\boldsymbol{m}^s$ are called the higher-order stresses. In the constitutive equation of the classical stress $\boldsymbol{\sigma}$, the parameters λ and μ are the bulk and shear modules, respectively, and are given as [Timoshenko and Goodier 1970]

$$\lambda = \frac{E\nu}{(1+\nu)(1-2\nu)}, \qquad \mu = \frac{E}{2(1+\nu)}. \tag{4}$$

Also, l_0, l_1, and l_2 appearing in the higher-order stresses represent the additional independent material length-scale parameters connected with the dilatation gradients, deviatoric stretch gradients, and symmetric rotation gradients, respectively. The kinematics of the Timoshenko beam theory can be written as [Reddy 2007]

$$u_1 = u(x,t) - z\psi(x,t), \qquad u_2 = 0, \qquad u_3 = w(x,t), \tag{5}$$

where $u(x,t)$, $w(x,t)$, and $\psi(x,t)$ stand for the axial displacement of the center of sections, the lateral deflection of the beam, and the rotation angle of the cross section with respect to the vertical direction.

3. Nonlinear formulation of motion and corresponding boundary conditions

As depicted in Figure 1, a straight beam of length L subjected to an initial axial load $N_0(x)$ is considered in which its top and bottom surfaces are perpendicular to the z-direction. The centroid of each section is assumed to be located on the plane $z = 0$. The kinematic parameters, boundary conditions, and loading of a Timoshenko beam modeled based on the strain gradient theory are demonstrated in this figure. In addition, $G(x,t)$ is related to the axial body force per unit length and $F(x,t)$ denotes the transverse distributed force intensity per unit length.

Based on Timoshenko beam theory under the assumption of small strains and moderate rotations, the nonlinear strain-displacement relations of a beam subjected to large-amplitude vibrations can be approximated by the von Kármán relation as [Reddy 2003; Ma et al. 2008; Asghari et al. 2010b]

$$\varepsilon_{11} = \frac{\partial u_1}{\partial x} + \frac{1}{2}\left(\frac{\partial w}{\partial x}\right)^2 = \frac{\partial u}{\partial x} - z\frac{\partial \psi}{\partial x} + \frac{1}{2}\left(\frac{\partial w}{\partial x}\right)^2, \quad \varepsilon_{13} = \frac{1}{2}\left(\frac{\partial w}{\partial x} - \psi\right). \tag{6}$$

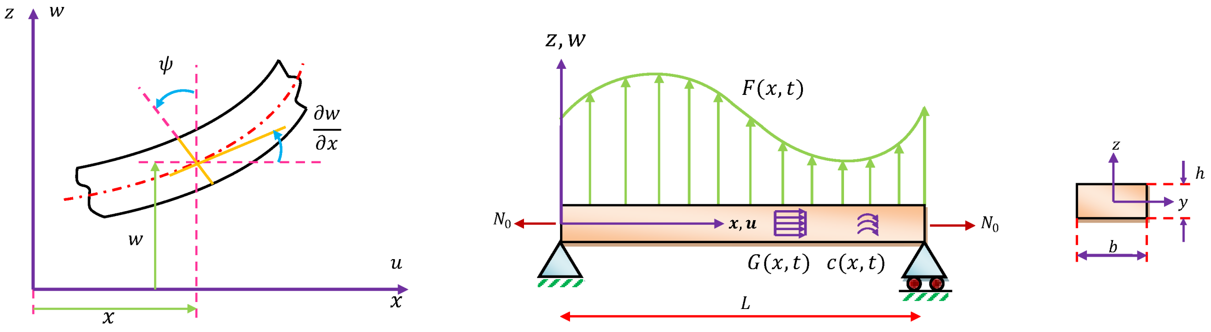

Figure 1. Schematic of a simply supported Timoshenko beam: kinematic parameters, coordinate system, geometry, and loading.

By inserting (5) and (6) into (2), the following nonzero components of $\boldsymbol{\theta}$, $\boldsymbol{\chi}^s$, $\boldsymbol{\gamma}$, and $\boldsymbol{\eta}^{(1)}$ will be achieved:

$$\theta_2 = -\frac{1}{2}\left(\psi + \frac{\partial w}{\partial x}\right), \qquad \chi^s_{12} = \chi^s_{21} = -\frac{1}{4}\left(\frac{\partial \psi}{\partial x} + \frac{\partial^2 w}{\partial x^2}\right), \tag{7a}$$

$$\gamma_1 = \frac{\partial^2 u}{\partial x^2} - z\frac{\partial^2 \psi}{\partial x^2} + \frac{\partial w}{\partial x}\cdot\frac{\partial^2 w}{\partial x^2}, \qquad \gamma_3 = -\frac{\partial \psi}{\partial x}, \tag{7b}$$

$$\begin{aligned}
&\eta^{(1)}_{111} = \frac{2}{5}\left(\frac{\partial^2 u}{\partial x^2} - z\frac{\partial^2 \psi}{\partial x^2} + \frac{\partial w}{\partial x}\cdot\frac{\partial^2 w}{\partial x^2}\right), \qquad \eta^{(1)}_{333} = -\frac{1}{5}\left(\frac{\partial^2 w}{\partial x^2} - 2\frac{\partial \psi}{\partial x}\right),\\
&\eta^{(1)}_{113} = \eta^{(1)}_{311} = \eta^{(1)}_{131} = \frac{4}{15}\left(\frac{\partial^2 w}{\partial x^2} - 2\frac{\partial \psi}{\partial x}\right), \qquad \eta^{(1)}_{223} = \eta^{(1)}_{322} = \eta^{(1)}_{232} = -\frac{1}{15}\left(\frac{\partial^2 w}{\partial x^2} - 2\frac{\partial \psi}{\partial x}\right),\\
&\eta^{(1)}_{221} = \eta^{(1)}_{212} = \eta^{(1)}_{122} = \eta^{(1)}_{313} = \eta^{(1)}_{133} = \eta^{(1)}_{331} = -\frac{1}{5}\left(\frac{\partial^2 u}{\partial x^2} - z\frac{\partial^2 \psi}{\partial x^2} + \frac{\partial w}{\partial x}\cdot\frac{\partial^2 w}{\partial x^2}\right).
\end{aligned} \tag{7c}$$

The major components of the symmetric section of the stress tensor can be expressed by the kinematic parameters as follows:

$$\begin{aligned}
&\sigma_{11} = (\lambda + 2\mu)\left(\frac{\partial u}{\partial x} - z\frac{\partial \psi}{\partial x} + \frac{1}{2}\left(\frac{\partial w}{\partial x}\right)^2\right), \qquad \sigma_{22} = \lambda\left(\frac{\partial u}{\partial x} - z\frac{\partial \psi}{\partial x} + \frac{1}{2}\left(\frac{\partial w}{\partial x}\right)^2\right),\\
&\sigma_{33} = \lambda\left(\frac{\partial u}{\partial x} - z\frac{\partial \psi}{\partial x} + \frac{1}{2}\left(\frac{\partial w}{\partial x}\right)^2\right), \qquad \sigma_{13} = \mu\left(\frac{\partial w}{\partial x} - \psi\right).
\end{aligned} \tag{8}$$

Note that σ_{13} depends only on one direction. Due to taking the nonuniformity of the shear strain over the beam cross-section into account, a correction factor k_s, which depends on the shape of the beam section, is multiplied into the stress component σ_{13} as follows [Hutchinson 2001; Wang et al. 2010]:

$$\sigma_{13} = k_s\mu\left(\frac{\partial w}{\partial x} - \psi\right). \tag{9}$$

At last, by inserting (6)–(9) into (3), the nonzero components of the higher-order stresses are obtained:

$$p_1 = 2\mu l_0^2\Big(\frac{\partial^2 u}{\partial x^2} - z\frac{\partial^2\psi}{\partial x^2} + \frac{\partial w}{\partial x}\cdot\frac{\partial^2 w}{\partial x^2}\Big), \qquad p_3 = -2\mu l_0^2\frac{\partial\psi}{\partial x}, \tag{10a}$$

$$\tau^{(1)}_{111} = \frac{4\mu l_1^2}{5}\Big(\frac{\partial^2 u}{\partial x^2} - z\frac{\partial^2\psi}{\partial x^2} + \frac{\partial w}{\partial x}\cdot\frac{\partial^2 w}{\partial x^2}\Big), \qquad \tau^{(1)}_{333} = -\frac{2\mu l_1^2}{5}\Big(\frac{\partial^2 w}{\partial x^2} - 2\frac{\partial\psi}{\partial x}\Big), \tag{10b}$$

$$\tau^{(1)}_{113} = \tau^{(1)}_{311} = \tau^{(1)}_{131} = \frac{8\mu l_1^2}{15}\Big(\frac{\partial^2 w}{\partial x^2} - 2\frac{\partial\psi}{\partial x}\Big), \qquad \tau^{(1)}_{223} = \tau^{(1)}_{322} = \tau^{(1)}_{232} = -\frac{2\mu l_1^2}{15}\Big(\frac{\partial^2 w}{\partial x^2} - 2\frac{\partial\psi}{\partial x}\Big), \tag{10c}$$

$$\tau^{(1)}_{221} = \tau^{(1)}_{212} = \tau^{(1)}_{122} = \tau^{(1)}_{313} = \tau^{(1)}_{133} = \tau^{(1)}_{331} = -\frac{2\mu l_1^2}{5}\Big(\frac{\partial^2 u}{\partial x^2} - z\frac{\partial^2\psi}{\partial x^2} + \frac{\partial w}{\partial x}\cdot\frac{\partial^2 w}{\partial x^2}\Big), \tag{10d}$$

$$m^s_{12} = m^s_{21} = -\frac{\mu l_2^2}{2}\Big(\frac{\partial\psi}{\partial x} + \frac{\partial^2 w}{\partial x^2}\Big). \tag{10e}$$

The initial axial stress in the beam, which is uniformly distributed in a section, can be written as $\sigma^{(0)}_{11}(x) = N_0(x)/A$. Accordingly, (6) and (8) for ε_{11} and σ_{11} do not express the total values of the strain and the stress changes with respect to the fully unloaded conditions, but only express them with respect to the initial configuration.

In the following, the strain energy resulted from the advent of a variation in the classical and higher-order stresses with respect to the initial configuration denoted by U_1, the strain energy due to the presence of the initial axial stresses and the next imposed stretching denoted by U_2, and the beam's kinetic energy, T, are expressed as:

$$U_1 = \frac{1}{2}\int_0^L\int_A \big(\sigma_{ij}\varepsilon_{ij} + p_i\gamma_i + \tau^{(1)}_{ijk}\eta^{(1)}_{ijk} + m^s_{ij}\chi^s_{ij}\big)\,dA\,dx = \frac{1}{2}\int_0^L\int_A\bigg\{(\lambda+2\mu)\Big(\frac{\partial u}{\partial x} - z\frac{\partial\psi}{\partial x} + \frac{1}{2}\Big(\frac{\partial w}{\partial x}\Big)^2\Big)^2$$
$$+ k_s\mu\Big(\frac{\partial w}{\partial x} - \psi\Big)^2 + 2\mu l_0^2\Big(\frac{\partial\psi}{\partial x}\Big)^2 + \Big(2\mu l_0^2 + \frac{20\mu l_1^2}{25}\Big)\Big(\frac{\partial^2 u}{\partial x^2} - z\frac{\partial^2\psi}{\partial x^2} + \frac{\partial w}{\partial x}\cdot\frac{\partial^2 w}{\partial x^2}\Big)^2$$
$$+ \frac{40\mu l_1^2}{75}\Big(\frac{\partial^2 w}{\partial x^2} - 2\frac{\partial\psi}{\partial x}\Big)^2 + \frac{\mu l_2^2}{4}\Big(\frac{\partial\psi}{\partial x} + \frac{\partial^2 w}{\partial x^2}\Big)^2\bigg\}\,dA\,dx,$$

$$U_2 = \int_0^L \frac{N_0}{A}\int_A\Big(\frac{\partial u}{\partial x} - z\frac{\partial\psi}{\partial x} + \frac{1}{2}\Big(\frac{\partial w}{\partial x}\Big)^2\Big)\,dA\,dx, \qquad T = \frac{1}{2}\int_0^L\int_A \rho\bigg\{\Big(\frac{\partial u}{\partial t} - z\frac{\partial\psi}{\partial t}\Big)^2 + \Big(\frac{\partial w}{\partial t}\Big)^2\bigg\}\,dA\,dx,$$

where ρ and I are the density and area moments of inertia of sections with respect to the y-axis, respectively, and the latter is given by $I = \int_A z^2\,dA$. Also, note that $\int_A z\,dA = 0$. Hence, for the total potential energy $U = U_1 + U_2$ and the kinetic energy we will have

$$U = \frac{1}{2}\int_0^L\bigg\{k_1\Big(\frac{\partial u}{\partial x} + \frac{1}{2}\Big(\frac{\partial w}{\partial x}\Big)^2\Big)^2 + k_2\Big(\frac{\partial\psi}{\partial x}\Big)^2 + k_3\Big(\frac{\partial w}{\partial x} - \psi\Big)^2 + k_4\Big(\frac{\partial^2\psi}{\partial x^2}\Big)^2 + k_5\Big(\frac{\partial^2 u}{\partial x^2} + \frac{\partial w}{\partial x}\cdot\frac{\partial^2 w}{\partial x^2}\Big)^2$$
$$+ k_6\Big(\frac{\partial^2 w}{\partial x^2} - 2\frac{\partial\psi}{\partial x}\Big)^2 + k_7\Big(\frac{\partial\psi}{\partial x} + \frac{\partial^2 w}{\partial x^2}\Big)^2 + N_0\Big(2\frac{\partial u}{\partial x} + \Big(\frac{\partial w}{\partial x}\Big)^2\Big)\bigg\}\,dx, \tag{11}$$

$$T = \frac{1}{2}\int_0^L\bigg\{\rho A\Big(\frac{\partial u}{\partial t}\Big)^2 + \rho I\Big(\frac{\partial\psi}{\partial t}\Big)^2 + \rho A\Big(\frac{\partial w}{\partial t}\Big)^2\bigg\}\,dx, \tag{12}$$

where

$$\begin{aligned} &k_1=(\lambda+2\mu)A, && k_2=(\lambda+2\mu)I+2\mu A l_0^2, && k_3=k_s\mu A, && k_4=\mu I\big(2l_0^2+\tfrac{4}{5}l_1^2\big),\\ &k_5=\mu A\big(2l_0^2+\tfrac{4}{5}l_1^2\big), && k_6=\tfrac{8}{15}\mu A l_1^2, && k_7=\tfrac{1}{4}\mu A l_2^2. \end{aligned} \tag{13}$$

The external induced work associated with the body forces, body couples, and boundary surface tractions is

$$W^{\text{ext}}=\int_0^L (G(x,t)u+F(x,t)w+C(x,t)\theta_2)\,dx \\ +\Big(\hat{N}u+\hat{V}w+\hat{M}_\sigma\psi+\hat{M}_M\frac{\partial w}{\partial x}+\hat{P}\Big(\frac{\partial u}{\partial x}+\frac{1}{2}\Big(\frac{\partial w}{\partial x}\Big)^2\Big)+\hat{Q}\frac{\partial \psi}{\partial x}\Big)\Big|_{x=0}^{x=L}, \tag{14}$$

in which $\hat{N}$ is the axial resultant force of normal stresses $\sigma_{xx}+N_0/A$, $\hat{V}$ denotes the transverse resultant force of the shear stresses and $\hat{M}_M$ the resultant moment in a section caused by the classical and higher-order stress components, and $\hat{M}_\sigma$ is the resultant moment around the y-axis due to the couple stresses m_{xy} at sections. In addition, the higher-order resultants in a section are denoted by $\hat{P}$ and $\hat{Q}$, which are due to higher-order stresses acting on that section.

By employing the Hamilton principle,

$$\delta\int_{t_1}^{t_2}(T-U+W^{\text{ext}})\,dt=0, \tag{15}$$

taking the variation of u, w, and ψ, integrating by parts, and finally the coefficients of δu, δw, and $\delta\psi$ equal to zero, we obtain the governing equations of motion

$$\frac{\partial}{\partial x}\Big\{N_0+k_1\Big(\frac{\partial u}{\partial x}+\frac{1}{2}\Big(\frac{\partial w}{\partial x}\Big)^2\Big)-k_5\frac{\partial^2}{\partial x^2}\Big(\frac{\partial u}{\partial x}+\frac{1}{2}\Big(\frac{\partial w}{\partial x}\Big)^2\Big)\Big\}+G(x,t)=\rho A\frac{\partial^2 u}{\partial t^2}, \tag{16a}$$

$$\frac{\partial}{\partial x}\Big\{\Big[N_0+k_1\Big(\frac{\partial u}{\partial x}+\frac{1}{2}\Big(\frac{\partial w}{\partial x}\Big)^2\Big)-k_5\frac{\partial^2}{\partial x^2}\Big(\frac{\partial u}{\partial x}+\frac{1}{2}\Big(\frac{\partial w}{\partial x}\Big)^2\Big)\Big]\frac{\partial w}{\partial x}\Big\}+k_3\Big(\frac{\partial^2 w}{\partial x^2}-\frac{\partial \psi}{\partial x}\Big) \\ +(k_6-k_7)\frac{\partial^4 w}{\partial x^4}-(2k_6+k_7)\frac{\partial^3\psi}{\partial x^3}+F(x,t)+\frac{1}{2}\frac{\partial C(x,t)}{\partial x}=\rho A\frac{\partial^2 w}{\partial t^2}, \tag{16b}$$

$$k_2\frac{\partial^2\psi}{\partial x^2}+k_3\Big(\frac{\partial w}{\partial x}-\psi\Big)-k_4\frac{\partial^4\psi}{\partial x^4}+(k_7-2k_6)\frac{\partial^3 w}{\partial x^3}+(k_7+4k_6)\frac{\partial^2\psi}{\partial x^2}-\frac{C(x,t)}{2}=\rho I\frac{\partial^2\psi}{\partial t^2}, \tag{16c}$$

and the boundary conditions:

$$\Big(N_0+k_1\Big(\frac{\partial u}{\partial x}+\frac{1}{2}\Big(\frac{\partial w}{\partial x}\Big)^2\Big)-k_5\frac{\partial^2}{\partial x^2}\Big(\frac{\partial u}{\partial x}+\frac{1}{2}\Big(\frac{\partial w}{\partial x}\Big)^2\Big)-\hat{N}\Big)\Big|_{x=0,L}=0 \quad\text{or}\quad \delta u\big|_{x=0,L}=0,$$

$$\Big(k_2\frac{\partial\psi}{\partial x}-k_4\frac{\partial^3\psi}{\partial x^3}+(k_7-2k_6)\frac{\partial^2 w}{\partial x^2}+(k_7+4k_6)\frac{\partial\psi}{\partial x}-\hat{M}_\sigma\Big)\Big|_{x=0,L}=0 \quad\text{or}\quad \delta\psi\big|_{x=0,L}=0,$$

$$\left(N_0+k_1\left(\frac{\partial u}{\partial x}+\frac{1}{2}\left(\frac{\partial w}{\partial x}\right)^2\right)-k_5\frac{\partial^2}{\partial x^2}\left(\frac{\partial u}{\partial x}+\frac{1}{2}\left(\frac{\partial w}{\partial x}\right)^2\right)\right)\frac{\partial w}{\partial x}$$
$$+k_3\left(\frac{\partial w}{\partial x}-\psi\right)-(k_6+k_7)\frac{\partial^3 w}{\partial x^3}+(2k_6-k_7)\frac{\partial^2\psi}{\partial x^2}+\frac{C(x,t)}{2}-\hat{V}\bigg|_{x=0,L}=0 \quad\text{or}\quad \delta w\big|_{x=0,L}=0,$$
$$\left(k_5\frac{\partial}{\partial x}\left(\frac{\partial u}{\partial x}+\frac{1}{2}\left(\frac{\partial w}{\partial x}\right)^2\right)-\hat{P}\right)\bigg|_{x=0,L}=0 \quad\text{or}\quad \delta\left(\frac{\partial u}{\partial x}+\frac{1}{2}\left(\frac{\partial w}{\partial x}\right)^2\right)\bigg|_{x=0,L}=0,$$
$$\left(k_4\frac{\partial^2\psi}{\partial x^2}-\hat{Q}\right)\bigg|_{x=0,L}=0 \quad\text{or}\quad \delta\left(\frac{\partial\psi}{\partial x}\right)\bigg|_{x=0,L}=0,$$
$$\left((k_6+k_7)\frac{\partial^2 w}{\partial x^2}+(k_7-2k_6)\frac{\partial\psi}{\partial x}-\hat{M}_M\right)\bigg|_{x=0,L}=0 \quad\text{or}\quad \delta\left(\frac{\partial w}{\partial x}\right)\bigg|_{x=0,L}=0.$$

Consequently, on the basis of the strain gradient theory the governing equations of motion of a nonlinear size-dependent Timoshenko beam are achieved. Neglecting the nonlinear terms, body forces, body couples, and boundary surface tractions in (16b) and (16c), these equations can be reduced to those given by [Wang et al. 2010]. In the cases associated with a thin beam with a huge aspect ratio, same as in the classical beam theories, Poisson's effect is no more effective and can be negligible, that is, $\nu=0$; but in other cases it must be considered to get reliable outcomes. Letting the material length-scale parameters l_0, l_1, and l_2 equal zero, the governing equations and corresponding boundary conditions related to a nonlinear Timoshenko beam modeled by classical beam theory will be achieved. Moreover, the governing equations and boundary conditions of a nonlinear Timoshenko beam modeled via the modified couple stress theory can be achieved if only $l_0=l_1=0$ and $l_2=l$ (see [Asghari et al. 2010b]). Additionally, by neglecting the shear deformation, governing equations and boundary conditions corresponding to the microscale Euler–Bernoulli beam model based on the strain gradient elasticity theory will be attained (see [Kahrobaiyan et al. 2011]).

4. Governing equations of motion of a simply supported beam with immovable ends and corresponding boundary conditions: A specific case

Herein, specifically simply supported beams with immobile ends are considered and the strain gradient formulation of the earlier section is developed for this case. The relevant boundary conditions are

$$u(0,t)=u(L,t)=0 \quad\text{and}\quad w(0,t)=w(L,t)=0. \tag{17}$$

We assume $\hat{P}$, $\hat{Q}$, $\hat{M}_\sigma$, and $\hat{M}_M$ are zero at the end sections. Accordingly, the other boundary conditions can be obtained as follows:

$$\frac{\partial}{\partial x}\left(\frac{\partial u}{\partial x}+\frac{1}{2}\left(\frac{\partial w}{\partial x}\right)^2\right)\bigg|_{x=0,L}=0, \tag{18a}$$
$$\left(k_2\frac{\partial\psi}{\partial x}-k_4\frac{\partial^3\psi}{\partial x^3}+(k_7-2k_6)\frac{\partial^2 w}{\partial x^2}+(k_7+4k_6)\frac{\partial\psi}{\partial x}\right)\bigg|_{x=0,L}=0, \tag{18b}$$
$$\left((k_6+k_7)\frac{\partial^2 w}{\partial x^2}+(k_7-2k_6)\frac{\partial\psi}{\partial x}\right)\bigg|_{x=0,L}=0, \quad \left(\frac{\partial\psi}{\partial x}\right)\bigg|_{x=0,L}=0. \tag{18c}$$

Compared to the inertia term in the transverse direction, the horizontal inertia force can be neglected [Asghari et al. 2010b]. Considering this assumption and assuming N_0 independent of x, in the absence of axial body forces (that is, $G(x,t)=0$), the equation of motion in the axial direction (16a) and the boundary condition (18a) give

$$k_1\left(\frac{\partial u}{\partial x}+\frac{1}{2}\left(\frac{\partial w}{\partial x}\right)^2\right)+N_0=N(t). \tag{19}$$

In the case of axially immobile ends ($u(0,t)=u(L,t)=0$), integrating (19) between the limits 0 and L leads to

$$N(t)=N_0+\tilde{N}(t)=N_0+\frac{k_1}{2L}\int_0^L\left(\frac{\partial w}{\partial x}\right)^2 dx. \tag{20}$$

The axial force variation in the beam with respect to the initial configuration is denoted by $\tilde{N}(t)$ and is indeed due to the extension resulting from the transverse deformation. Inserting (20) into (16b), the equations of motion can be rewritten in the following form:

$$N\frac{\partial^2 w}{\partial x^2}+k_3\left(\frac{\partial^2 w}{\partial x^2}-\frac{\partial \psi}{\partial x}\right)+(k_6-k_7)\frac{\partial^4 w}{\partial x^4}-(2k_6+k_7)\frac{\partial^3 \psi}{\partial x^3}+F(x,t)+\frac{1}{2}\frac{\partial C(x,t)}{\partial x}=\rho A\frac{\partial^2 w}{\partial t^2}. \tag{21}$$

The governing equations of the dynamic behavior of a nonlinear size-dependent Timoshenko beam with two immobile ends modeled on the basis of strain gradient theory are represented in (16c) and (21) and the associated boundary conditions are given by $w(0,t)=w(L,t)=0$ and by (18b)–(18c). If the material length-scale parameters l_0, l_1, and l_2 are set to be zero, the governing equations and corresponding boundary conditions of a nonlinear Timoshenko beam with immobile supports modeled by classical beam theory will be attained (see [Ansari and Ramezannezhad 2011]). Furthermore, to achieve the governing equations and boundary conditions of a nonlinear Timoshenko beam with two immobile supports modeled by modified couple stress theory, it is enough to let $l_0=l_1=0$ and $l_2=l$.

5. Investigation of the free vibration of a simply supported beam

Herein, as an example, based on strain gradient theory, the free vibration of nonlinear size-dependent Timoshenko beams with simply supported boundary conditions and immovable ends under the assumption $N_0=F=C=0$ are investigated.

For beams with simply supported edges, the solutions of the governing equations can be introduced as $\psi(x,t)=\Psi(t)\cos(m\pi x/L)$ and $w(x,t)=W(t)\sin(m\pi x/L)$. Inserting these solutions into (16c) and (21) results in

$$\ddot{W}+\frac{\pi^4 m^4(\lambda+2\mu)}{4\rho L^4}W^3+\left(\frac{k_s\mu\pi^2 m^2}{\rho L^2}-\frac{8\mu l_1^2\pi^4 m^4}{15\rho L^4}+\frac{\mu l_2^2\pi^4 m^4}{4\rho L^4}\right)W \\ +\left(\frac{16\mu l_1^2\pi^3 m^3}{15\rho L^3}-\frac{k_s\mu m\pi}{\rho L}+\frac{\mu l_2^2\pi^3 m^3}{\rho L^3}\right)\Psi=0, \tag{22a}$$

$$\ddot{\Psi}+\left(\frac{\pi^2m^2(\lambda+2\mu)}{\rho L^2}+\frac{2\mu A\pi^2m^2l_0^2}{\rho IL^2}+\frac{k_s\mu A}{\rho I}+\frac{2\mu l_0^2\pi^4m^4}{\rho L^4}+\frac{4\mu l_1^2\pi^4m^4}{5\rho L^4}+\frac{32\mu Al_1^2\pi^2m^2}{15\rho IL^2}+\frac{\mu Al_2^2\pi^2m^2}{4\rho IL^2}\right)\Psi \\ +\left(\frac{\mu Al_2^2\pi^3m^3}{4\rho IL^3}-\frac{k_s\mu Am\pi}{\rho IL}-\frac{16\mu Al_1^2\pi^3m^3}{15\rho IL^3}\right)W=0. \quad (22b)$$

The governing equations must be expressed in nondimensional form by using the following nondimensional parameters:

$$\omega_l=\sqrt{\frac{\pi^2(\lambda+2\mu)}{\rho L^2}},\qquad \omega_s=\sqrt{\frac{k_s\mu A}{\rho I}},\qquad \omega_r=\sqrt{\frac{\pi^2k_s\mu}{\rho L^2}}, \\ \omega_m=\sqrt{\frac{\mu\pi^2}{\rho L^2}},\qquad \omega_n=\sqrt{\frac{\mu A}{\rho I}},\qquad (\alpha_0,\alpha_1,\alpha_2)=\frac{\pi^2}{4L^2}(l_0^2,l_1^2,l_2^2),\qquad \tau=\omega t. \quad (23)$$

In order to achieve an accurate analytical solution, the nonlinear equations resulting from (22) are solved utilizing the harmonic balance method. According to this method, the solutions are assumed as a truncated Fourier series of the form [Gao and Lei 2009]

$$W(\tau)=\Gamma_1\cos\tau+\Gamma_1\cos 3\tau,\qquad \Psi(\tau)=\Lambda_1\cos\tau+\Lambda_2\cos 3\tau. \quad (24a)$$

Inserting the given solution into (22), substituting the above Fourier series, ignoring the higher-order harmonics than ones comprised in the original assumed solutions and setting the coefficients of like cosine harmonics (such as the $\cos\tau$ and $\cos 3\tau$ terms) equal to zero, a set of algebraic equations will be achieved as follows:

$$-\omega^2\frac{\Gamma_1}{L}+\left(m^4\alpha_2\omega_m^2+m^2\pi\omega_r^2-\frac{32m^4}{15}\alpha_1\omega_m^2\right)\frac{\Gamma_1}{L}+\left(\frac{4m^3\alpha_2}{\pi}\omega_m^2+\frac{64\alpha_1m^3}{15\pi}\omega_m^2-\frac{m\omega_r^2}{\pi}\right)\Lambda_1 \\ +\frac{\pi^2m^4\omega_l^2}{4L^3}\left(\frac{3}{4}\Gamma_1^3+\frac{3}{4}\Gamma_1^2\Gamma_2+\frac{3}{2}\Gamma_2^2\Gamma_1\right)=0, \quad (25a)$$

$$-\omega^2\Lambda_1+\left(m^2\omega_l^2+8m^2\alpha_0\omega_n^2+\omega_s^2+8m^4\alpha_0\omega_m^2+\frac{16}{5}m^4\alpha_1\omega_m^2+\frac{128m^2}{15}\alpha_1\omega_n^2+m^2\alpha_2\omega_n^2\right)\Lambda_1 \\ +\left(\pi m^3\alpha_2\omega_n^2-m\pi\omega_s^2-\frac{64\pi m^3}{15}\alpha_1\omega_n^2\right)\frac{\Gamma_1}{L}=0, \quad (25b)$$

$$-9\omega^2\frac{\Gamma_2}{L}+\left(m^4\alpha_2\omega_m^2+m^2\pi\omega_r^2-\frac{32m^4}{15}\alpha_1\omega_m^2\right)\frac{\Gamma_2}{L}+\left(\frac{4m^3\alpha_2}{\pi}\omega_m^2+\frac{64\alpha_1m^3}{15\pi}\omega_m^2-\frac{m\omega_r^2}{\pi}\right)\Lambda_2 \\ +\frac{\pi^2m^4\omega_l^2}{4L^3}\left(\frac{1}{4}\Gamma_1^3+\frac{3}{2}\Gamma_1^2\Gamma_2+\frac{3}{4}\Gamma_2^3\right)=0, \quad (25c)$$

$$-9\omega^2\Lambda_1+\left(m^2\omega_l^2+8m^2\alpha_0\omega_n^2+\omega_s^2+8m^4\alpha_0\omega_m^2+\frac{16}{5}m^4\alpha_1\omega_m^2+\frac{128m^2}{15}\alpha_1\omega_n^2+m^2\alpha_2\omega_n^2\right)\Lambda_2 \\ +\left(\pi m^3\alpha_2\omega_n^2-m\pi\omega_s^2-\frac{64\pi m^3}{15}\alpha_1\omega_n^2\right)\frac{\Gamma_2}{L}=0. \quad (25d)$$

Utilizing the Newton–Raphson method, these nonlinear equations can be solved for ω, Λ_1, Λ_2, and Γ_2 by choosing Γ_1 as a determined parameter.

A microbeam made of epoxy with mechanical properties $E = 1.44\,\text{GPa}$ and $\rho = 1.22 \times 10^3\,\text{kg/m}^3$ [Maneschy et al. 1986] is considered under the assumption $l_0 = l_1 = l_2 = l = 17.6\,\mu\text{m}$ [Ma et al. 2008; Kong et al. 2009]. The shear coefficient k_s is given as $(5+5\nu)/(6+5\nu)$ which is assessed as the most efficient description for a rectangular cross-section beam [Ke et al. 2012].

As was mentioned, if the material length-scale parameters are set as $l_0 = l_1 = 0$ and $l_2 = l$ and the nonlinearity is neglected, the linear free vibration of the homogeneous microbeams presented in [Ma et al. 2008] can be degenerated. To check the validity and accuracy of the present analysis, the first four natural frequencies of a simply supported Timoshenko microbeam with $E = 1.44\,\text{GPa}$, $\rho = 1.22 \times 10^3\,\text{kg/m}^3$, $L/h = 10$, and $l = 17.6\,\mu\text{m}$ obtained from the present analysis are compared with those of Ma et al., given in Table 1. As can be seen from the table, a good agreement has been achieved. The small difference between our results and those of Ma et al. is due to considering the Poisson effect. We observe that these differences become really significant at lower l/h and higher modes.

Table 2 compares the results obtained with the present method, based on classical, modified couple stress, and strain gradient theories, with those reported in [Ansari et al. 2011] for the same theories. As in that paper, we report the dimensionless natural frequencies, $\Omega = \omega L\sqrt{\rho_m/(\lambda_m + 2\mu_m)}$, of simply supported homogeneous metal (Al) and ceramic (SiC) microbeams with material properties $E_m = 70\,\text{GPa}$, $\nu_m = 0.3$, and $\rho_m = 2702\,\text{kg/m}^3$ for Al and $E_c = 427\,\text{GPa}$, $\nu_c = 0.17$, and $\rho_c = 3100\,\text{kg/m}^3$ for SiC. The other parameters used are $L/h = 10$, $h/l = 2$, and $l = 15\,\mu\text{m}$. Excellent agreement can be observed between the present results and the earlier ones.

Table 3 gives the nonlinear frequency ratios for simply supported homogeneous microbeams with the material properties $E = 70\,\text{GPa}$, $\rho = 2702\,\text{kg/m}^3$, and $\nu = 0.3$ [Ke et al. 2012] based on modified couple stress theory. The results of Ke et al. are also provided for comparison. The other parameters used in the example are $L/h = 12$, $h/l = 2$, and $l = 15\,\mu\text{m}$ [Ke et al. 2012]. Excellent agreement can be observed

Mode	$h/l = 1$		$h/l = 3$		$h/l = 10$	
	present	Ma et al.	present	Ma et al.	present	Ma et al.
1	0.6733	0.6723	0.1393	0.1391	0.0377	0.0377
2	2.4643	2.4530	0.5182	0.5163	0.1402	0.1396
3	4.9741	4.9368	1.0588	1.0519	0.2858	0.2838
4	7.9372	7.8606	1.6966	1.6814	0.4557	0.4514

Table 1. Comparison of the first four linear natural frequencies (in MHz) of microbeams with consideration of size effect. Literature results are from [Ma et al. 2008].

Theory	Ceramic		Metal	
	present	previous	present	previous
Classical	0.5778	0.5776	0.2810	0.2854
Modified couple stress	0.8541	0.8538	0.3820	0.3863
Strain gradient	1.2705	1.2608	0.5471	0.5430

Table 2. Comparison of the dimensionless natural frequencies of microbeams corresponding to different beam models. “Previous” refers to results from [Ansari et al. 2011].

	$\Omega_{\text{Linear}} = \omega L\sqrt{\rho/E}$	Nonlinear frequency ratio		
		$w_{\max}/h = 0.2$	$w_{\max}/h = 0.4$	$w_{\max}/h = 0.6$
present	0.3187	1.0338	1.1259	1.2654
[Ke et al. 2012]	0.3186	1.0340	1.1265	1.2671

Table 3. Comparison of the dimensionless natural frequency and nonlinear frequency ratios of microbeams.

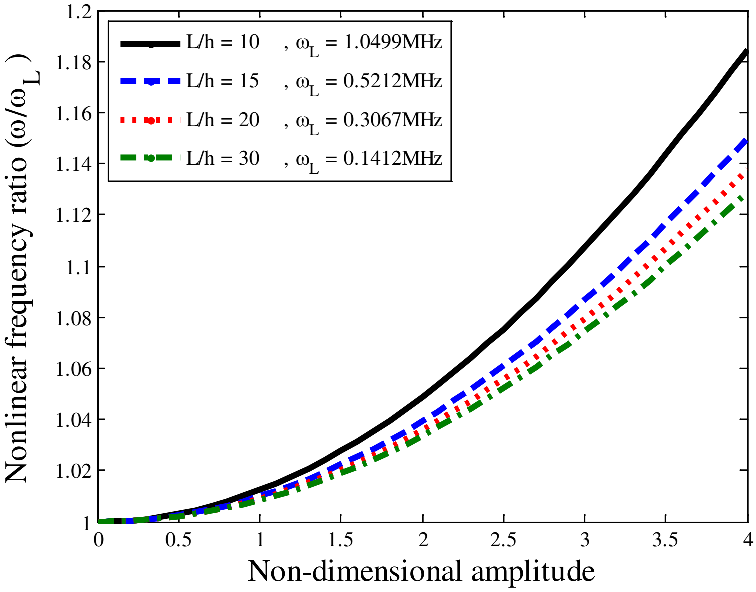

Figure 2. Effect of the length-to-thickness ratio (L/h) on the nonlinear frequency ratio, for $h = l$ and $b = 2h$.

between our results and those of Ke et al.

The nonlinear free vibration of a simply supported beam is investigated in Figures 2–6. The linear fundamental frequencies (ω_L) are also given in Figures 2–5. Figure 2 illustrates the nonlinear frequency ratio versus the vibration amplitude for different length-to-thickness ratios for the geometric parameters $h = l$, $b = 2h$. It is seen that the beam exhibits a typical hard-spring behavior, that is, the nonlinear frequency ratio increases as the vibration amplitude increases. The length-to-thickness ratio has a significant effect on the nonlinear vibration behavior. At a given vibration amplitude, both the linear frequency and nonlinear frequency ratios decrease with the increase of the length-to-thickness ratio.

The effect of the ratio of the beam thickness to the material length-scale parameter (h/l) on the nonlinear frequency ratio is investigated in Figure 3. This figure is illustrated for the geometric parameters $b = 2h$ and $L = 20h$ and reveals that as the ratio h/l increases, unlike for the linear frequency, the nonlinear frequency ratio gets bigger. At higher amplitudes, the discrepancy between the curves becomes more prominent.

Figure 4 depicts the Poisson's ratio's influence on the linear and nonlinear frequencies for two different geometric parameters. For the case of $h = l$, $b = 2h$, and $L = 30h$, an increase in the Poisson's ratio

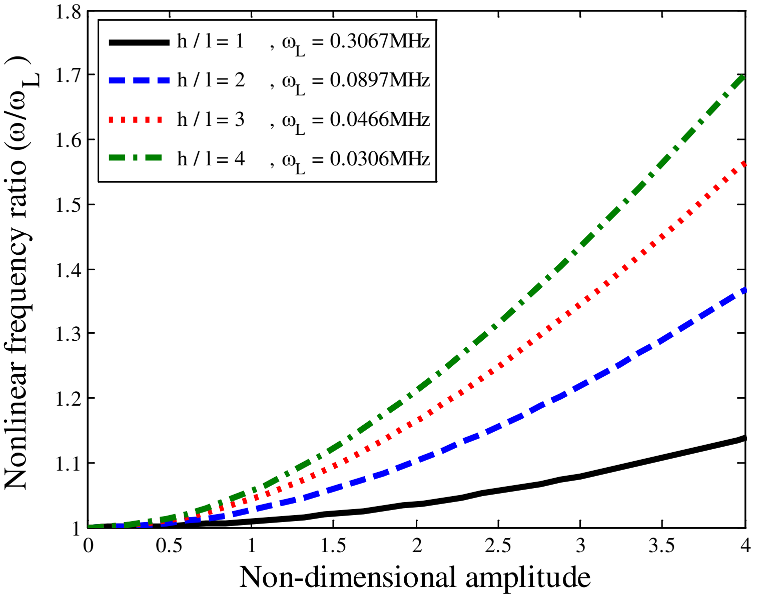

Figure 3. Effect of the ratio of the beam thickness to the material length scale parameter (h/l) on the nonlinear frequency ratio, for $b = 2h$ and $L = 20h$.

leads to lower linear frequencies while the nonlinear frequency ratio becomes higher. In addition, for the geometric parameters $h = 3l$, $b = 2h$, and $L = 20h$, an increase in the Poisson's ratio results in higher nonlinear frequency ratios but results in unpredictable behavior of the linear frequency. This indicates that the size effect plays a key role in the investigation of the effect of Poisson's ratio on the natural frequency of microbeams.

Figure 5 illustrates the influences of additional material parameters on the nonlinear frequency ratio. The figure is plotted for the nonlinear frequency ratio versus the nondimensional amplitude for $h = 2l$, $b = 2h$, $L = 10h$, and $\nu = 0.38$. As the figure indicates, the value of the nonlinear frequency ratio predicted by classical beam theory is more than that of the nonclassical beam theories. Also, according to the figure, strain gradient beam theory predicts the lowest nonlinear frequency ratio. In other words, the modified couple stress and classical beam theories tend to overestimate the nonlinear frequency ratio, especially when the amplitude gets higher. Furthermore, as the amplitude rises, the deviation between the theories becomes more prominent.

Another comparison between the classical and nonclassical beam theories is illustrated in Figure 6, but this time the figure shows the natural frequency of a microbeam assessed by the nonclassical and classical theories for two different Poisson's ratios. The trends are illustrated for a nondimensional vibrational amplitude $(w_{\max}/\sqrt{I/A})$ equal to 3. This figure indicates that the natural frequencies obtained by the nonclassical Timoshenko beam models are higher than the ones predicted by the classical model for both Poisson's ratios. The natural frequencies predicted by the strain gradient model are higher than those from the modified couple stress model. In other words, apart from strain gradient theory, the theories mentioned tend to underestimate the natural frequency. In addition, as can be deduced from this figure, for the classical beam model, the natural frequency with $\nu = 0$ is always lower than that with $\nu = 0.38$.

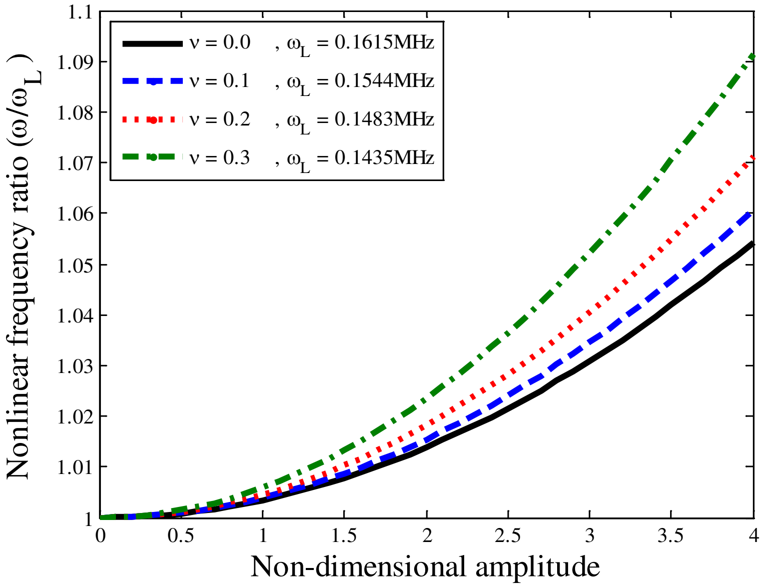

(a): $h = l$, $b = 2h$, $L = 30h$

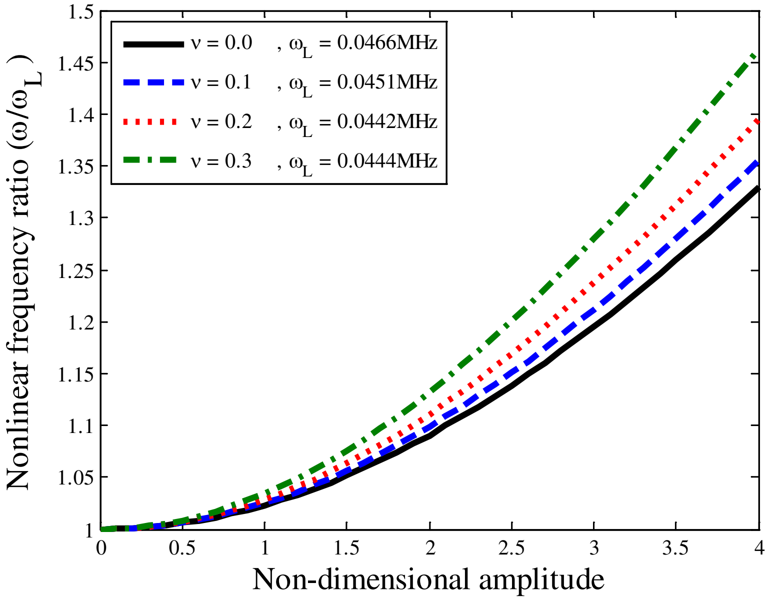

(b): $h = 3l$, $b = 2h$, $L = 20h$

Figure 4. Influence of the Poisson's ratio on the nonlinear frequency ratio for the given values of h, b, and L.

However, for the nonclassical beam theories, this is not true at low h/l. At low and high h/l, with an increase of the Poisson's ratio, the microbeam natural frequency corresponding to the nonclassical beam models decreases and increases, respectively. According to this figure, it can be concluded that the Poisson effect is more prominent at low thickness ratios. Hence, the reliability of the beam theories

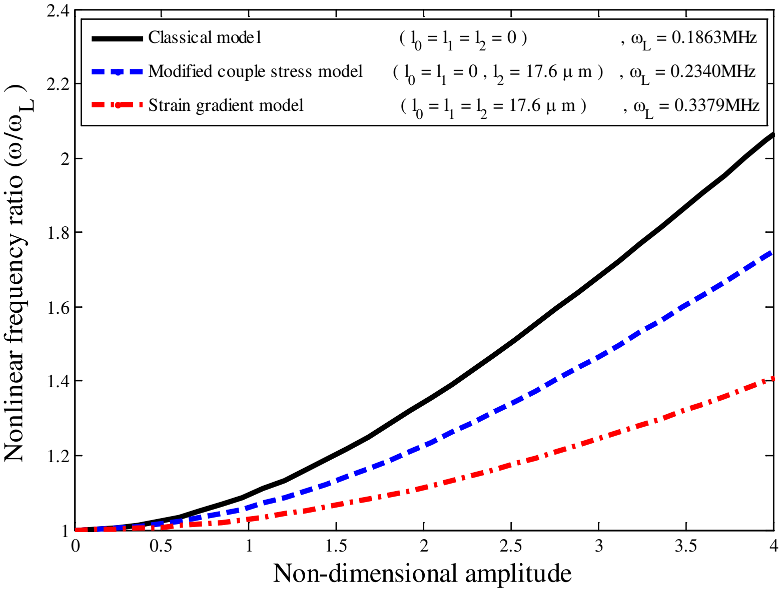

Figure 5. Comparison between classical and nonclassical beam theories and the influence of additional material parameters on the nonlinear frequency ratio, for $h = 2l$, $b = 2h$, $L = 10h$, and $\nu = 0.38$.

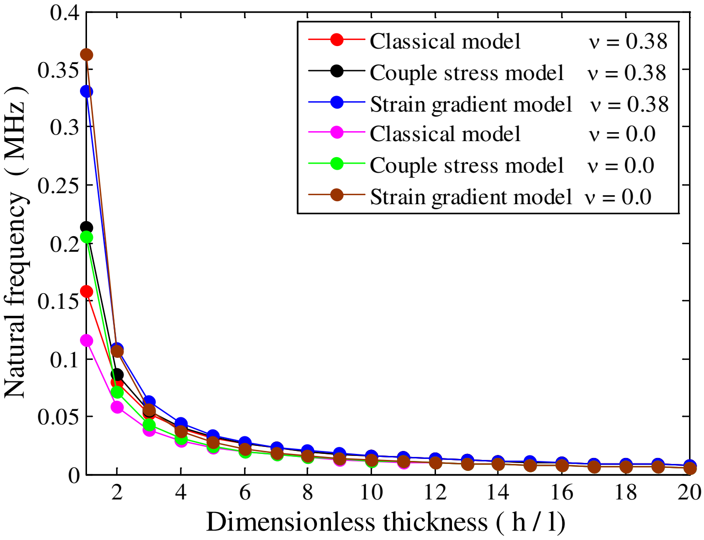

Figure 6. Nonlinear frequency versus the dimensionless thickness corresponding to two different values of Poisson's ratio and the classical and nonclassical beam theories, for $b = 2h$ and $L = 20h$.

which neglect the Poisson effect is questionable, so in order to obtain more accurate results, this effect must be incorporated.

6. Conclusion

Based on strain gradient theory and using Hamilton's principle, a comprehensive geometrically nonlinear size-dependent Timoshenko beam model incorporating the Poisson effect was developed. The model contains the nonlinear governing partial differential equations of motions and the corresponding classical and nonclassical boundary conditions. The current nonclassical Timoshenko beam model encompasses the available modified couple stress and classical models and recovers the nonclassical Euler–Bernoulli beam model when $\psi = \partial w/\partial x$. As a specific case, the governing equations and the corresponding boundary conditions were solved by the use of the harmonic balance method to describe the large-amplitude size-dependent vibration behavior of simply supported microbeams. The numerical results obtained from the present model were compared with previously published results, from the linear strain gradient and the nonlinear and linear modified couple stress theories, as well as linear and nonlinear classical models, showing good agreement.

References

[Aifantis 1999] E. C. Aifantis, "Strain gradient interpretation of size effects", *Int. J. Fract.* **95** (1999), 299–314.

[Ansari and Ramezannezhad 2011] R. Ansari and H. Ramezannezhad, "Nonlocal Timoshenko beam model for the large-amplitude vibrations of embedded multiwalled carbon nanotubes including thermal effects", *Physica E* **43** (2011), 1171–1178.

[Ansari et al. 2011] R. Ansari, R. Gholami, and S. Sahmani, "Free vibration analysis of size-dependent functionally graded microbeams based on the strain gradient Timoshenko beam theory", *Compos. Struct.* **94** (2011), 221–228.

[Asghari et al. 2010a] M. Asghari, M. T. Ahmadian, M. H. Kahrobaiyan, and M. Rahaeifard, "On the size-dependent behavior of functionally graded micro-beams", *Mater. Des.* **31** (2010), 2324–2329.

[Asghari et al. 2010b] M. Asghari, M. H. Kahrobaiyan, and M. T. Ahmadian, "A nonlinear Timoshenko beam formulation based on the modified couple stress theory", *Int. J. Eng. Sci.* **48** (2010), 1749–1761.

[Coutu et al. 2004] R. A. Coutu, P. E. Kladitis, L. A. Starman, and J. R. Reid, "A comparison of micro-switch analytic, finite element, and experimental results", *Sens. Actuators, A* **115** (2004), 252–258.

[Craighead 2000] H. G. Craighead, "Nanoelectromechanical systems", *Science* **290** (2000), 1532–1535.

[Eringen 1972] A. C. Eringen, "Nonlocal polar elastic continua", *Int. J. Eng. Sci.* **10** (1972), 1–16.

[Fleck and Hutchinson 1993] N. A. Fleck and J. W. Hutchinson, "Phenomenological theory for strain gradient effects in plasticity", *J. Mech. Phys. Solids* **41** (1993), 1825–1857.

[Fleck and Hutchinson 1997] N. A. Fleck and J. W. Hutchinson, "Strain gradient plasticity", *Adv. Appl. Mech.* **33** (1997), 295–361.

[Fleck and Hutchinson 2001] N. A. Fleck and J. W. Hutchinson, "A reformulation of strain gradient plasticity", *J. Mech. Phys. Solids* **49** (2001), 2245–2271.

[Fleck et al. 1994] N. A. Fleck, G. M. Muller, M. F. Ashby, and J. W. Hutchinson, "Strain gradient plasticity: theory and experiment", *Acta Metall. Mater.* **42** (1994), 475–487.

[Gao and Lei 2009] Y. Gao and F. Lei, "Small scale effects on the mechanical behaviors of protein microtubules based on the nonlocal elasticity theory", *Biochem. Biophys. Res. Commun.* **387** (2009), 467–471.

[Giannakopoulos and Stamoulis 2007] A. E. Giannakopoulos and K. Stamoulis, "Structural analysis of gradient elastic components", *Int. J. Solids Struct.* **44** (2007), 3440–3451.

[Gurtin et al. 1998] M. E. Gurtin, J. Weissmuller, and F. Larche, "The general theory of curved deformable interfaces in solids at equilibrium", *Philos. Mag. A* **78** (1998), 1093–1109.

[Hutchinson 2001] J. R. Hutchinson, "Shear coefficients for Timoshenko beam theory", *J. Appl. Mech.* **68** (2001), 87–92.

[Kahrobaiyan et al. 2011] M. H. Kahrobaiyan, M. Asghari, M. Rahaeifard, and M. T. Ahmadian, "A nonlinear strain gradient beam formulation", *Int. J. Eng. Sci.* **49**:11 (2011), 1256–1267.

[Kaneko 1975] T. Kaneko, "On Timoshenko's correction for shear in vibrating beams", *J. Phys. D: Appl. Phys.* **8** (1975), 1927–1936.

[Ke et al. 2012] L. L. Ke, Y. S. Wang, J. Yang, and S. Kitipornchai, "Nonlinear free vibration of size-dependent functionally graded microbeams", *Int. J. Eng. Sci.* **50**:1 (2012), 256–267.

[Kong et al. 2008] S. Kong, S. Zhou, Z. Nie, and K. Wang, "The size-dependent natural frequency of Bernoulli–Euler microbeams", *Int. J. Eng. Sci.* **46** (2008), 427–437.

[Kong et al. 2009] S. Kong, S. Zhou, Z. Nie, and K. Wang, "Static and dynamic analysis of micro beams based on strain gradient elasticity theory", *Int. J. Eng. Sci.* **47** (2009), 487–498.

[Lam et al. 2003] D. C. C. Lam, F. Yang, A. C. M. Chong, J. Wang, and P. Tong, "Experiments and theory in strain gradient elasticity", *J. Mech. Phys. Solids* **51** (2003), 1477–1508.

[Lazopoulos 2004] K. A. Lazopoulos, "On the gradient strain elasticity theory of plates", *Eur. J. Mech. A-Solid* **23** (2004), 843–852.

[Lazopoulos and Lazopoulos 2010] K. A. Lazopoulos and A. K. Lazopoulos, "Bending and buckling of thin strain gradient elastic beams", *Eur. J. Mech. A-Solid* **29** (2010), 837–843.

[Lun et al. 2006] F. Y. Lun, P. Zhang, F. B. Gao, and H. G. Jia, "Design and fabrication of micro-optomechanical vibration sensor", *Microfabrication Tech.* **120** (2006), 61–64.

[Ma et al. 2008] H. M. Ma, X.-L. Gao, and J. N. Reddy, "A microstructure-dependent Timoshenko beam model based on a modified couple stress theory", *J. Mech. Phys. Solids* **56** (2008), 3379–3391.

[Ma et al. 2010] H. M. Ma, X. L. Gao, and J. N. Reddy, "A non-classical Reddy–Levinson beam model based on a modified couple stress theory", *Int. J. Multiscale Comput. Eng.* **8** (2010), 167–180.

[Ma et al. 2011] H. M. Ma, X. L. Gao, and J. N. Reddy, "A non-classical Mindlin plate model based on a modified couple stress theory", *Acta Mech.* **220** (2011), 217–235.

[Mahdavi et al. 2008] M. H. Mahdavi, A. Farshidianfar, M. Tahani, S. Mahdavi, and H. Dalir, "A more comprehensive modeling of atomic force microscope cantilever", *J. Ultramicroscopy* **109** (2008), 54–60.

[Maneschy et al. 1986] C. E. Maneschy, Y. Miyano, M. Shimbo, and T. C. Woo, "Residual-stress analysis of an epoxy plate subjected to rapid cooling on both surfaces", *Exp. Mech.* **26** (1986), 306–312.

[Mindlin 1965] R. D. Mindlin, "Second gradient of strain and surface tension in linear elasticity", *Int. J. Solids Struct.* **1** (1965), 417–438.

[Mindlin and Tiersten 1962] R. D. Mindlin and H. F. Tiersten, "Effects of couple-stresses in linear elasticity", *Arch. Ration. Mech. Anal.* **11** (1962), 415–448.

[Moghimi Zand and Ahmadian 2009] M. Moghimi Zand and M. T. Ahmadian, "Vibrational analysis of electrostatically actuated microstructures considering nonlinear effects", *Commun. Nonlinear Sci. Numer. Simul.* **14** (2009), 1664–1678.

[Mojahedi et al. 2010] M. Mojahedi, M. Moghimi Zand, and M. T. Ahmadian, "Static pull-in analysis of electrostatically actuated microbeams using homotopy perturbation method", *Appl. Math. Model.* **34** (2010), 1032–1041.

[Papargyri-Beskou et al. 2003b] S. Papargyri-Beskou, K. G. Tsepoura, D. Polyzos, and D. E. Beskos, "Bending and stability analysis of gradient elastic beams", *Int. J. Solids Struct.* **40** (2003b), 385–400.

[Park and Gao 2006] S. K. Park and X. L. Gao, "Bernoulli–Euler beam model based on a modified couple stress theory", *J. Micromech. Microeng.* **16** (2006), 2355–2359.

[Reddy 2003] J. N. Reddy, *Mechanics of laminated composite plates and shells: theory and analysis*, 2nd ed., CRC Press, Boca Raton, FL, 2003.

[Reddy 2007] J. N. Reddy, *Theory and analysis of elastic plates and shells*, 2nd ed., CRC Press, Boca Raton, FL, 2007.

[Scheible et al. 2002] D. V. Scheible, A. Erbe, and R. H. Blick, "Evidence of a nanomechanical resonator being driven into chaotic response via the Ruelle–Takens route", *Appl. Phys. Lett.* **81** (2002), 1884–1886.

[Timoshenko and Goodier 1970] S. P. Timoshenko and J. N. Goodier, *Theory of elasticity*, 3rd ed., McGraw-Hill, New York, 1970.

[Toupin 1962] R. A. Toupin, "Elastic materials with couple-stresses", *Arch. Ration. Mech. Anal.* **11** (1962), 385–414.

[Tsepoura et al. 2002] K. Tsepoura, S. Papargyri-Beskou, D. Polyzos, and D. E. Beskos, "Static and dynamic analysis of a gradient-elastic bar in tension", *Arch. Appl. Mech.* **72** (2002), 483–497.

[Turner et al. 1998] K. L. Turner, S. A. Miller, P. G. Hartwell, N. C. MacDonald, S. H. Strogatz, and S. G. Adams, "Five parametric resonances in a microelectromechanical system", *Nature* **396** (1998), 149–152.

[Vardoulakis and Sulem 1995] I. Vardoulakis and J. Sulem, *Bifurcation analysis in geomechanics*, Blackie/Chapman & Hall, London, 1995.

[Wang et al. 2010] B. Wang, J. Zhao, and S. Zhou, "A micro scale Timoshenko beam model based on strain gradient elasticity theory", *Eur. J. Mech. A. Solids* **29** (2010), 591–599.

[Yang et al. 2002] F. Yang, A. C. M. Chong, D. C. C. Lam, and P. Tong, "Couple stress based strain gradient theory for elasticity", *Int. J. Solids Struct.* **39** (2002), 2731–2743.

Received 7 Sep 2011. Revised 2 Feb 2012. Accepted 17 Feb 2012.

REZA ANSARI: `r_ansari@guilan.ac.ir`
Department of Mechanical Engineering, University of Guilan, P.O. Box 3756, Rasht, Iran

RAHEB GHOLAMI: `rahebgholami@gmail.com`
Department of Mechanical Engineering, University of Guilan, P.O. Box 3756, Rasht, Iran

MOHAMMAD ALI DARABI: `mad.fluid.darabi@gmail.com`
Department of Mechanical Engineering, University of Guilan, P.O. Box 3756, Rasht, Iran

JOURNAL OF MECHANICS OF MATERIALS AND STRUCTURES
Vol. 7, No. 2, 2012

FINITE ELEMENT ANALYSIS OF BENDING-STIFF COMPOSITE CONICAL SHELLS WITH MULTIPLE DELAMINATION

SUDIP DEY AND AMIT KARMAKAR

This paper presents a finite element method to investigate the effects of multiple delaminations on the free-vibration characteristics of graphite-epoxy bending-stiff composite pretwisted shallow conical shells. (We call *bending-stiff* a laminate configuration having maximum stiffness for the spanwise first bending mode.) The generalized dynamic equilibrium equation is derived from Lagrange's equation of motion neglecting the Coriolis effect for moderate rotational speeds. An eight-noded isoparametric plate bending element is employed in the finite element formulation incorporating rotary inertia and the effects of transverse shear deformation based on Mindlin theory. A multipoint constraint algorithm is utilized to ensure the compatibility of deformation and equilibrium of resultant forces and moments at the delamination crack front. The standard eigenvalue problem is solved by applying the QR iteration algorithm. Finite element codes are developed to obtain numerical results concerning the effects of twist angle and rotational speed on the natural frequencies of multiple delaminated bending-stiff composite conical shells. The mode shapes are also depicted for a typical laminate configuration. The numerical results obtained for comparison of single and multiple delaminated bending-stiff composite laminates are the first known nondimensional natural frequencies under the combined effect of rotation and twist for the type of analyses carried out here.

1. Introduction

Composite structures are extensively used in aerospace, automobile, civil, and other various high performance applications. Composite materials are immensely popular in weight-sensitive applications because of their high specific stiffness, low weight, and high strength-to-weight ratio, but one of the major causes of failure in fiber-reinforced laminate composites is the delamination resulting from interlaminar debonding of constituent laminae. Pretwisted composite conical shells with low aspect ratios can be idealized as turbomachinery blades. Prior knowledge of the resonant characteristics of turbomachinery blades is of utmost importance in ensuring a reliably long life for turbine engines. The presence of invisible delamination in such a structural element made of composite materials can be detected with the help of prior knowledge of the natural frequencies if delamination exists. Moreover, the initial stress system in a rotating shell due to centrifugal body forces has appreciable cascading affects on the natural frequency. The vibratory characteristics are thus of critical influence on the performance and safety of such composite structures. In realistic situations, pretwisted conical shell structures have geometrical complexities arising due to their specific applications in various service environments. Hence certain dynamic parameters are to be considered when these structural elements are in rotation, and the finite

---

Keywords: delamination, finite element, vibration, conical shell, bending-stiff.

element method is an efficient tool for the dynamic analysis of such types of applications. Multiple delaminated composite laminated structures exhibit new vibration frequencies depending on the size and location of the delamination. In order to ensure safety of operation, a profound understanding of the dynamic characteristics of composite pretwisted conical shells is essential for designers.

The first established work on pretwisted composite plates [Qatu and Leissa 1991b] determined the natural frequencies of stationary plates using laminated shallow shell theory and the Ritz method. Liew et al. [1994] investigated a pretwisted conical shell to find out the vibratory characteristics of a stationary conical shell by using the Ritz procedure. By using the same method, the first known three-dimensional continuum vibration analysis including full geometric nonlinearities and centrifugal accelerations in composite blades was carried out in [McGee and Chu 1994].

The two important investigations on delamination model were by Shen and Grady [1992] and Krawczuk et al. [1997]. The first dealt with the analytical and experimental determination of natural frequencies of delaminated composite beam while the second one undertook a finite element free vibration analysis of the delaminated composite cantilever beam and plate. Rebière and Gamby [2004] employed a variational approach to model the behavior of composite cross-ply laminates damaged by transverse and longitudinal cracking and delamination, while Aydogdu and Timarci [2003] and Tripathi et al. [2007] studied the free-vibration behavior of a delaminated composite employing the finite element method. Lee et al. [2002] carried out the vibration analysis of a twisted cantilevered conical composite shell using a finite element method based on the Hellinger–Reissner principle, again for single and multiple delaminations. Parhi et al. [2001] and Aymerich et al. [2009] have demonstrated the effects of multiple delamination on laminated composites using FEM. The first dealt with failure analysis of a composite plate due to bending and impact, while the second simulated cross-ply laminates subject to impact based on cohesive interface elements.

As far as the authors are aware, there is no work available in the literature which deals with rotating multiple delaminated composite pretwisted cantilever conical shells by a finite element method considering the combined effect of rotation and twist on the vibration characteristics of the *bending-stiff* configuration $[0°_2/\pm 30°]$s [Crawley 1979]. (We call *bending-stiff* a laminate configuration having maximum stiffness for the spanwise first bending mode in terms of design compliance.) Turbomachinery blades may flutter due to high-speed rotation which may lead to fouling of the blades in the cantilevered arrangements. Although the free ends of the blades are restrained by lacing wire, in resonant condition, excessive vibration may lead to severe damage of the vibratory blades. This can be prevented to a great extent provided the blades have high stiffness against spanwise bending. In this paper, the multipoint constraint algorithm [Gim 1994] is incorporated which leads to asymmetric element stiffness matrices. The QR iteration algorithm [Bathe 1990] is utilized to solve the standard eigenvalue problem. The present analysis is aimed at obtaining the nondimensional fundamental frequency (NDFF) and nondimensional second natural frequencies (NDSF) of pretwisted bending-stiff composite shallow conical shells having delamination without taking care of the effect of dynamic contact between delaminated layers.

In the present study, the shell surface is considered as a shallow conical shell with length L, reference width b_0, thickness h, vertex angle θ_v, and base subtended angle of cone θ_0 as depicted in Figure 1. Since the conical shell is shallow, it may be assumed that the cross section is elliptical. The component of radius of curvature in the chord-wise direction $R_y(x, y)$ is a parameter varying both in the x and y-directions. The variation in the x-direction is linear. There is no curvature along the spanwise direction ($R_x = \infty$).

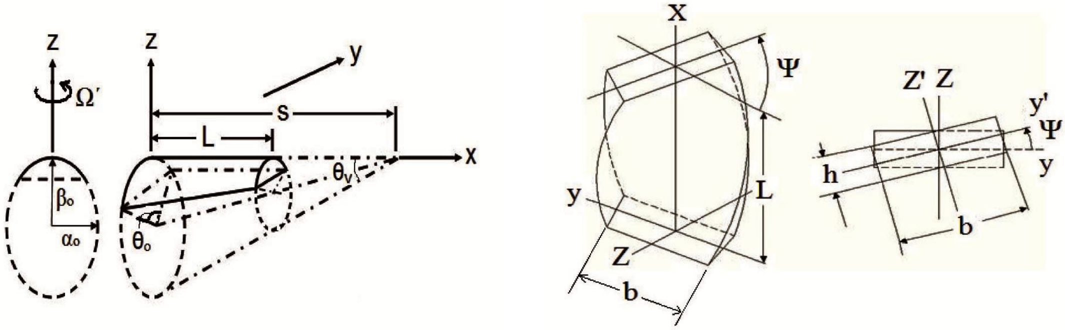

Figure 1. Geometry of an untwisted conical shell (left) and a twisted plate (right).

The cantilever shell, clamped along $x = 0$, is pretwisted with radius of twist R_{xy} as shown in the figure. Thus a pretwisted shallow conical shell of uniform thickness, made of laminated composite is considered.

2. Mathematical formulation

A shallow shell is characterized by its middle surface which is defined by the equation [Leissa et al. 1984]

$$z = -\tfrac{1}{2}\left[\frac{x^2}{R_x} + 2\frac{xy}{R_{xy}} + \frac{y^2}{R_y}\right], \tag{1}$$

where R_x and R_y denote the radii of curvature in the x and y-directions, respectively. The radius of twist (R_{xy}), length (L) of shell, and twist angle (ψ) are related as

$$\tan\psi = -\frac{L}{R_{xy}}. \tag{2}$$

The dynamic equilibrium equation for moderate rotational speeds neglecting the Coriolis effect is derived employing Lagrange's equation of motion. The equation in global form is expressed as [Karmakar and Sinha 2001]

$$[M]\{\ddot{\delta}\} + ([K] + [K_\sigma])\{\delta\} = \{F(\Omega^2)\}, \tag{3}$$

where $[M]$, $[K]$, and $[K_\sigma]$ are the global mass, elastic stiffness, and geometric stiffness matrices, respectively. $\{F(\Omega^2)\}$ is the nodal equivalent centrifugal force and $\{\delta\}$ is the global displacement vector. $[K_\sigma]$ depends on the initial stress distribution and is obtained by the iterative procedure upon solving

$$([K] + [K_\sigma])\{\delta\} = \{F(\Omega^2)\}. \tag{4}$$

The natural frequencies (ω_n) are determined from the standard eigenvalue problem [Bathe 1990], which is represented below and is solved by the QR iteration algorithm:

$$[A]\{\delta\} = \lambda\{\delta\}, \tag{5}$$

where

$$[A] = ([K] + [K_\sigma])^{-1}[M] \quad \text{and} \quad \lambda = 1/\omega_n^2. \tag{6}$$

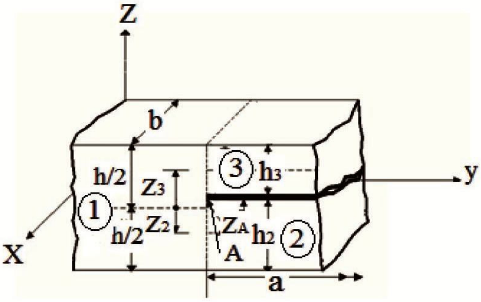

Figure 2. Plate elements at a delamination crack tip.

3. Multipoint constraint

Figure 2 represents the cross-sectional view of a typical delamination crack tip [Gim 1994] where nodes of three plate elements meet together to form a common node. The undelaminated region is modeled by plate element 1 of thickness h, and the delaminated region is modeled by plate elements 2 and 3 whose interface contains the delamination (h_2 and h_3 are the thicknesses of elements 2 and 3, respectively). Elements 1, 2, and 3 are freely allowed to deform prior to imposition of the constraint conditions. The plate elements at a delamination crack front are shown in Figure 3. The nodal displacements of elements 2 and 3 at the crack tip are expressed as

$$U_j = U'_j - (Z - Z'_j)\theta_{xj}, \quad V_j = V'_j - (Z - Z'_j)\theta_{yj}, \quad W_j = W'_j \quad (j = 2, 3), \tag{7}$$

where U'_j, V'_j, and W'_j are the midplane displacements, Z'_j is the z-coordinate of the midplane of element j, and θ_x and θ_y are the rotations about x and y-axes, respectively. The above equation also holds good for element 1 and Z'_1 equal to zero. The transverse displacements and rotations at a common node have values expressed as

$$W_1 = W_2 = W_3 = W, \quad \theta_{x1} = \theta_{x2} = \theta_{x3} = \theta_x, \quad \theta_{y1} = \theta_{y2} = \theta_{y3} = \theta_y. \tag{8}$$

(See [Gim 1994] for Equations (8)–(13).) The in-plane displacements of all three elements at the crack tip are equal and they are related as

$$U'_2 = U'_1 - Z'_2\theta_x, \quad \text{and} \quad V'_2 = V'_1 - Z'_2\theta_y, \tag{9}$$

$$U'_3 = U'_1 - Z'_3\theta_x, \quad \text{and} \quad V'_3 = V'_1 - Z'_3\theta_y, \tag{10}$$

where U'_1 is the midplane displacement of element 1. Equations (8)–(10) relating the nodal displacements and rotations of elements 1, 2, and 3 at the delamination crack tip are the multipoint constraint equations used in the finite element formulation to satisfy the compatibility of the displacements and rotations. The midplane strains between elements 2 and 3 are related as

$$\{\epsilon'\}_j = \{\epsilon'\}_j + Z'_j\{k\}, \tag{11}$$

where $\{\epsilon'\}$ represents the strain vector and $\{k\}$ is the curvature vector, which is identical at the crack tip for elements 1, 2, and 3. This equation can be considered as a special case for element 1 and Z'_1 equal

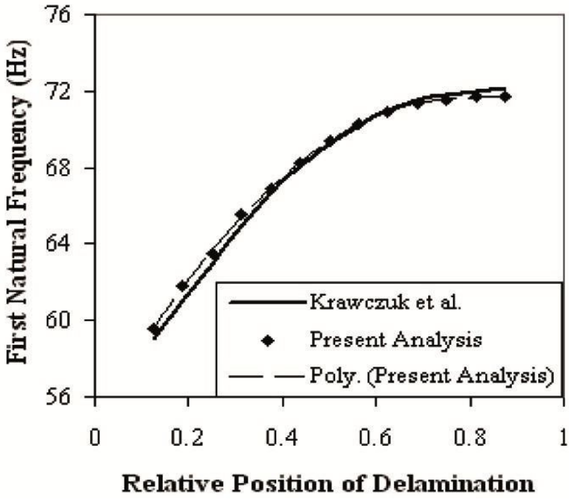

Figure 3. Influence of the relative position of delamination on the first natural frequency of the composite cantilever beam [Krawczuk et al. 1997].

to zero. The in-plane stress-resultants, $\{N\}$, and moment resultants, $\{M\}$, of elements 2 and 3 can be expressed as

$$\{N\}_j = [A]_j\{\epsilon'\}_1 + (Z'_j[A]_j + [B]_j)\{k\}, \tag{12}$$

$$\{M\}_j = [B]_j\{\epsilon'\}_1 + (Z'_j[B]_j + [D]_j)\{k\}. \tag{13}$$

The resultant forces and moments at the delamination front for elements 1, 2, and 3 satisfy the following equilibrium conditions:

$$\{N\} = \{N\}_1 = \{N\}_2 + \{N\}_3, \tag{14}$$

$$\{M\} = \{M\}_1 = \{M\}_2 + \{M\}_3 + Z'_2\{N\}_2 + Z'_3\{N\}_3, \tag{15}$$

$$\{Q\} = \{Q\}_1 = \{Q\}_2 + \{Q\}_3, \tag{16}$$

where $\{Q\}$ denotes the transverse shear resultants.

In the finite element analysis the structure has to be discretized into a number of elements connected at the nodal points. The element shall be such that it can properly define the behavior of the structure. In the present analysis an eight-noded quadratic isoparametric element with five degrees of freedom at each node (three translational and two rotational) is employed. The quadrilateral element has four corner nodes and four midside nodes. The isoparametric plate bending element shall be oriented in the natural coordinate system wherein the shape functions are as follows [Bathe 1990]:

$$N_i = (1+\epsilon\epsilon_i)(1+\eta\eta_i)(\epsilon\epsilon_i+\eta\eta_i-1)/4 \qquad (\text{for } i = 1,\dots,4), \tag{17}$$

$$N_i = (1-\epsilon^2)(1+\eta\eta_i)/2 \qquad (\text{for } i = 5, 6), \tag{18}$$

$$N_i = (1-\eta^2)(1+\epsilon\epsilon_i)/2 \qquad (\text{for } i = 6, 8), \tag{19}$$

where η and ϵ are local natural coordinates of the element.

ψ	Aspect ratio (L/s)	Present FEM (8×8)	Present FEM (6×6)	[Liew et al. 1994]
0°	0.6	0.3524	0.3552	0.3599
	0.7	0.2991	0.3013	0.3060
	0.8	0.2715	0.2741	0.2783
30°	0.6	0.2805	0.2834	0.2882
	0.7	0.2507	0.2528	0.2575
	0.8	0.2364	0.2389	0.2417

Table 1. Convergence study for NDFF ($\omega=\omega_n b_0^2\sqrt{(\rho h/D)}$, where $D=Eh^3/12(1-\nu^2)$) of the pretwisted shallow conical shells, considering $\nu=0.3$, $s/h=1000$, $\theta_v=15°$, and $\theta_0=30°$.

4. Results and discussion

The nondimensional fundamental frequencies (NDFF) and nondimensional second natural frequencies (NDSF) for conical shells having a curvature ratio (b_0/R_y) of 0.5 and a thickness ratio (s/h) of 1000 are obtained corresponding to different nondimensional speeds of rotation, $\Omega=0.0$, 0.5, and 1.0 (where $\Omega=\Omega'/\omega_0$), with relative distance $d/L=0.5$; the parameters n_d, n, a, Ω', ω_0, ρ, and d represent the number of delaminations, number of layers, crack length, actual angular speed of rotation, fundamental natural frequency of a nonrotating shell, and density, respectively. The material properties of the graphite-epoxy composite [Qatu and Leissa 1991a] are considered as $E_1=138.0$ GPa, $E_2=8.96$ GPa, $\nu=0.3$, $G_{12}=7.1$ GPa, $G_{13}=7.1$ GPa, and $G_{23}=2.84$ GPa. Convergence studies are also performed to determine the converged mesh size (Table 1). It is observed from the convergence study that uniform mesh divisions of 6 × 6 and 8 × 8 considering the complete planform of the shell provide nearly equal results, the difference being around one percent; the results also corroborate monotonic downward convergence. The slight differences between the values of the present solution and those of [Liew et al. 1994] can be attributed to consideration of transverse shear deformation and rotary inertia in the present FEM and also to the fact that the Ritz method always overestimates the structural stiffness. Moreover, increasing the size of the matrix because of higher mesh size increases the ill-conditioning of the numerical eigenvalue problem [Qatu and Leissa 1991b]. Hence, the lower mesh size (6 × 6), consisting of 36 elements and 133 nodes, has been used for the analysis due to computational efficiency. The total number of degrees of freedom involved in the computation is 665 as each node of the isoparametric plate bending element has five degrees of freedom, three translational and two rotational.

4.1. ***Validation of results.*** Computer codes were developed based on the present finite element method. The numerical results obtained are compared and validated with the results of [Liew et al. 1994; Krawczuk et al. 1997; Karmakar et al. 2005] as furnished in Table 1, Figure 3, and Table 2, respectively. The comparative study shows excellent agreement with the previously published results and hence demonstrates the capability of the code developed and proves the accuracy of the analyses.

4.2. ***Effect of stacking sequence and twist angle.*** A parametric study is conducted to obtain the nondimensional natural frequencies of eight-layered graphite-epoxy bending-stiff composite shallow conical

	Two delaminations		Three delaminations	
Ω	Present FEM	[Karmakar et al. 2005]	Present FEM	[Karmakar et al. 2005]
0.0	1.9316	1.9332	1.9048	1.8994
0.5	2.1080	2.1921	2.0469	2.1495
1.0	2.6735	2.7475	2.5996	2.6874

Table 2. NDFF ($\omega = \omega_n L^2 \sqrt{(\rho/E_1 h^2)}$) of eight-layered graphite-epoxy composite [0°/0°/30°/−30°]s rotating cylindrical shells with 25% delaminations located at several positions (for 2 delaminations: 0°/0°/30°//−30°/−30°/30°/0°//0° and for 3 delaminations: 0°//0°/30°/−30°//−30°/30°//0°/0°, where // indicates the location of delamination) across the thickness, $a/b = 1$, $b/h = 100$, and $b_0/R_y = 0.5$.

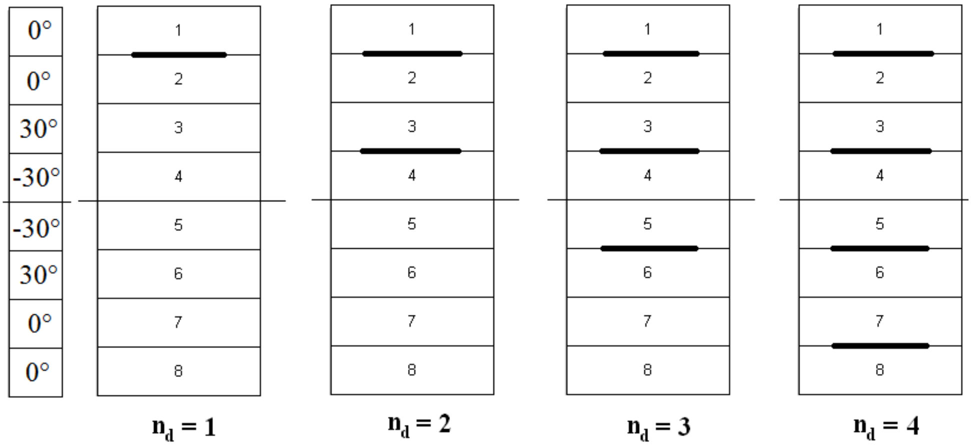

Figure 4. Arrangement of layers of eight-layered laminated composite with delamination.

shells under single, double, triple, and quadruple delaminations with different twist angles, as furnished in Table 3. The arrangement of layers with delamination is shown in Figure 4. At a stationary condition for a particular number of delaminations, nondimensional fundamental natural frequencies are identified to attain a maximum value for twist angle $\psi = 0°$ and gradually decrease to a minimum value for twist angle $\psi = 45°$. It is also noted that at a stationary condition for a particular angle of twist, the nondimensional fundamental frequencies are found to reduce with the increase of the number of delamination. This can be attributed to the fact that the delamination leads to reduction in the elastic stiffness. The centrifugal stiffening effect (that is, the increase of structural stiffness with increase of rotational speed) is predominantly found with reference to nondimensional fundamental and second natural frequencies of bending-stiff composites irrespective of twist angle. Under a rotating condition, the nondimensional fundamental frequencies of delaminated composite laminates found a drooping trend with an increase of twist angle.

4.3. ***Effect of relative frequency.*** The trends of the relative frequencies (the ratio of rotating natural frequency and stationary natural frequency) at $\Omega = 0.5$ and $\Omega = 1.0$ for a bending stiff configuration corresponding to NDFF are furnished in Figures 5a and 5b, respectively. The percentage difference

		NDFF			NDSF		
n_d	ψ	$\Omega = 0.0$	$\Omega = 0.5$	$\Omega = 1.0$	$\Omega = 0.0$	$\Omega = 0.5$	$\Omega = 1.0$
1	0°	0.3925	0.5231	0.6015	0.4953	0.6281	0.6279
	15°	0.2378	0.4552	0.5584	0.4946	0.5669	0.5644
	30°	0.1434	0.2617	0.4863	0.4935	0.5042	0.4983
	45°	0.0947	0.2056	0.3641	0.4932	0.5041	0.4550
2	0°	0.3190	0.5130	0.5529	0.5337	0.7227	0.6175
	15°	0.2092	0.3884	0.4353	0.4677	0.6555	0.6982
	30°	0.1295	0.1457	0.1401	0.4197	0.5249	0.5731
	45°	0.0882	0.1505	0.2388	0.4196	0.4867	0.5289
3	0°	0.2449	0.4967	0.4430	0.3825	0.5551	0.8587
	15°	0.1831	0.3316	0.4004	0.3339	0.3729	0.4402
	30°	0.1174	0.0664	0.4125	0.3017	0.2992	0.6361
	45°	0.0828	0.1134	0.2469	0.2965	0.5030	0.4840
4	0°	0.2565	0.4880	0.4075	0.2727	0.4670	0.6622
	15°	0.1841	0.3235	0.3667	0.2343	0.4136	0.5655
	30°	0.1162	0.2815	0.2168	0.2087	0.3711	0.6706
	45°	0.0816	0.0983	0.4494	0.2010	0.3549	0.7109

Table 3. NDFF and NDSF ($\omega = \omega_n L^2\sqrt{(\rho/E_1 h^2)}$) of delaminated bending-stiff composite conical shells for various twist angles, considering $n = 8$, $h = 0.0004$, $s/h = 1000$, $a/L = 0.33$, $d/L = 0.5$, $L/s = 0.7$, $\theta_0 = 45°$, and $\theta_v = 20°$.

between the maximum and minimum relative frequencies with respect to NDFF at lower rotational speeds are found as 38.6%, 39.4%, 72.1%, and 50.3% corresponding to $n_d = 1$, 2, 3, and 4, respectively. On the other hand, the same at higher rotational speeds are found as 60.1%, 60.0%, 48.5% and 71.2% corresponding to $n_d = 1$, 2, 3, and 4, respectively. Hence this also proves the fact that for higher rotational speeds, the relative frequencies have a pronounced effect. Considering the twist of the laminate at lower rotational speeds, the percentage difference between the maximum and minimum relative frequencies with respect to NDFF are found as 34.3%, 8.2%, 76.7%, and 44.5% corresponding to $\psi = 0°$, 15°, 30°, and 45°, respectively. On the other hand, the same at higher rotational speeds are found as 15.3%, 15.2%, 69.2%, and 50.8% corresponding to $\psi = 0°$, 15°, 30°, and 45°, respectively. Hence it is observed that under a rotating condition, the relative frequencies (NDFF) have a pronounced effect corresponding to twist angle $\psi = 30°$.

In contrast, at lower rotational speeds, the percentage difference between the maximum and minimum relative frequencies with respect to NDSF are found as 19.4%, 17.2%, 41.5%, and 3.7% corresponding to $n_d = 1$, 2, 3, and 4, respectively, while the same at higher rotational speeds are found as 15.3%, 15.2%, 69.2%, and 50.8% corresponding to $n_d = 1$, 2, 3, and 4, respectively. On the other hand, the percentage difference between the maximum and minimum relative frequencies with respect to NDSF are found as 25.9%, 36.7%, 44.2%, and 42.1% corresponding to $\psi = 0°$, 15°, 30°, and 45°, respectively, while the same at higher rotational speeds are obtained as 52.4%, 52.7%, 68.6%, and 73.9% corresponding

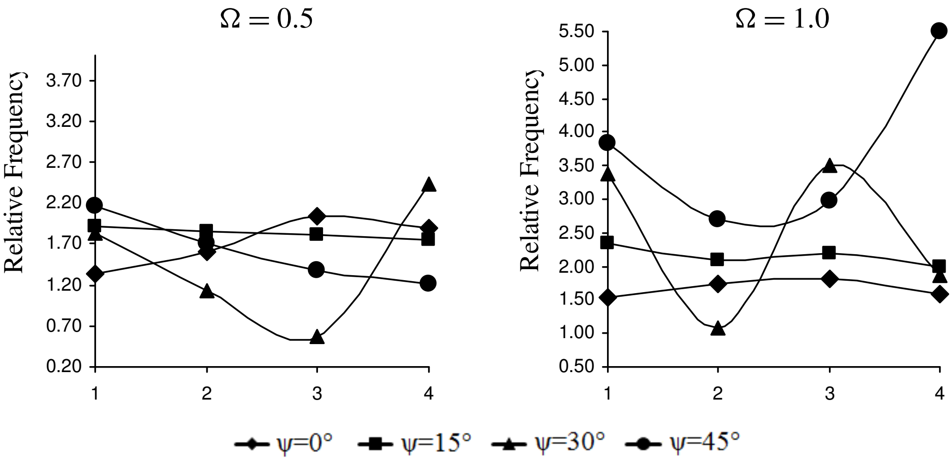

Figure 5. Variation of relative frequencies (NDFF) of graphite-epoxy bending stiff composite conical shells with delamination at rotation speeds $\Omega = 0.5$ (left) and $\Omega = 1.0$ (right) for different twist angles Ψ and different numbers of delaminations. Other parameters are $n = 8$, $h = 0.0004$, $a/L = 0.33$, $d/L = 0.5$, $s/h = 1000$, $L/s = 0.7$, $\theta_0 = 45°$, and $\theta_v = 20°$.

to $\psi = 0°$, 15°, 30°, and 45°, respectively. Hence it could be inferred that the relative frequencies corresponding to NDSF have a greater effect only for higher rotational speeds.

5. Mode shapes

The mode shapes corresponding to NDFF and NDSF are shown in Figures 6 and 7, respectively, for various twist angles at the stationary condition ($\Omega = 0.0$) and a number of delaminations, for eight-layered graphite-epoxy symmetric bending-stiff composite shallow conical shells. The fundamental mode corresponds to the first torsion. The symmetry modes are absent when the twist angle is nonzero and the nodal lines indicate zero displacement amplitude. The first spanwise bending is observed for an untwisted conical shell at the stationary condition corresponding to the second natural frequencies for single, double, and triple delamination cases ($n_d = 1, 2, 3$), but the dominance of the first torsional mode is identified for the twisted cases corresponding to the second natural frequency.

6. Conclusions

The following conclusions are drawn from the present study:

(1) The finite element formulation presented in this paper can be successfully applied to analyze the natural frequencies of multiple delaminated conical shells for any particular laminate configuration.

(2) In general, at a stationary condition, the nondimensional fundamental frequency parameter decreases with increase in the twist angle. Under a rotating condition, nondimensional fundamental frequencies of the delaminated composite laminates with bending-stiff configuration are found to decrease with an increase of the twist angle.

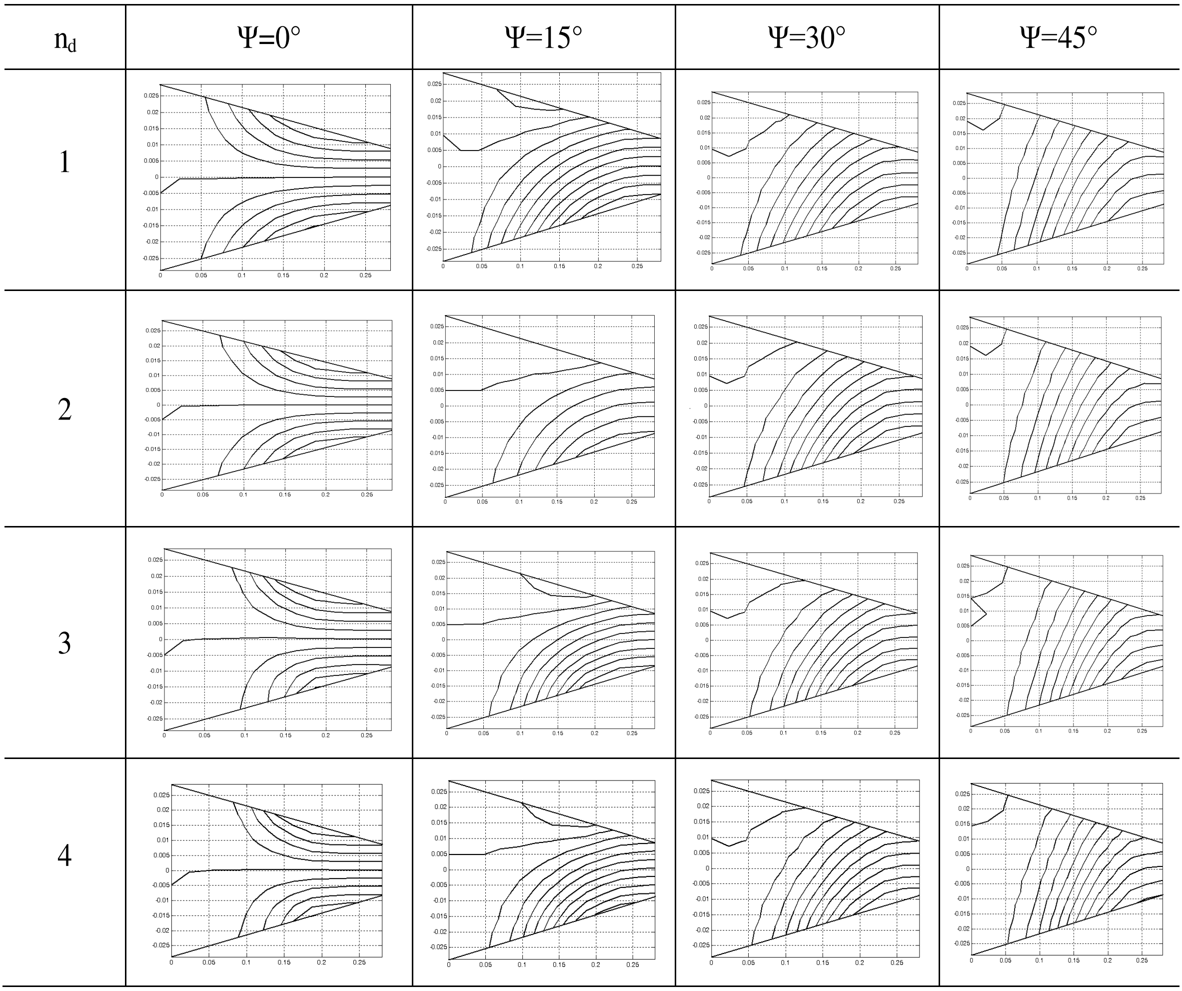

Figure 6. Effect of twist and number of delaminations on mode shapes for NDFF of graphite-epoxy bending-stiff delaminated composite conical shells, considering $n = 8$, $h = 0.0004$, $s/h = 1000$, $a/L = 0.33$, $d/L = 0.5$, $L/s = 0.7$, $\theta_0 = 45°$, and $\theta_v = 20°$.

(3) An increase in the number of delaminations leads to a reduction in elastic stiffness irrespective of the twist angles.

(4) The relative frequencies corresponding to the nondimensional second natural frequencies have a pronounced effect for higher rotational speeds.

(5) The fundamental mode corresponds to the first torsion. The first spanwise bending is observed for an untwisted conical shell at a stationary condition corresponding to the second natural frequencies for single, double, and triple delamination cases.

(6) The nondimensional frequencies obtained are the first known results which can serve as reference solutions for future investigations.

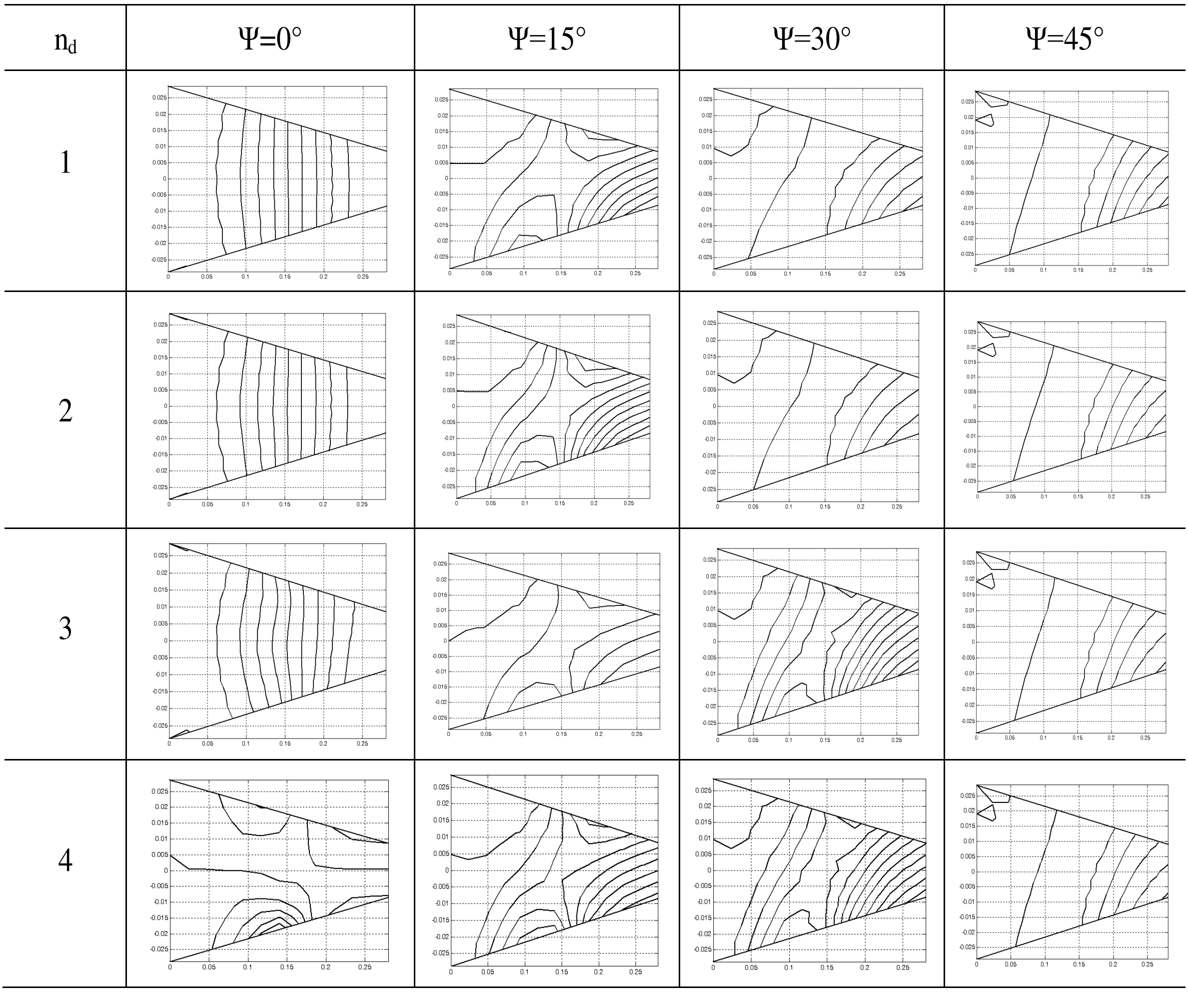

Figure 7. Effect of twist and number of delaminations on mode shapes for NDSF of graphite-epoxy bending-stiff delaminated composite conical shells, considering $n = 8$, $h = 0.0004$, $s/h = 1000$, $a/L = 0.33$, $d/L = 0.5$, $L/s = 0.7$, $\theta_0 = 45°$, and $\theta_v = 20°$.

References

[Aydogdu and Timarci 2003] M. Aydogdu and T. Timarci, "Vibration analysis of cross-ply laminated square plates with general boundary conditions", *Compos. Sci. Technol.* **63**:(7) (2003), 1061–1070.

[Aymerich et al. 2009] F. Aymerich, F. Dore, and P. Priolo, "Simulation of multiple delamination in impacted cross-ply laminates using a finite element model based on cohesive interface elements", *Compos. Sci. Technol.* **69**:(11–12) (2009), 1699–1709.

[Bathe 1990] K. J. Bathe, *Finite element procedures in engineering analysis*, Prentice Hall of India, New Delhi, 1990.

[Crawley 1979] E. F. Crawley, "The natural modes of graphite/epoxy cantilever plates and shells", *Compos. Mater.* **13** (1979), 195–205.

[Gim 1994] C. K. Gim, "Plate finite element modeling of laminated plates", *Comput. Struct.* **52**:(1) (1994), 157–168.

[Karmakar and Sinha 2001] A. Karmakar and P. K. Sinha, "Failure analysis of laminated composite pretwisted rotating plates", *J. Reinf. Plast. Compos.* **20**:(15) (2001), 1326–1357.

[Karmakar et al. 2005] A. Karmakar, T. K. Mishra, and K. Kishimoto, "Free vibration characteristics of delaminated composite rotating cantilever shallow shells", in *Proceeding of the International Conference on Fracture*, Turin, Italy, March 20–25 2005.

[Krawczuk et al. 1997] M. Krawczuk, W. Ostachowicz, and A. Zak, "Dynamics of cracked composite material structures", *Comput. Mech.* **20** (1997), 79–83.

[Lee et al. 2002] J. J. Lee, C. H. Yeom, and I. Lee, "Vibration analysis of twisted cantilever conical composite shells", *J. Sound Vib.* **255**:(5) (2002), 965–982.

[Leissa et al. 1984] A. W. Leissa, J. K. Lee, and A. J. Wang, "Vibrations of twisted rotating blades", *J. Vib. Acoust.* (*ASME*) **106** (1984), 251–257.

[Liew et al. 1994] K. M. Liew, C. M. Lim, and L. S. Ong, "Vibration of pretwisted cantilever shallow conical shells", *Int. J. Solids Struct.* **31** (1994), 2463–74.

[McGee and Chu 1994] O. G. McGee and H. R. Chu, "Three-dimensional vibration analysis of rotating laminated composite blades", *J. Eng. Gas Turb. Power* (*ASME*) **116** (1994), 663–671.

[Parhi et al. 2001] P. K. Parhi, S. K. Bhattacharyya, and P. K. Sinha, "Failure analysis of multiple delaminated due to bending and impact", *Bull. Mater. Sci.* **24**:(2) (2001), 143–149.

[Qatu and Leissa 1991a] M. S. Qatu and A. W. Leissa, "Natural frequencies for cantilevered doubly-curved laminated composite shallow shells", *Compos. Struct.* **17** (1991), 227–255.

[Qatu and Leissa 1991b] M. S. Qatu and A. W. Leissa, "Vibration studies for laminated composite twisted cantilever plates", *Int. J. Mech. Sci.* **33** (1991), 927–940.

[Rebière and Gamby 2004] J. L. Rebière and D. Gamby, "A criterion for modeling initiation and propagation of matrix cracking and delamination in cross-ply laminates", *Compos. Sci. Technol.* **64**:(13–14) (2004), 2239–2250.

[Shen and Grady 1992] M. H. H. Shen and J. E. Grady, "Free vibrations of delaminated beams", *AIAA J.* **30** (1992), 1361–1370.

[Tripathi et al. 2007] V. Tripathi, B. N. Singh, and K. K. Shukla, "Free vibration of laminated composite conical shells with random material properties", *Compos. Struct.* **81** (2007), 96–104.

Received 26 Oct 2011. Revised 2 Jan 2012. Accepted 3 Jan 2012.

SUDIP DEY: `infosudip@gmail.com`
Mechanical Engineering Department, Jadavpur University, Kolkata 700032, India

AMIT KARMAKAR: `shrikatha@yahoo.co.in`
Mechanical Engineering Department, Jadavpur University, Kolkata 700032, India

SUBMISSION GUIDELINES

ORIGINALITY

Authors may submit manuscripts in PDF format online at the Submissions page. Submission of a manuscript acknowledges that the manuscript is original and has neither previously, nor simultaneously, in whole or in part, been submitted elsewhere. Information regarding the preparation of manuscripts is provided below. Correspondence by email is requested for convenience and speed. For further information, write to one of the Chief Editors:

Davide Bigoni	bigoni@ing.unitn.it
Iwona Jasiuk	ijasiuk@me.concordia.ca
Yasuhide Shindo	shindo@material.tohoku.ac.jp

LANGUAGE

Manuscripts must be in English. A brief abstract of about 150 words or less must be included. The abstract should be self-contained and not make any reference to the bibliography. Also required are keywords and subject classification for the article, and, for each author, postal address, affiliation (if appropriate), and email address if available. A home-page URL is optional.

FORMAT

Authors can use their preferred manuscript-preparation software, including for example Microsoft Word or any variant of TeX. The journal itself is produced in LaTeX, so accepted articles prepared using other software will be converted to LaTeX at production time. Authors wishing to prepare their document in LaTeX can follow the example file at www.jomms.net (but the use of other class files is acceptable). At submission time only a PDF file is required. After acceptance, authors must submit all source material (see especially Figures below).

REFERENCES

Bibliographical references should be complete, including article titles and page ranges. All references in the bibliography should be cited in the text. The use of BibTeX is preferred but not required. Tags will be converted to the house format (see a current issue for examples); however, for submission you may use the format of your choice. Links will be provided to all literature with known web locations; authors can supply their own links in addition to those provided by the editorial process.

FIGURES

Figures must be of publication quality. After acceptance, you will need to submit the original source files in vector format for all diagrams and graphs in your manuscript: vector EPS or vector PDF files are the most useful. (EPS stands for Encapsulated PostScript.)

Most drawing and graphing packages—Mathematica, Adobe Illustrator, Corel Draw, MATLAB, etc.—allow the user to save files in one of these formats. Make sure that what you're saving is vector graphics and not a bitmap. If you need help, please write to graphics@msp.org with as many details as you can about how your graphics were generated.

Please also include the original data for any plots. This is particularly important if you are unable to save Excel-generated plots in vector format. Saving them as bitmaps is not useful; please send the Excel (.xls) spreadsheets instead. Bundle your figure files into a single archive (using zip, tar, rar or other format of your choice) and upload on the link you been given at acceptance time.

Each figure should be captioned and numbered so that it can float. Small figures occupying no more than three lines of vertical space can be kept in the text ("the curve looks like this:"). It is acceptable to submit a manuscript with all figures at the end, if their placement is specified in the text by means of comments such as "Place Figure 1 here". The same considerations apply to tables.

WHITE SPACE

Forced line breaks or page breaks should not be inserted in the document. There is no point in your trying to optimize line and page breaks in the original manuscript. The manuscript will be reformatted to use the journal's preferred fonts and layout.

PROOFS

Page proofs will be made available to authors (or to the designated corresponding author) at a Web site in PDF format. Failure to acknowledge the receipt of proofs or to return corrections within the requested deadline may cause publication to be postponed.

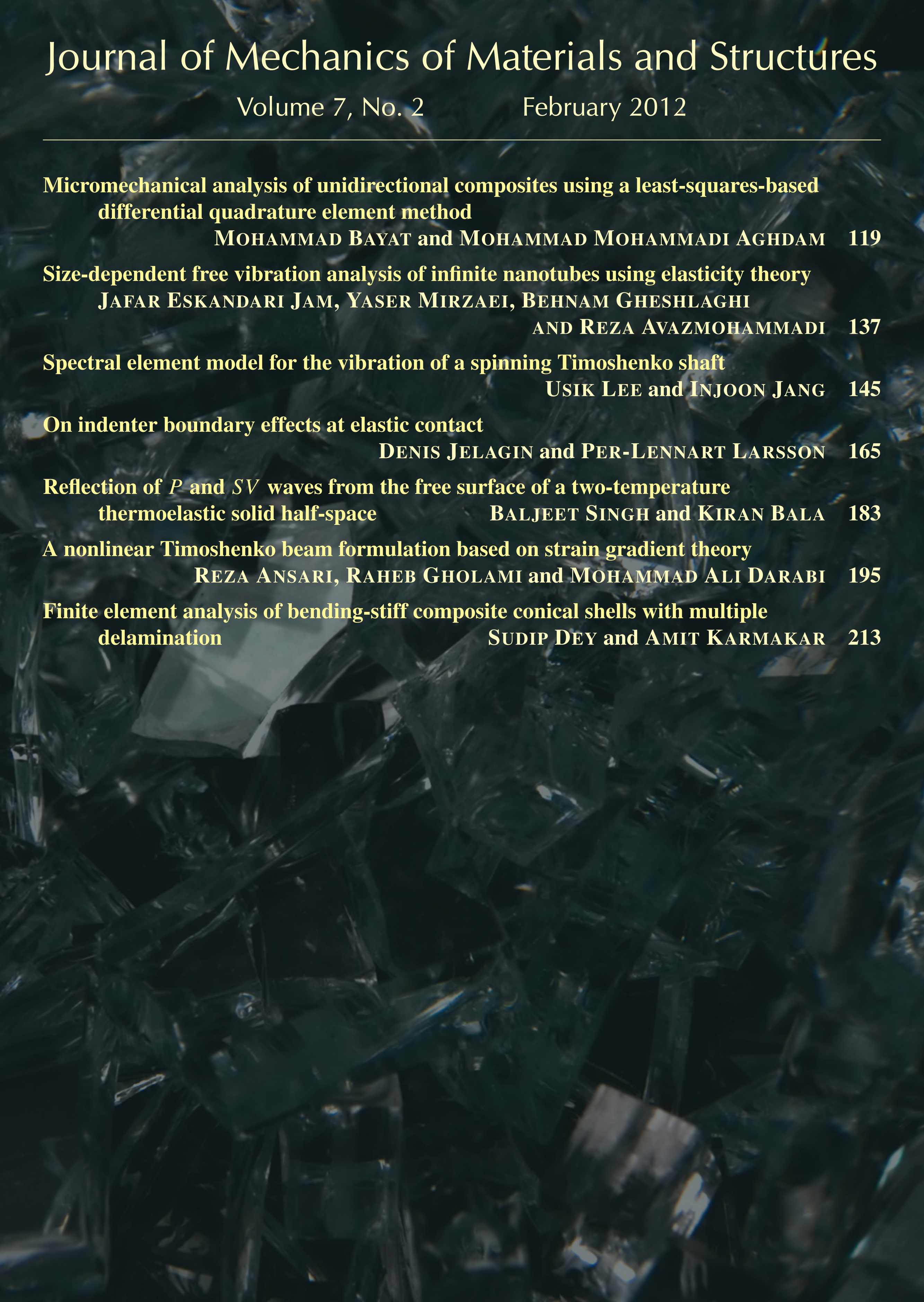

Journal of Mechanics of Materials and Structures

Volume 7, No. 2 February 2012